

**TOPICAL REVIEW**

# Electronic and optoelectronic nano-devices based on carbon nanotubes

**M Scarselli, P Castrucci and M De Crescenzi**

Dipartimento di Fisica, Università di Roma Tor Vergata, Roma, Italy

E-mail: [manuela.scarselli@roma2.infn.it](mailto:manuela.scarselli@roma2.infn.it)

Received 2 April 2012

Published 11 July 2012

Online at [stacks.iop.org/JPhysCM/24/313202](http://stacks.iop.org/JPhysCM/24/313202)**Abstract**

The discovery and understanding of nanoscale phenomena and the assembly of nanostructures into different devices are among the most promising fields of material science research. In this scenario, carbon nanostructures have a special role since, in having only one chemical element, they allow physical properties to be calculated with high precision for comparison with experiment. Carbon nanostructures, and carbon nanotubes (CNTs) in particular, have such remarkable electronic and structural properties that they are used as active building blocks for a large variety of nanoscale devices. We review here the latest advances in research involving carbon nanotubes as active components in electronic and optoelectronic nano-devices. Opportunities for future research are also identified.

(Some figures may appear in colour only in the online journal)

**Contents**

1. Introduction	1
2. The structure of carbon nanotubes	3
3. Electronic properties	3
4. Methods of synthesis	6
4.1. Chemical vapour deposition	7
4.2. Structural defects in carbon nanotubes	8
5. Characterization techniques	8
6. Transport properties of carbon nanotubes	11
7. Solar cells	20
7.1. Carbon nanotube solar cells	21
7.2. Photoelectrochemical devices	27
7.3. Polymer solar cells	31
8. Conclusions and future prospects	33
References	33

## 1. Introduction

Nanostructures are low-dimensional systems with length scales down to a few nanometres. The majority of their

properties are altered with respect to bulk materials; this is because the smaller the systems, the more likely it is that size-related quantum confinement effects will regulate their electrical, optical and magnetic properties. Therefore, at this early stage of nanoscience development, model systems are necessary for providing general concepts that might be applicable for the description of nanoscale phenomena and for more complex small scale structures. The great challenge of the next decades will be the application of nanoscience concepts to the development of new materials and technologies that can address the major requirements of the next generation; these include the increasing need for clean energy and improvements in living conditions and quality of life.

In this research field, carbon plays a significant role since it can be found in different stable aggregation forms because of its flexible electronic configuration. Each identified structure has a peculiar geometrical configuration and related properties that make it a unique building block for future nanomaterials. The carbon atom has six electrons; the 2s orbital and two or three of the 2p orbitals can form an  $sp^2$  or  $sp^3$  hybrid, respectively. Until the 1980s the only known carbon ordered structures were graphite and diamond.

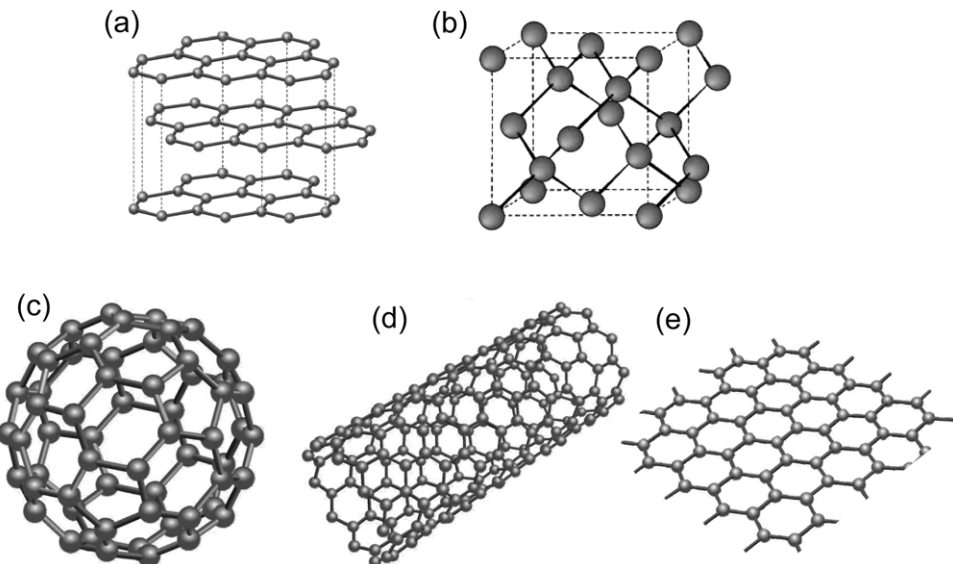


**Figure 1.** Carbon ordered structures including (a) graphite, consisting of a stack of graphene layers, (b) diamond, and the new carbon allotropes (c) 0D, buckminsterfullerene ( $C_{60}$ ), consisting of graphene balled into a sphere, (d) 1D, nanotube, made of a rolled-up cylinder of graphene, and (e) 2D, graphene.

The  $sp^2$  orbital hybridization leads to the strong in-plane bonds of the hexagonal structure of graphite (figure 1(a)), leaving the p-like orbital involved in the weak bonds between the planes. Meanwhile, the  $sp^3$  configuration gives rise to the tetrahedral bonded structure of diamond, figure 1(b). In 1985, the discovery of the buckyball [1], which consists of a single layer of graphite balled into a sphere by introducing pentagons and hexagons into the lattice, the most famous being  $C_{60}$  (figure 1(c)), marked the beginning of a new era for carbon allotropes. These allotropes can now be divided into three broad categories, namely zero-dimensional (0D) systems such as fullerenes, one-dimensional (1D) systems such as nanotubes [2–5], figure 1(d), and two-dimensional (2D) systems commonly referred to as graphene (i.e. a single sheet or plane of graphite) [6–8], figure 1(e).

The one-dimensional carbon form was first observed in 1976 [2] as hollow structures named ‘carbon nanotubes’ (CNTs) and aroused great interest only after the pioneering work of Iijima in the early 1990s [3–5]. Carbon nanotubes consist of one or more graphite sheets rolled up to form a cylinder infinitely extended along the axis, whereas along the circumference there are only very few atoms. The diameter can be as little as 1 nm and the length up to several centimetres. Although CNTs are made up only of carbon atoms, their physical properties can vary substantially depending on variations in their microscopic structure. One of the most intriguing properties is their ability to show semiconducting or metallic behaviour depending on their diameter and on the orientation of the carbon hexagons with respect to the nanotube axis [9–11]. This distinct electronic property is displayed without changing the local bonding and sets nanotubes apart from all other nanostructured materials. In addition, their one-dimensional character and the presence of van Hove singularities were first derived from tight-binding calculations [10, 11] and shortly after

validated experimentally [12–14]. The van Hove singularities are responsible for the unique optical properties observed in single-walled CNTs (SWCNTs) and more recently also in multiwalled CNTs (MWCNTs), as will be detailed in this paper.

While CNTs are supposed to constitute the building blocks for future nanoscale devices their fundamental properties have to be studied systematically. This was made possible only after effective control of the growth process and when large scale quantities of material had been obtained [15]. As well as their electronic properties, CNTs also possess an array of unprecedented structural and mechanical properties such as extremely high tensile strength and elasticity [16–18], together with a good chemical and thermal stability. In recent decades CNTs have provided the scientific community with an excellent opportunity to find a fruitful match between experiment, theory, and simulation, as can be easily verified by the extensive published literature.

Our review begins with an introduction to the atomic structure (section 2) and electronic properties (section 3) of CNTs, establishing the basic concepts that will be useful in later sections. Section 4 summarizes and compares the main synthesis techniques that have allowed CNT production on a large scale. The most important experimental techniques used for the CNTs’ morphological, structural and electronic characterization are described in section 5. The electronic transport properties are the focus of section 6, where the concepts of quantum conductance and transport properties are introduced as well as a discussion of the role of phonon and defect scattering. Some examples of CNT transistors are illustrated, and the simplest such device, the p–n junction, is also discussed. Section 7 addresses the emerging area of solar cell devices. Section 7.1 focuses on the optoelectronic applications of CNTs, first reviewing the aspects of photoconductivity and then focusing on the

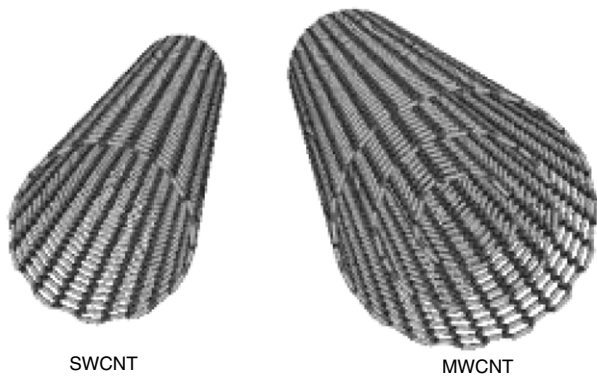


**Figure 2.** SWCNT and MWCNT.

most relevant CNT solar cell devices. Two more sections are dedicated to photoelectrochemical devices (section 7.2) and polymer–CNT solar cells (section 7.3). The future prospects will be discussed in section 8.

## 2. The structure of carbon nanotubes

A single sheet of  $sp^2$  hybridized carbon makes a bonded graphite, and when rolled up into a hollow cylinder with no surface broken bonds is called a single-walled carbon nanotube (SWCNT), figure 2. A tube comprising several, concentrically arranged cylinders as in a ‘Russian doll’ configuration is referred to as a multiwalled carbon nanotube (MWCNT), as shown in figure 2. The name multiwalled nanotube is restricted to nanostructures with outer diameters of about 30 nm, above which the structures are called carbon nanofibres and possess properties somewhere between carbon fibres and MWCNTs [19].

SWCNTs have diameters of 1–2 nm, while MWCNTs have diameters of 10–30 nm with an interlayer spacing of 0.34 nm. The lengths of the two types of tube can reach hundreds of microns or even centimetres. There are many

possible carbon nanotubes depending on how the graphite layer is rolled into a cylinder. Because the microscopic structure of CNTs is closely related to that of a single layer of graphite, the tubes are usually labelled in terms of the two main lattice vectors, as illustrated in figure 3 referring to SWCNT geometry. In particular, a CNT is defined by the circumferential vector of the tube, called the chiral vector ( $\mathbf{C}$ ), that uniquely defines the circumference of the chosen tube [19]. In this way, a SWCNT’s geometry is completely specified by the definition of the relative position  $\mathbf{C} = n\mathbf{a}_1 + m\mathbf{a}_2 \equiv (n, m)$  of the pair of atoms in a graphene strip which, when rolled onto each other, form a tube, while  $\mathbf{a}_1$  and  $\mathbf{a}_2$  are unit vectors of the hexagonal honeycomb lattice.

The diameter  $d$  of the nanotube can thus be estimated from

$$d = |\mathbf{C}|/\pi = \frac{a}{\pi} \sqrt{n^2 + nm + m^2}$$

where  $a$  is the lattice constant of the honeycomb network:  $a = \sqrt{3}a_{C-C}$ , and  $a_{C-C} = 1.42 \text{ \AA}$  is the C–C bond length. The chiral vector  $\mathbf{C}$  uniquely defines a particular tube, as well as its chiral angle  $\theta$ , which is the angle between  $\mathbf{C}$  and  $\mathbf{a}_1$ .

There are three distinct geometries of SWCNTs: armchair, zig-zag and chiral, as shown in figure 4.

1. Nanotubes of type  $(n, n)$  are commonly called armchair nanotubes because of the  $\backslash/\backslash/\backslash$  shape, perpendicular to the tube axis, see the red line in figure 3.
2. Nanotubes of type  $(n, 0)$  are known as zig-zag nanotubes because of the  $\backslash\backslash\backslash$  shape, perpendicular to the tube axis, see the blue line in figure 3.
3. All the remaining nanotubes are known as chiral nanotubes.

## 3. Electronic properties

The most intriguing property of SWCNTs is their ability to show semiconducting or metallic properties according to

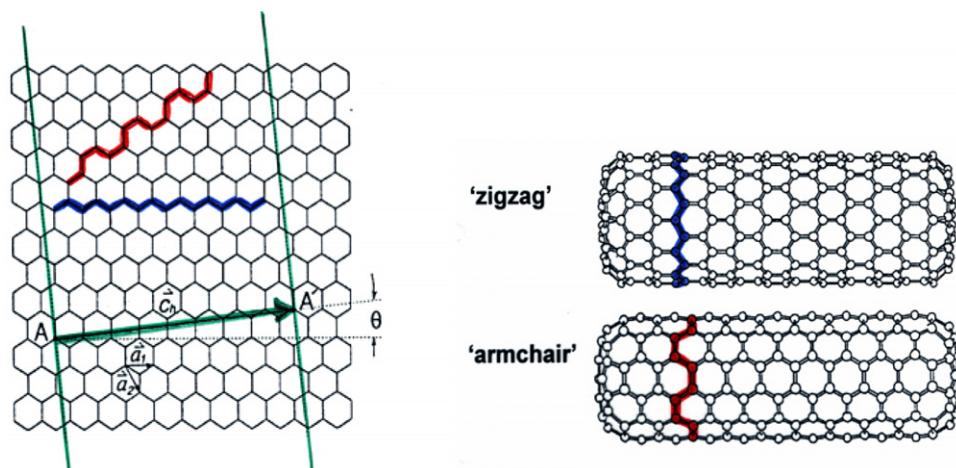


**Figure 3.** Graphene honeycomb network with lattice vectors  $\mathbf{a}_1$  and  $\mathbf{a}_2$ . The chiral vector  $\mathbf{C} = n\mathbf{a}_1 + m\mathbf{a}_2$  represents a possible wrapping of the two-dimensional graphene sheet into a tubular form. The direction perpendicular to  $\mathbf{C}$  is the tube axis. The chiral angle  $\theta$  is defined by the  $\mathbf{C}$  vector and the  $\mathbf{a}_1$ .

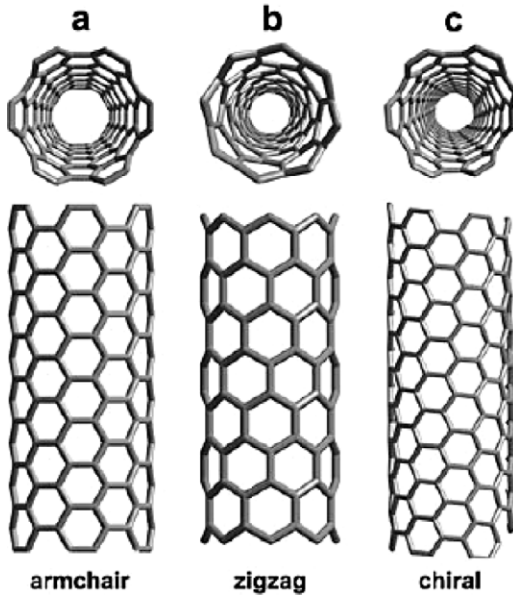


**Figure 4.** Models of SWCNTs exhibiting different chiralities: (a) armchair, (b) zig-zag, and (c) chiral arrangement.

a general rule that can be summarized as follows.  $(n, n)$  armchair tubes are always metallic, since their intrinsic symmetry and curvature do not change this property, figure 4(a). All  $n - m = 3p$ , with  $p$  a nonzero integer, are metallic.  $(n, 0)$  zig-zag tubes are metallic when  $n$  is an integer multiple of 3, as reported in figure 5(b) for a  $(9, 0)$  tube; otherwise when  $n$  is not a multiple of 3 a small energy gap opens and the tube is semiconducting. Finally all  $n - m = 3p \pm 1$  tubes are semiconductors (figure 4). Consequently, most CNTs are semiconductors ( $2/3$ ), and only a fraction of them ( $1/3$ ) are metallic (or semi-metallic). The associated number of available states for a given energy interval, that is the density of states (DOS) of the CNTs, can be evaluated theoretically [20, 21] and experimentally validated under some approximations [12–14, 22–25]. It is well known that the shape of the density of states depends significantly on the system dimensionality. In 1D CNTs, the confinement properties in directions perpendicular to the tube axis come into view in the DOS as divergences near the band edges. These anomalies called van Hove singularities can be analytically derived from the dispersion relations as the inverse of the square root of the energy ( $1/\sqrt{E}$ ). As an example, figure 5 reports the calculated DOSs of armchair and zig-zag nanotubes respectively [21]. The panels show the dependence of the DOS on the chirality; in particular the DOS at the Fermi energy ( $E = 0$ ) is finite for metallic tubes while it is null for semiconducting ones. The calculated value of the energy gap depends on the tube diameter [26].

It can be noticed from figure 5 that van Hove singularities appear in the DOS for both metallic and semiconducting tubes at low as well as at high energies; these were found to determine many optical and transport properties of CNTs, as will be discussed later.

Atomic resolution low-temperature scanning tunnelling microscopy (STM) and scanning tunnelling spectroscopy

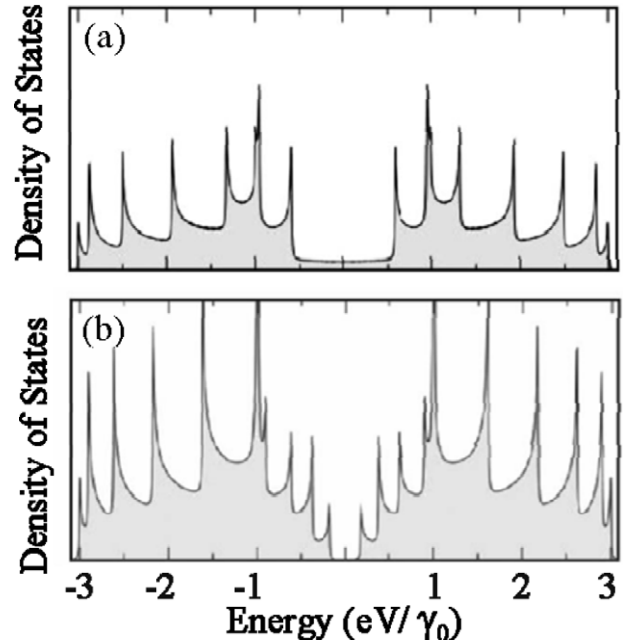


**Figure 5.** Electronic density of states (DOS) evaluated from the 1D energy dispersion relations within the zone-folding picture, based on the tight-binding approach. (a) armchair  $(5, 5)$ , (b)  $(9, 0)$  zig-zag tube. The DOSs are presented in the  $[-3\gamma_0, 3\gamma_0]$  energy range, with  $\gamma_0 = 2.9$  eV, the nearest neighbour C–C tight-binding overlap energy. The Fermi level is located at zero energy (adapted with permission from [21]). Copyright 2007 American Physical Society.

(STS) studies directly probe the relationship between the structural and electronic properties of carbon nanotubes [12–14, 22–25, 28]. Since STM can give direct information on the tube structure at atomic resolution, the tube chirality is easily detected from the images. STS measurements are performed keeping the tip position locked on a single isolated tube while registering the current flowing between the tip and the nanotube as a function of the applied bias ( $I-V$ ). The acquired  $I-V$  data allow direct evaluation of the conductance and the local electronic density of states of the nanotube. Figure 6 reports the results for metallic and semiconducting nanotubes.

STM experiments performed on an SWCNT shortened by applying voltage pulses to the tip allow the direct visualization of local electron standing waves along the tube axis [24, 25]. The electronic oscillation found has a period of approximately  $2L/n$ , where  $L$  is the tube length and  $n$  is an integer. This finding indicates that a quantum confinement of electrons in a 1D wire takes place [27]. Similar measurements performed on both metallic and semiconducting SWCNTs with lengths down to 3 nm have shown finite size effects [28]. These studies show that it is possible to reach and directly study low-dimensional systems where finite length produces quantization along the tube axis.

Later on a number of optical techniques, such as absorption [29–31], Raman spectroscopy [32–34], photoluminescence [35], and spectrofluorimetry [36], confirmed the relation between SWCNT geometry and electronic properties.

In the case of MWCNTs, theoretical studies are significantly more challenging because the numerous graphitic

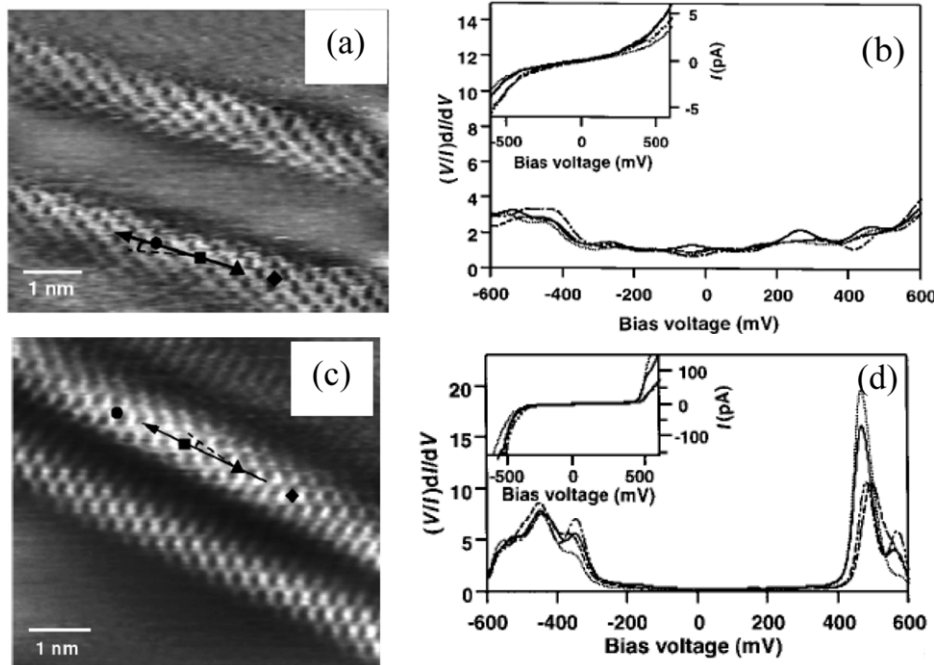


**Figure 6.** Atomically resolved STM images of individual SWCNTs on a Au(111) surface. Structure and spectroscopy of metallic SWCNTs: (a) constant current image, (b) calculated normalized conductance and measured  $I$ - $V$  (inset) data from the positions indicated by the symbols in (a) ( $V_{\text{bias}} = 0.15$  V,  $I_{\text{tunnel}} = 150$  pA). Structure and spectroscopy of semiconducting SWCNTs: (c) constant current image, (d) calculated normalized conductance,  $(V/I)dI/dV$ , and measured  $I$ - $V$  (inset) from the locations indicated by the symbols in (c) ( $V_{\text{bias}} = 0.3$  V,  $I_{\text{tunnel}} = 150$  pA). The tube axes in both images are indicated by solid, black arrows. It is possible to identify the tube chirality by measuring the angle between the tube axis and the hexagon rows (adapted with permission from [12]). Copyright 1998 Nature Publishing Group.

sheets rolled up in the tube require a large number of atoms to model the entire system. In addition, the intertube interactions play an important role in determining the structure of the energy bands, energy dispersion and density of states. Theoretical simulations can be found on double-walled carbon nanotubes (DWCNTs) [37–40], that represent the most simple model system of MWCNTs. Studies on DWCNT electronic properties predict that the intertube interactions induce changes in the energy bands also appreciable with absorption measurements [41]. The van Hove singularities found in the DW tubes have been exploited for the realization of solar cell prototypes [42]. In general, MWCNTs are closely related to graphite layers and are considered to exhibit similar electronic properties. Shyu *et al* [43] performed a detailed theoretical calculation based on electron energy loss spectroscopy (EELS) experiments, demonstrating that MWCNT electronic properties differ remarkably from those found in graphite. This finding has been confirmed by Castrucci *et al* [44] by direct EELS measurements showing the typical peak located around 6 eV of graphite with additional well-defined features between 2.8 and 3.2 eV, as shown in figure 7.

These findings suggest that MWCNTs have singularities in the density of states due to the reduced dimensionality and that they differ substantially from graphite. In fact, when the number of walls is low, the MWCNT density of states can be well reproduced by a superposition of the single wall carbon nanotube DOSs constituting the MWCNT structure, each maintaining its one-dimensional features in the electronic and

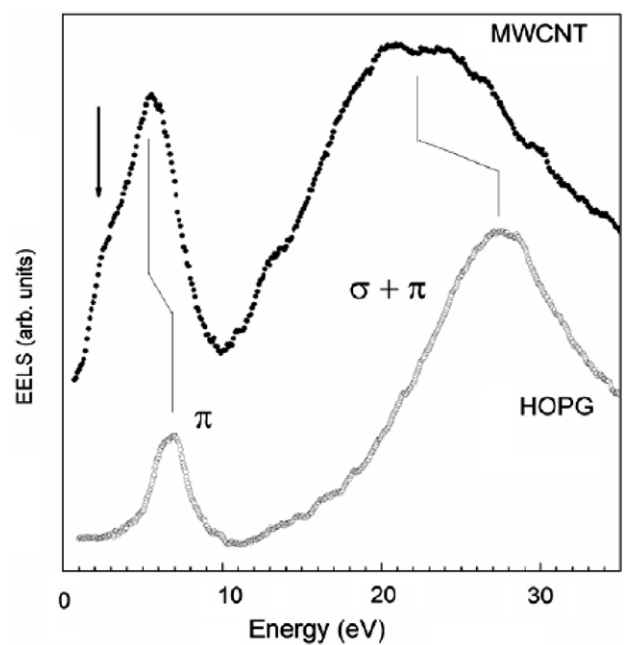


**Figure 7.** Transmission electron energy loss spectra measured by collecting inelastic electrons from a highly oriented pyrolytic graphite (HOPG) very thin flake and an MWCNT. Note the shoulder in the MWCNT spectra at energies lower than the plasmon  $\pi$  peak typical of graphitic systems [44].

transport properties. Figure 8 reports the calculated density of states for an arbitrary set of single, double and four wall (4WCNT) carbon nanotubes. First, by comparing the DOS

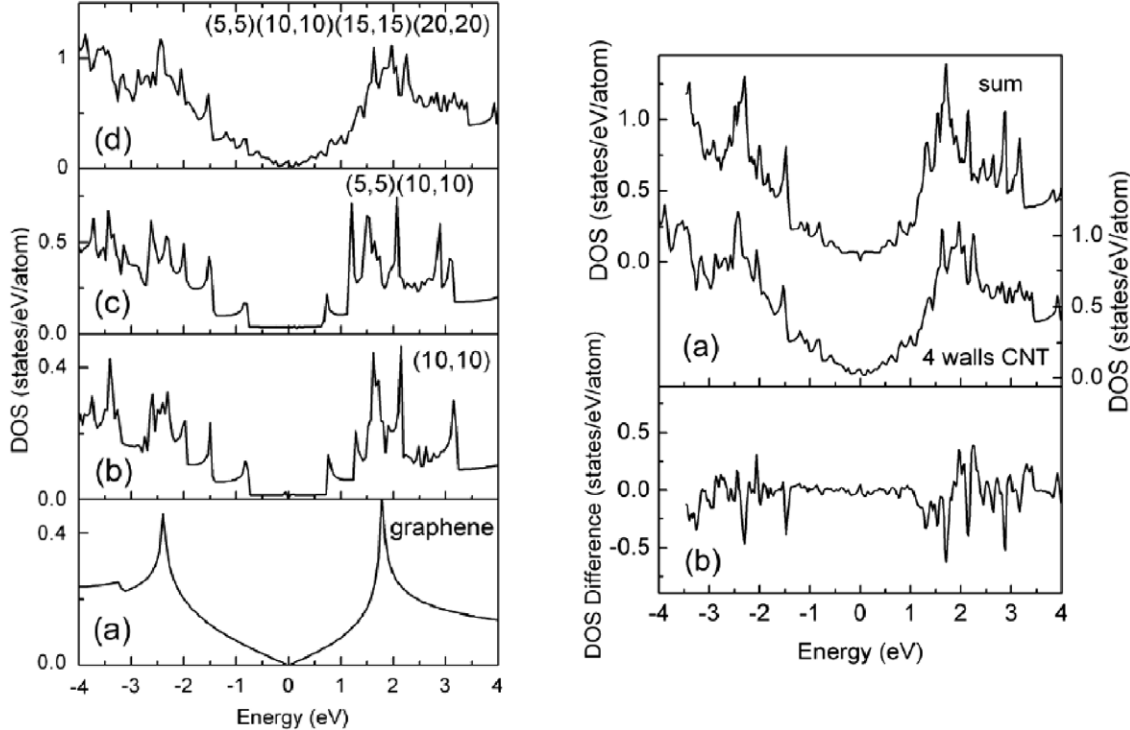


**Figure 8.** Left: comparison between the electronic DOSs calculated for (a) graphene, (b) a metallic SWCNT (10, 10), (c) a DWCNT made of two metallic SWCNTs (5, 5) (10, 10), and (d) a 4WCNT made of four metallic SWCNTs (5, 5) (10, 10) (15, 15) (20, 20). Right: (a) comparison between the calculated electronic DOSs for a (5, 5) (10, 10) (15, 15) (20, 20) 4WCNT and for the sum of the four SWCNTs constituting the 4WCNT, (b) difference between the two spectra reported in (a) [44].

of a simple graphene sheet (figure 8(a), left panel) with the metallic SWCNT (figure 8(b), left panel), more complex structures appear mainly due to band-folding effects [21]. Adding walls to the calculation increases the number of singularities and smooths out the DOS. Finally the 4WCNT structure turns out to be similar to the sum of the DOSs of each SWCNT composing the structure, showing that there is a rather small interaction among nanotubes belonging to the same multiwalled structure figure 8 (right panel). The results clearly indicate that multiwall carbon nanotubes made up of a reduced number of walls present different electronic properties from bulk graphite sheet systems. The presence of large van Hove singularities on both sides of the Fermi level ( $E_F$ ) together with the very small density of states at  $E_F$  may originate the interesting optical properties recently found [44] that will be discussed in this review.

#### 4. Methods of synthesis

The research activity on CNTs was at first restricted to microscopic and theoretical properties due to their limited availability. A marked turning point in nanotube applications was observed only after the development of well-established synthesis techniques that allowed CNT production in large quantities. The first synthesis methods used were techniques based on the vaporization of a block of graphite through an electric arc-discharge [45, 46] or laser beam [47], which allowed massive production of narrow sized SWCNTs.

In arc-discharge synthesis, carbon atoms are evaporated by a helium plasma initiated by high currents passed through an opposing carbon anode and cathode. The first success in producing a substantial amount of SWCNTs by arc-discharge was achieved in 1993 [45], by using a carbon anode containing a small percentage of cobalt in the discharge experiment. The method is currently used for producing both high quality MW- and SWCNTs.

In the ablation technique [47] a laser beam scans in a controlled way a metal-graphite composite target where the metal or metal-oxide can have variable concentration. The target is placed in a tube-furnace heated to 1200 °C. The soot produced by the laser vaporization is swept by the flowing Ar gas from the high-temperature zone, and deposited onto a water-cooled copper collector positioned downstream, just outside the furnace. This technique allows far better control over growth conditions compared with the arc-discharge technique, together with a greater yield and cleanliness of the nanotubes. Growth by arc-discharge and laser ablation requires that the material produced must be collected separately and subsequently deposited on a substrate to build-up the devices. In addition, typical by-products including fullerene, graphitic polyhedrons with enclosed metal particles, and amorphous carbon in the form of particles or over-coating on the CNT sidewalls are present in both growth methods. Therefore, for electronic device applications, the tubes need purification, which is much more costly than the production itself since there is no simple, routine method to measure purity. Such processing can also induce a

significant number of defects in the tubes. In this regard, new techniques for wet processing, cutting, and sorting are under constant development [48, 49].

#### 4.1. Chemical vapour deposition

A real improvement in synthesis technology was obtained from the use of the chemical vapour deposition (CVD) method, now probably the preferred technique for massive CNT production. In the CVD process metal catalyst nanoparticles supported by an inert substrate (quartz, silicon, alumina and others) are exposed to a flow of hydrocarbon source [50–52]. Initially, only iron family elements such as Fe, Co, Ni were considered to have a good catalytic function, due to the large bonding energy of carbon, but with time it was soon discovered that many other metals can be used. Since the systematic study reported by Yuan *et al* [53], that concluded that a large variety of metals including Fe, Co, Ni, Cu, Pt, Pd, Mn, Mo, Cr, Sn, Au, Mg, and Al can successfully catalyse the growth of carbon nanotubes, nowadays it is generally accepted that almost any metal nanoparticle can be used as catalyst for CNT growth. The essential role of the metal nanoparticles is to provide a platform on which carbon atoms can form a hemispherical cap, and then a carbon nanotube can grow in a self-assembled fashion. The basic elements of the growth process have been elucidated and the process is often described as driven by a high solubility of carbon in the metal catalyst solution at high temperature followed by carbon segregation and emergence from the catalyst surface [54]. The carbon in the particle links up to form graphene and wraps around the catalyst to form carbon nanostructures from the catalyst surface; these structures range from amorphous carbon to single-walled and multiwalled carbon nanotubes, depending on the type and size of the catalyst, and specific thermodynamic conditions [51–54]. The CVD process has many advantages with respect to arc-discharge and laser ablation methods. CVD operates between 600 and 1200 °C, unlike laser ablation techniques that require higher temperatures (around 4000 °C), and the CNTs can be grown on pre-patterned surface areas where the catalyst has been selectively deposited. In addition, by tuning the catalyst composition and the operating growth parameters, oriented CNTs can be obtained [55–57]. Figure 9(a) shows an image of regularly spaced arrays of nanotube towers grown on top of patterned iron squares on porous silicon substrates. The nanotubes can self-assemble into aligned structures during CVD growth, and the driving force for self-alignment is the van der Waals interaction between nanotubes. The nanotube towers exhibit very sharp edges and corners with no nanotubes branching away from the blocks. Figure 9(b) shows SWCNT networks formed by nanotubes grown from catalyst material placed on top of regularly patterned adjacent silicon towers. The tube structures are suspended bridges above the surface [56].

The CVD process was recently used for the growth of ultralong SWCNTs over 18.5 cm long on Si substrates using water vapour, ethanol, and H<sub>2</sub> as the feed gas, monodispersed Fe–Mo as the catalyst, and a superaligned

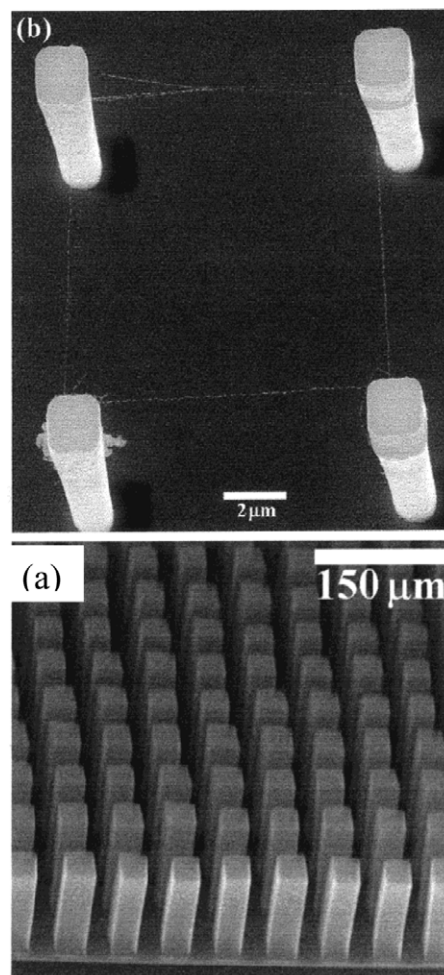


**Figure 9.** Scanning electron microscopy images. (a) Arrays of bundled multiwalled nanotube towers. Each tower-like structure is formed by many closely packed MWCNTs. The nanotubes self-assemble such that in each tower they are oriented perpendicular to the substrate. (b) A square of suspended SWCNT bridges. Reproduced with permission from [56]. Copyright 1999 American Chemical Society.

carbon nanotube (CNT) film as the catalyst supporting frame. Electrical transport measurements indicated that the electrical characteristics along a single ultralong SWCNT were uniform. It was also found that the maintenance of a spatially homogeneous temperature during the growth process was a critical factor for obtaining constant electrical characteristics along the length of the ultralong SWCNTs [57]. Transparent nanotube sheets were drawn from a sidewall of MWCNT forests previously synthesized by CVD. The nanometre scale thickness, transparency, flexibility, porosity, and high work function of the CNT sheets were used to demonstrate that they can be applied on flexible plastic and rigid substrates [58–60].

Continuous and massive production would be greatly facilitated if the substrate used for the CNT growth could play at the same time the role of support and catalyst, so as to be rapidly reused for subsequent growth processes. In this regard, stainless steel can fulfil this requirement. Camilli *et al* [61] found that two key parameters regulate the CVD process: the native nanoscale roughness of the substrate and the exclusive extraction of the Fe from the steel substrate

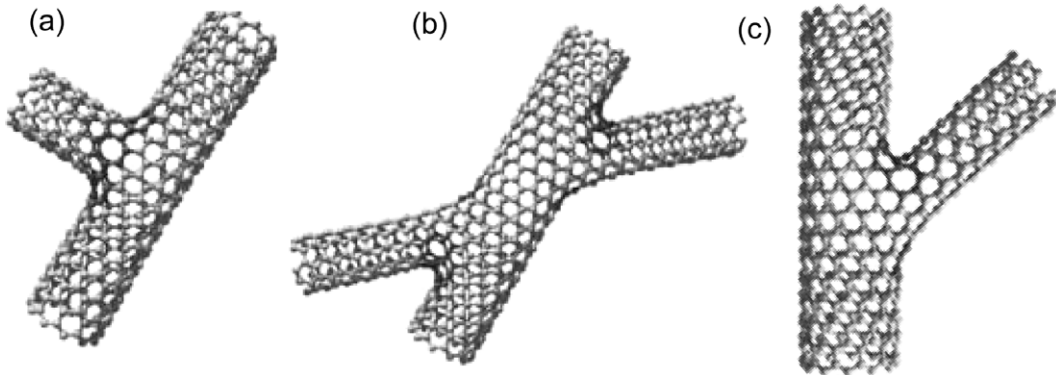


**Figure 10.** Carbon-based ideal junctions exhibiting (a) T, (b) X, and (c) Y geometries. (Adapted with permission from [74].) Copyright 2002 American Physical Society.

components (i.e. iron, chromium, nickel) as the only metal catalyst involved in the reaction mechanism. In addition, the stainless steel substrate can be reused for subsequent growth, after only carefully removing the synthesized CNTs. Over the years, remarkable advances have succeeded in significantly increasing the overall yield and control of the carbon nanotubes. There is still a major difficulty to overcome for the CNTs to be integrated in devices, namely the variety of nanotube structures that are simultaneously produced, where metallic and semiconducting CNTs are both present with different size distributions [48, 49]. There are applications such as nanotube field emitters or carbon nanotube-reinforced materials which do not require specific isolated tubes and are thus easier to realize.

#### 4.2. Structural defects in carbon nanotubes

The synthesized CNTs (either SW or MW) are sometimes far from the ideal systems considered in the theoretical models. CNT walls may contain chemical impurities and structural defects whose nature and density depend mostly on the synthesis method used. The chemical impurities are generally by-products such as amorphous carbon or fullerenes, as well as the remains of the primary materials used in the synthesis process, such as pieces of graphite from arc-discharge or catalyst metal nanoparticles from CVD. Hence, purification is part of the synthesis process; the most problematic step is to get rid of the undesired by-products without damaging the CNT structure [62]. The structural defects in CNTs are mainly atomic vacancies and interstitials. A vacancy is a deviation from the perfect hexagonal lattice arrangement due to the absence of one or more carbon atoms [63]. Other defects like pentagons, heptagons, Stone–Wales reconstruction [64], adatoms, or substitutional impurities have been proposed theoretically [65–67] and observed experimentally [68, 69]. Electron irradiation and strain might induce structural transformations in CNTs; these consist mainly of vacancies and interstitials [73–78] which can change the helicity of the nanotube and modify its electronic structure [64–71]. Although the majority of electronic applications require structurally perfect CNTs to maximize the electron mobility, defects can be useful for other applications. For example they are good anchoring

sites for foreign species such as single atoms, organic or inorganic molecules. The influence of defects induced by electron and ion irradiation in pristine carbon nanotubes has been studied experimentally [72] and theoretically [73]. As an example, the size and distribution of Au clusters on MWCNTs for gas-sensing devices greatly improves after the MWCNTs are exposed to oxygen–plasma irradiation [72]. While this kind of method has proved to be useful for gas-sensing devices it does not improve the electrical contact characteristics. Therefore it would be useless in light energy conversion applications. In fact, the presence of oxygen or other contaminants at the nanoparticle–CNT interface can be detrimental for the charge transfer processes regulating the optoelectronic devices’ response. Terrones *et al* [74] irradiated SWCNTs with electrons and induced a local covalent welding between tubes of similar diameters. Junctions of different shapes (denoted as T, X, and Y) were obtained and proved to be stable after formation, figure 10. Research into the controlled fabrication of nanotube-based junctions and network architectures exhibiting interesting electronic behaviour is in constant progress.

## 5. Characterization techniques

Several experimental techniques make it possible to measure the nanotubes’ morphological and electronic structure and also help to validate the synthesis process used.

Raman spectroscopy has historically played an important role in the study and characterization of graphitic materials [32–34, 75]. In principle, via vibrational frequency detection, Raman spectroscopy gives information on crystallite size, clustering of the  $sp^2$  phase, the presence of  $sp^2$ – $sp^3$  hybridization, the optical energy gap, elastic constants, doping, the presence of defects and other crystal disorder, the number of graphene layers, nanotube diameter, chirality, curvature, and finally the metallic versus semiconducting behaviour which makes carbon nanotubes unique. Besides, Raman spectroscopy has the advantage of being non-destructive for CNTs. Figure 11 reports typical Raman spectra obtained on SWCNTs, DWCNTs, MWCNTs and graphite. It can be noticed that the spectrum for each graphitic form shows a proper characteristic. In the spectra different contributions

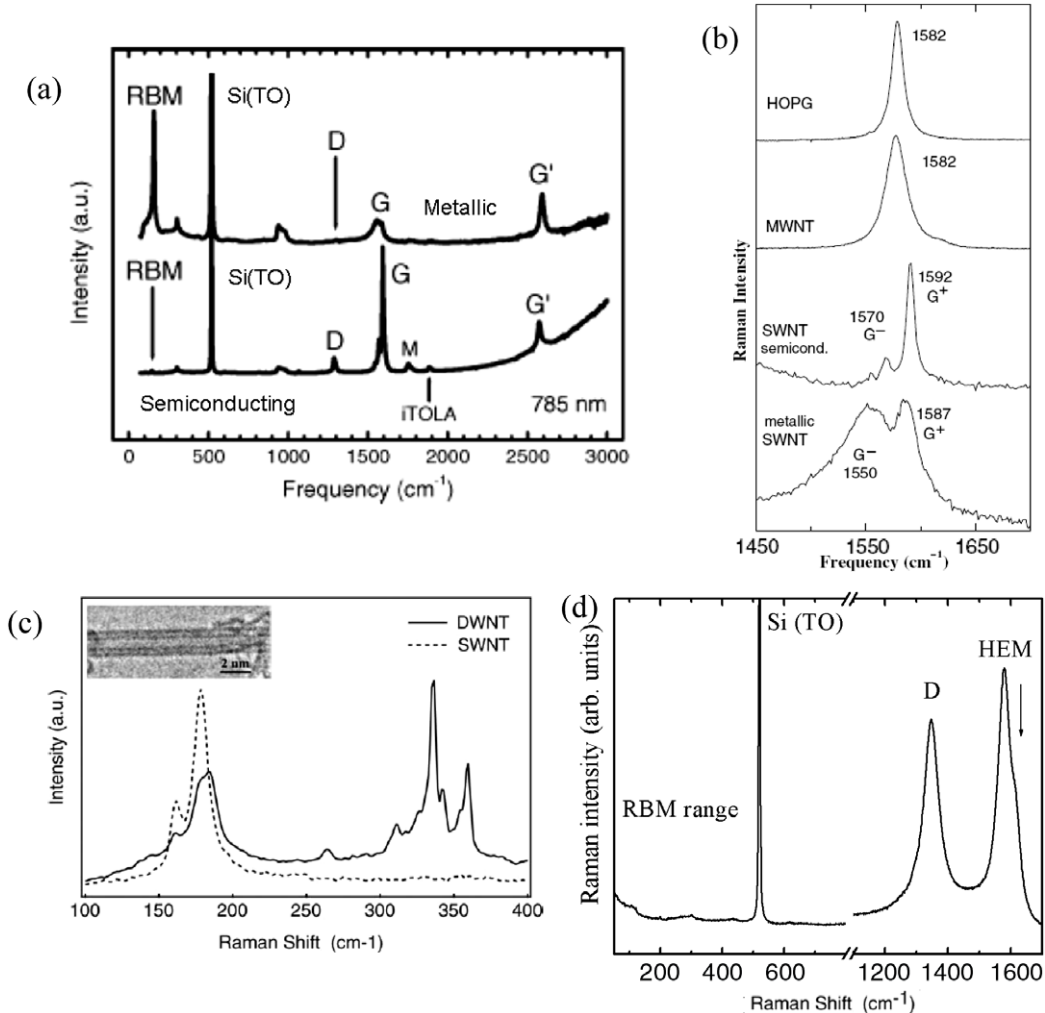


**Figure 11.** (a) Raman spectra from metallic and semiconducting SWCNTs using 785 nm laser excitation, showing the radial breathing mode (RBM), D-band, G-band, and G'-band features, in addition to weak double resonance features associated with the M-band and the iTOLA second-order modes. (b) G-band spectra for highly oriented pyrolytic graphite (HOPG), an isolated semiconducting nanotube and an isolated metallic nanotube [75]. (c) Raman spectra taken for the SWCNT (dashed line) and DWCNT (solid line) samples for an excitation wavelength of 1064 nm in the range of the radial breathing modes. Inset: TEM image of a typical DWCNT. Reproduced with permission from [42]. Copyright 2005 Elsevier. (d) Raman spectrum obtained from an MWCNT bundle using 514.5 nm laser excitation. No strong radial breathing modes are visible, unlike the SWCNT, while the high-energy mode (HEM) is split in a peak located at about  $1578\text{ cm}^{-1}$  and a shoulder at about  $1615\text{ cm}^{-1}$  [76]. The oxidized silicon substrate on which the tubes are deposited in (a) and (d) also contributes to the Raman spectra, denoted by Si (TO).

can be identified. The radial breathing mode (RDM), in the low energy range ( $100\text{--}300\text{ cm}^{-1}$ ), is due to the out-of-plane vibrations. The tangential (in-plane vibrations) band in the range from  $1520$  to  $1620\text{ cm}^{-1}$  gives two main peaks called the D-band that stems from disorder-induced modes in graphite and the G-band attributed to the ordered graphitic structures respectively. Figure 11(a) reports the typical Raman spectra for metallic and semiconducting SWCNTs. Figure 11(b) reports the G-band spectra for highly oriented pyrolytic graphite (HOPG), compared to those for isolated semiconducting and metallic nanotubes, and that of MWCNT, respectively.

In figure 11(c) the spectrum from an SWCNT is reported together with that from a DWCNT [42]. It can be noticed that the DWCNT spectrum has two additional peaks from which the inner and outer shell diameters can be determined. The values found are in good agreement with those obtained from

the TEM analysis, also reported in the inset of the figure. The contribution at low wave numbers is peculiar to the SW- and DWCNTs and allows direct evaluation of the tube diameter. In particular, a detailed analysis of all resonance Raman effects has been greatly aided by the introduction of the Kataura plot, which reports the interband transitions energies ( $E_{ii}$ ) as a function of the tube diameter ( $d_t$ ) for all values of  $(n; m)$  [26], showing that each nanotube has a single set of  $E_{ii}$  transition energies. Figure 11(d) reports the Raman from an MWCNT film. Unlike the SWCNT, in the low-energy range ( $100\text{--}300\text{ cm}^{-1}$ ) no strong radial breathing modes are observed. The high-energy range mode (HEM), equivalent to the transverse vibrations of the graphene planes, is split into a peak located at about  $1578\text{ cm}^{-1}$  and a shoulder at about  $1615\text{ cm}^{-1}$ . The graphene phonon mode at  $1578\text{ cm}^{-1}$  is not split. The vibrational mode at  $1615\text{ cm}^{-1}$  is typical of

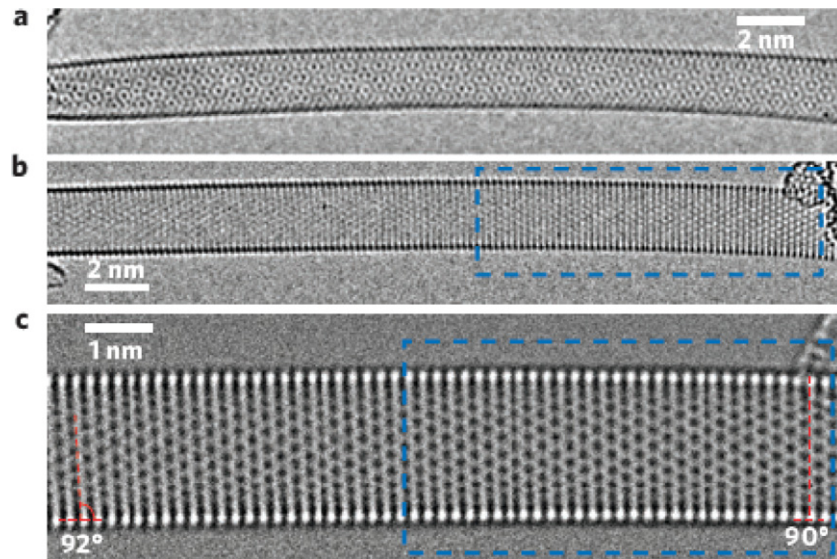


**Figure 12.** Low-voltage aberration-corrected (AC)-HR-TEM images of SWCNTs. (a) An (18; 8) SWCNT. (b) A (28; 0) zig-zag SWCNT suspended in free space with a bend. (c) Higher magnification of the area in (b) showing the full atomic structure [111]. Reproduced with permission from [81]. Copyright 2011 Nature Publishing Group.

defective graphite-like materials that have not been purified after the growth process [76].

The relationship between SWCNT geometry and electronic properties was later established by other optical techniques, such as absorption [29–31], photoluminescence [35] and spectrofluorimetry [36].

Electronic techniques can be usefully adopted to investigate the atomic structure of carbon nanotubes. The most important are scanning and transmission electron microscopy (SEM, TEM) [77–83], scanning probe microscopy (SPM) [22–25, 28] and electron diffraction [84, 85]; they are all able to provide information on the local chemical and physical characteristics of the samples with a resolution ranging from tens to fractions of a nanometre. SEM can scan large areas of the supporting substrate after the CNT growth, from which the coverage and density of the CNTs can be rapidly evaluated. In addition, the presence of carbonaceous products from the growth process can be localized. This check turns out to be useful for CNT device applications. Nevertheless, SEM has a limited spatial resolution and cannot ascertain whether the CNTs are single or multiwalled. This task can be performed by TEM, the most direct technique for accessing the micro-structures of nanotubes. The technique operates in transmission mode and allows the direct visualization of isolated as well as bundles of CNTs with high-resolution TEM (HR-TEM) as shown in figure 12 [81]. A direct measurement of the tube dimension can be obtained while the chiralities of individual tubes can be extracted from the electron diffraction patterns with adequate combination of the real space phase restoration and its Fourier transformation.

Recently a high-resolution imaging technique with single atom sensitivity has been developed. An example is reported in figure 13, where atomic defects in graphene layers have been recovered with the acquisition of optical diffraction patterns (Fourier transformation) completed by systematic image simulations [80].

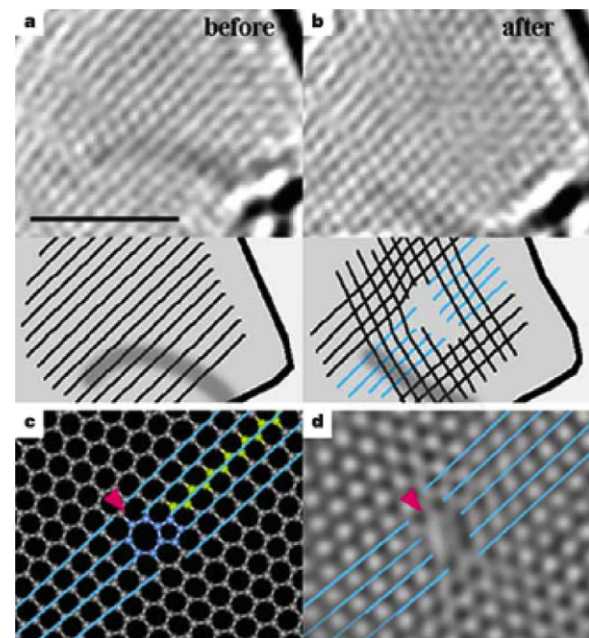


**Figure 13.** HR-TEM images of a graphene layer before (a) and after (b) a topological defect induced *in situ* by electron irradiation. An edge dislocation is unambiguously visible at the middle of the network where one zig-zag chain is missing. The missing zig-zag chain is shown schematically in the bottom part of each panel. (c) An atomistic model of the pentagon–heptagon pair in the graphitic network. (d) A simulated HR-TEM image shows a good comparison with the HR-TEM image in (b). Scale bar, 2 nm (adapted with permission from [80]). Copyright 2004 Nature Publishing Group.

TEM performed on MWCNTs allows direct evaluation of the outer diameter, the number of walls and the internal channel diameter, as shown in figure 14 [76].

Since the technique operates in transmission mode, the CNTs need to be carefully removed from the substrate and deposited on special grids for observation. Although CVD

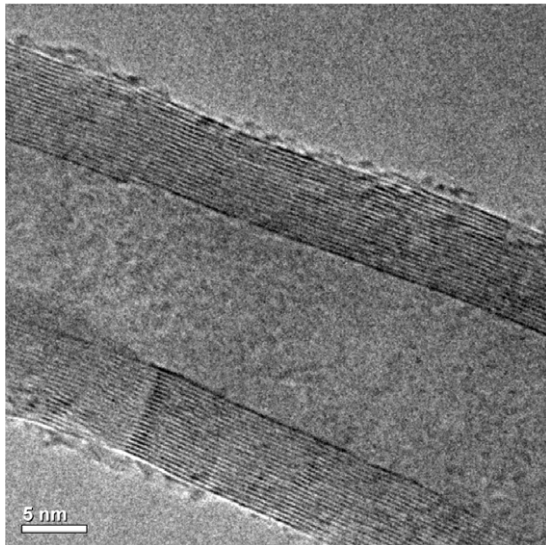


**Figure 14.** TEM image of a portion of an MWCNT, synthesized by CVD [76]. The outer and inner diameters can be evaluated together with the number of walls.

is the synthesis process of choice for industrial applications, the carbon-based product formed is strongly dependent on many different parameters. By using the same experimental growth conditions different morphologies or types of tube are often obtained, making a complete unified picture of the reaction process problematic. The same difficulty is experienced by the numerous proposed theories describing the growth mechanism of C-based nanostructures [51–54]. In this regard, TEM proves to be very useful for direct visualization of the CVD growth process. This can be achieved by acquiring a sequence of bright-field images, taken at specific time intervals starting from the observation of the catalyst particle and monitoring the CNT growth from carbon adsorption and decomposition followed by surface diffusion and nucleation at an elevated temperature [82, 83].

One major disadvantage of TEM, and to a lesser extent of SEM, is the damage produced by the long-term focusing of the electron beam. Depending on the specimen material the damage induced during a TEM measurement can take a variety of forms, including tube distortion, desorption, oxidization, reduction, polymerization and carbonization, all of these inducing unexpected experimental errors [86, 87]. When the TEM is equipped with an electron energy analyser, energy loss spectra in the transmission mode can be acquired at high spatial resolution [88].

Scanning probe techniques (SPM) are also used to study CNTs [22–25, 28]. Scanning tunnelling microscopy makes it possible to acquire images, at atomic resolution, of the tube and evaluate its diameter and the chiral angle. A direct measurement of the DOS close to the Fermi level can also be obtained when operating in the scanning tunnelling spectroscopy mode as shown in figure 6. Sometimes an ultra-low temperature is necessary in order to achieve good imaging conditions. Atomic force microscopy (AFM) has been applied not only for morphological characterization but also to study the mechanical [17] and/or electrical properties

of the CNT by means of the local interaction between the tube and the tip [89, 90]. This point will be illustrated in detail in the next section. The sample for SPM measurement must be carefully prepared and well dispersed on a flat substrate.

## 6. Transport properties of carbon nanotubes

Although the basic element of a carbon nanotube is the graphitic sheet, the electrical conducting properties of graphite appear only partially in nanotubes, which are electronic hybrids [91]. The most intriguing predicted property of SWCNTs is their semiconducting or metallic behaviour depending on their diameter, chirality and also small structural variations [9, 10].

Due to the complexity of making electric measurements on individual tubes, experimental studies were first performed on bundles of CNTs. Different experimental strategies such as conventional lithography, direct four-probe (or two-probe) contacts, AFM tip manipulation and others were applied to establish reliable electric contact with the nanotubes. There is an intrinsic difficulty in realizing the metal contact, and usually one of two different strategies is followed. One is to directly evaporate the metal on the tubes, at the risk of beam damage. The main advantage is that aligned contacts can be realized. The second method consists in depositing the CNTs on a prefabricated array of electrodes. Both methods need to be checked with SEM or AFM to obtain direct images of the substrate surface and find where the tube or rope happens to bridge the contacts.

The conduction properties of CNTs can be described using the two-terminal Landauer–Buttiker formula [92–94]. This states that for a system made up of a discrete number ( $N$ ) of 1D channels in parallel, the conductance  $G$  can be expressed as  $G = T(Ne^2/h)$ , where  $T$  is the transmission coefficient for electrons through the sample,  $e$  is the electron charge, and  $h$  is the Planck constant. If the electronic transport inside the CNT is ballistic with no energy dissipation in the conductor ( $T = 1$ ), each conducting channel contributes  $G_0$  ( $G_0 = e^2/h$ ) to the total conductance. Calculations performed on CNTs indicate that metallic SWCNTs have two conductance channels since the Fermi level crosses two energy bands, and taking into account the spin degeneracy the conductance  $G = 4G_0 = 4e^2/h = 155 \mu\text{S}$ . This value corresponds to a quantum resistance  $R_Q = 1/G \sim 6.5 \text{ k}\Omega$ . This means that the starting value of the contact resistance associated with the 1D CNT system is at least  $R_Q$ . Unfortunately, in real CNT-based systems the presence of both imperfect contacts and scatter centres that alter the mean free path of the electrons generates two additional contributions together with the fundamental resistance. Therefore the total resistance measured is approximately the sum of these three contributions.

Electron transport measurements on individual SWCNTs [95] have been performed on a  $\text{SiO}_2$  substrate where prefabricated electrode assemblies constitute the three metal electrodes. The SWCNT is positioned so as to contact two metal electrodes, and a third electrode acts as a gate, see figure 15. The current flowing in the tube is measured as a

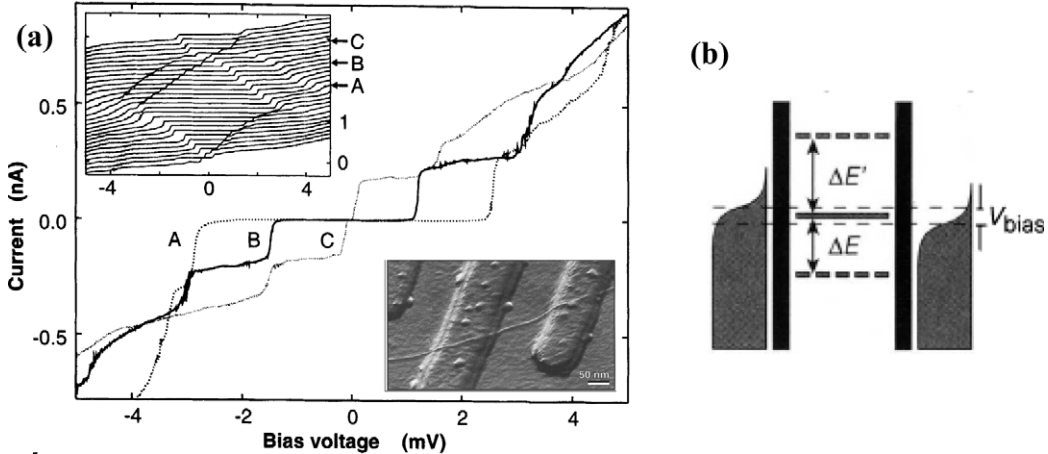


**Figure 15.** Current–voltage curves of an SWCNT at  $V_{\text{gate}} = 88.2$  mV (a), 104.1 mV (b) and 120 mV (c) at 5 mK. The inset in the top-left corner shows more  $I-V_{\text{bias}}$  curves. The variation with  $V_{\text{gate}}$  of the gap around zero bias voltage implies Coulomb charging of the tube. The inset in the bottom-right corner shows an AFM image of an SWCNT on top of a SiO<sub>2</sub> substrate with two 15 nm-thick Pt electrodes. A  $V_{\text{bias}}$  is applied to the metal contacts while the gate voltage  $V_{\text{gate}}$  is applied to a third electrode in the upper-left corner of the image. (b) Schematic of the density of states of the CNT in contact with the continuous states of the metal electrodes (adapted with permission from [95]). Copyright 1997 Nature Publishing group.

function of the applied bias voltage. A voltage can also be applied at the gate in order to modulate the transport through the tube.

From the current–voltage response obtained on a metallic SWCNT at different applied gate voltages it can be noticed that around zero applied bias the current is zero, while a sequence of peaks in the current appears at higher applied voltages. These oscillations have been shown to result from Coulomb blockade or single-electron charging and resonant tunnelling. The single-electron charging occurrence requires that two conditions must be fulfilled: (1) the value of the contact resistance must be larger than the quantum resistance ( $R_Q = h/4e^2$ ), mainly due to the poor contact between the CNT and the metal, thus confining the 1D wire of finite length into a ‘quantum dot’ and (2) if this ‘dot’ is small its total capacitance  $C$  is small as well and the energy required to add an electron to the system,  $E_C = e^2/2C$ , is larger than the thermal energy  $K_B T$ . Therefore for measurements performed at low temperature for which  $E_C \gg K_B T$ , the current is locked and it can flow in the tube only when the applied bias is greater than  $e/2C$ .

Under this regime the transport occurs by means of individual electrons. Figure 15(b) shows a schematic of the density of states of the CNT in contact with the continuous states of the metal electrodes. The electron states in the CNT are discrete due to the finite length of the tube. When a discrete state of the CNT is aligned with the Fermi level of the system, resonance tunnelling occurs and the electrons are delocalized over the CNT length.

Similar measurements have been performed on small SWCNT ropes. A drop of solution containing SWCNTs is deposited on a thick SiO<sub>2</sub> substrate. Subsequently the surface is imaged with AFM [89–96] to localize tubes bridging between two or more metal contacts, see the inset of figure 16(a).

The current–voltage curves obtained at room temperature depend strongly on  $V_{\text{gate}}$ ; for negative  $V_{\text{gate}}$  the  $I-V$  traces are

linear, whereas as  $V_{\text{gate}}$  becomes more positive they are highly nonlinear with an increasing bias threshold. This behaviour may be explained qualitatively if conduction occurs through a semiconducting tube, so that the device behaves as a field effect transistor. The measured conductance ( $G$ ) at room temperature as a function of the applied gate voltage for two different tubes is reported in figures 16(b) and (c). The conductance is independent of the applied gate voltage ( $V_{\text{gate}}$ ) in (b), and dependent on  $V_{\text{gate}}$  in (c). The former finding can be understood if the nanotubes in the rope are mainly metallic. If this is the case the expected energy dispersion curve  $E(k)$  near the Fermi level  $E_F$  (as indicated in the inset of figure 16(b)) indicates that there is no energy gap. Therefore changes of the gate voltage have little or no influence on the electrons close to the Fermi level. The maximum value of the conductance found is around  $3G_0$ , close to the theoretical predicted value of  $4G_0$ . The second behaviour observed (figure 16(c)) shows decreases for positive applied  $V_{\text{gate}}$  and increases for negative applied  $V_{\text{gate}}$ . This trend can be explained if conduction occurs through semiconducting tubes, as seen in the  $I-V$  response in (a), whereby the device behaves as a field effect transistor where the charged carriers are holes and hence the Fermi energy level in the tube is near to the bottom of the band gap (inset to figure 16(c)).

When the measurements are performed at lower temperature the conductance displays a variety of different trends mainly originating from the number of NTs involved in the conduction process, see figure 17. On average the observed oscillations in the conductance indicate that a Coulomb blockade process takes place. In the intermediate temperature range, a key manifestation of the presence of the Luttinger liquid (LL) state is the existence of a power-law dependence of the tunnelling conductance on temperature  $G \propto T^\alpha$ . The observed behaviour matches the predictions for strongly correlated one-dimensional electron systems [90].

In 1994, Langer *et al* carried out the first transport measurements on bundles of MWCNTs, using two gold

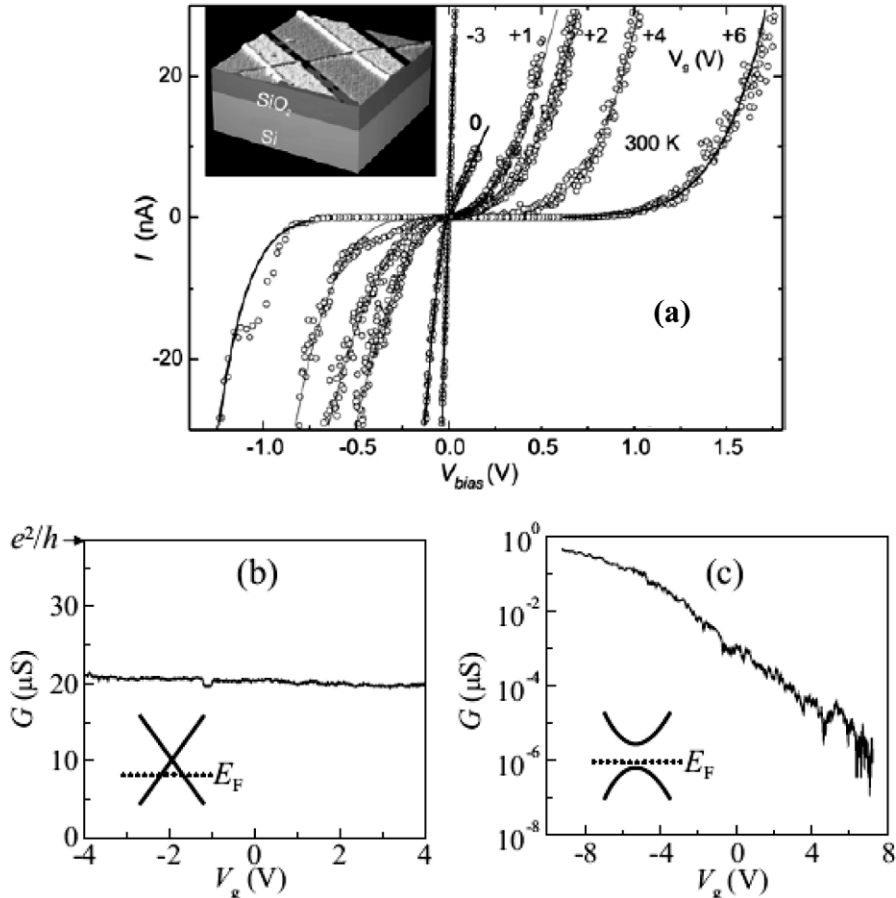


**Figure 16.** (a) The nanotube transistor ‘TUBEFET’. Main: room temperature  $I$ - $V$  traces measured in vacuum for a semiconducting nanotube device at a series of gate voltages. Inset: AFM image showing the nanotube lying across platinum electrodes. The gate voltage is applied to the n+ doped Si underneath the 300 nm-thick SiO<sub>2</sub> layer. (b), (c) Conductance versus  $V_{gate}$  at room temperature for two devices. The insets are schematic drawings of the energy dispersion  $E(k)$  near the Fermi level for a metallic (armchair) tube (b) and a semiconducting tube (c) (adapted with permission from [89]). Copyright 1999 American Institute of Physics.

contacts deposited by lithographic techniques. The measured bundle resistance changed as a function of the temperature (2–300 K) and turned out to be well described by a simple two-band semi-metal model [97]. Direct four-probe contact measurements on aligned bundles of MWCNTs [98] showed that they behave as conducting materials and exhibit anisotropy with respect to transport properties for different nanotube alignment configurations [99]. Transport measurements made on various individual MWCNTs showed metallic, semiconducting, and semi-metallic electronic behaviour [100–103], with a very short mean free path for the conduction electrons, most likely due to scattering from defects. Meanwhile other studies have found that the transport is Ohmic [104]. The conductance of MWCNTs was found to be quantized even at room temperature [105]. In the experiment the tip of a scanning probe microscope was replaced with a nanotube fibre. Thanks to the piezoelectric movement of the microscope the fibre could be lowered into a liquid metal to establish a gentle electrical contact with a nanotube at the end of the fibre. In another AFM experiment performed in a solution containing MWCNTs well dissolved in poly-chlorinated biphenyls (Aroclor 1254), the tip was used to ensure the electric contact with the NT and directly measured the conductance. A quantized conductance was

found in both experiments. This result was expected due to the nearly one-dimensional CNT nature. The conductance value found at room temperature for the MWCNTs varied from 1 to  $2G_0$  of the quantum conductance. Since each MWCNT wall can have different helicity, there is no simple interpretation and theoretical prediction of transport properties.

In principle an MWCNT behaves as a conductor, because the band gap of a CNT has been predicted to decrease with increasing tube diameter [26]. Therefore, MCWNTs with diameter greater than 10 nm are expected to show metallic rather than semiconducting behaviour at room temperature.

As a result, the current at low applied bias and temperature in a bulk-contacted MWCNT flows only through the outermost shell [105]. When at least the outer wall is conducting, it is not easy to understand what happens to the rest of the layers. Incommensurate character of the stacking of the different shells and momentum conservation requirements both lead to weak coupling between the shells of an MWCNT. If the next-to-top layer is insulating, then this layer and the deeper ones will not contribute to the conductance. Due to geometrical and energy considerations it is possible that a conducting layer is usually followed by a non-conducting one. This will impose conditions on the layer helicity and hence on the conductance properties. It is also possible that the outer

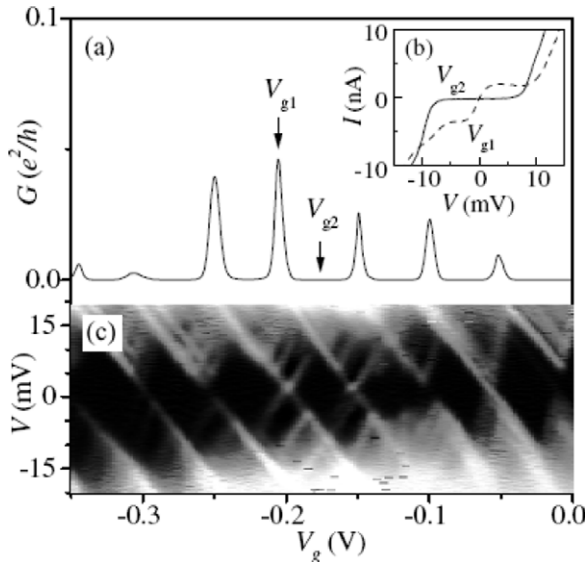


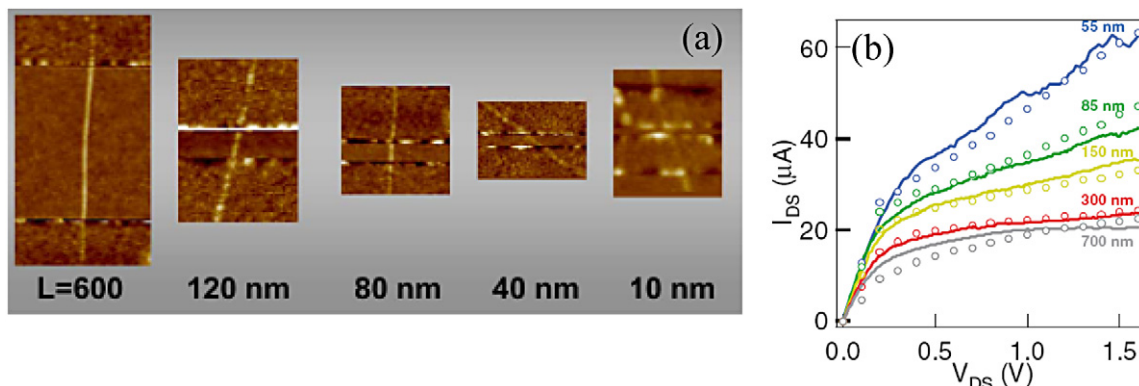
**Figure 17.** (a)  $G-V_g$  for a device at 4.2 K showing periodic Coulomb blockade peaks. (b)  $I-V$  characteristics taken at the centre of a peak ( $V_{g1}$ ) and in between peaks ( $V_{g2}$ ). (c) Grey scale (bias spectroscopy) plot of  $dI/dV$  versus  $V_g$  and  $V$  at 4.2 K in the same range of  $V_g$  (lighter = more positive). Reproduced with permission from [89]. Copyright 1999 Springer.

layer would be the only one to participate in the conduction process because the resistivity perpendicular to the tube axis is very high and consequently the layers are effectively insulated from each other.

The results discussed so far show that CNTs are excellent wires, with an experimentally measured conductance very close to ideal. At first, the majority of electrical transport experiments report a very high contact resistance between the CNT and the metal. Therefore the applied voltage drops almost entirely across the contacts; as a consequence tunnelling dominates the transport and single-electron charging related phenomena are manifested at low temperature. At relatively high temperatures, the transport characteristics appear to be

described by tunnelling into the so-called Luttinger liquid. In terms of transport, the electrons in the CNTs are expected to have a mean free path considerably longer than in higher dimension systems, since electrons can only scatter either backward or forward in the quasi-one-dimensional tube. The measured electron mean free path is also related to the applied electric field and can reach 1  $\mu\text{m}$  for low electric fields down to 15 nm at high electric fields [106]. The main processes that could influence the transport properties and decrease the conductance are surface scattering, defect and phonon scattering, and disorder. All them seem ineffective and the reasons for this are various, hence CNTs are potentially ballistic conductors. Since the elastic scattering in CNTs is weak, the inelastic scattering determines the transport properties.

Surface scattering can be excluded since the nanotube has a crystalline surface without disordered boundaries. It must be noted that the presence of structural defects significantly affects the measured conductance as observed for metallic nanotubes. It has been found that the conductance of argon ion bombarded CNTs is strongly reduced [72, 73, 107], thus demonstrating that structural defects affect the conduction process. In metal-CNTs the electrons in the crossing bands have a large velocity ( $8 \times 10^5 \text{ m s}^{-1}$ ) compared to the phonon sound velocity. This, coupled with the small final density of states for scattering, makes the probability of scattering with acoustic phonons very low. The dominant scattering mechanisms are due to the zone boundary and optical phonons with energies of approximately 160 and 200 meV; however, at room temperature and low applied bias, electrons do not acquire high enough energy to emit such a phonon; therefore scattering with these phonons is ineffective. From the above, there must be a tube length limit beyond which the transport behaviour changes from ballistic to diffusive and is eventually localized when disorder sets in. Improvements in the contacts between the metal and CNT help in understanding whether the electron transport in the tubes is ballistic or dominated by scattering processes.



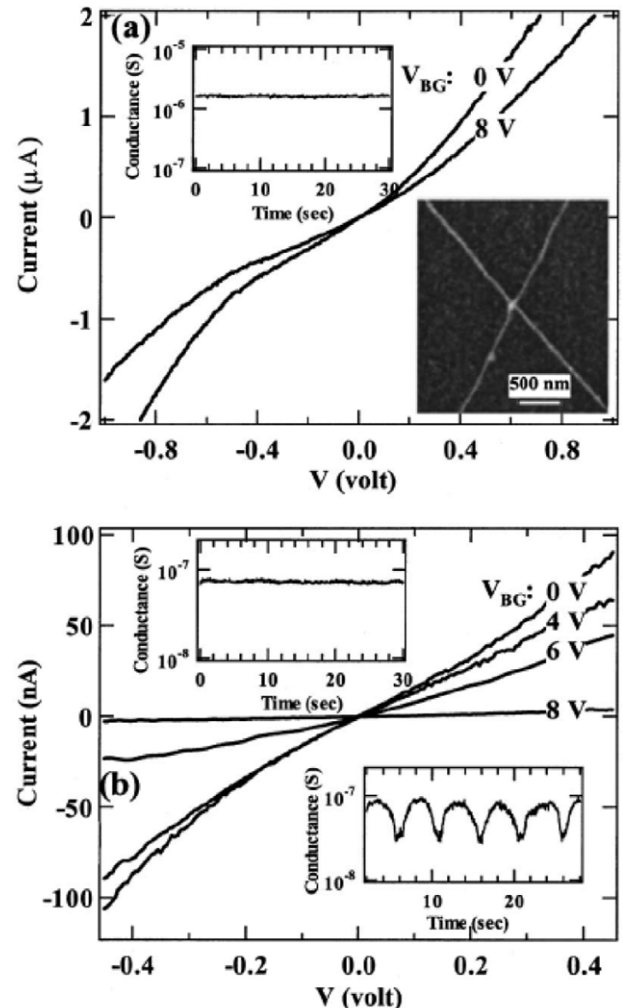
**Figure 18.** (a) AFM images of five devices consisting of individual SWCNTs with lengths in the range of  $L = 600$ –10 nm between the edges of Pd contact electrodes. (b) Electrical properties of ohmically contacted metallic SWCNTs of various lengths. The solid lines are experimental  $I_{DS}-V_{DS}$  curves and the symbols are Monte Carlo calculation and fitting results (adapted with permission from [108]). Copyright 2004 American Physical Society.

Figure 18 shows the AFM image obtained on five devices made of individual SWCNTs of length ranging from 10 up to 600 nm bridged between Pd Ohmic contacts and laid on a heavily p-doped Si substrate used as the back gate covered with thermally grown  $\text{SiO}_2$  as the dielectric gate [108].

Electron transport experiments have been performed by applying a voltage bias on the device and registering the current. Transport properties of metallic SWCNTs of different lengths, in the low and high-bias regimes, are reported in figure 18(b). The symbols in the figure correspond to the Monte Carlo simulation of the transport process involved. At room temperature and in the low-bias regime, shorter tubes have higher conductance than the longer ones; therefore they are ballistic. In the high applied bias regime, the current saturates around  $60 \mu\text{A}$  for shorter tubes, while for longer tubes the saturation current reduces to  $20 \mu\text{A}$ , due to optical or zone-boundary phonon scattering. The conductance versus gate voltage for a tube 60 nm long recorded at various temperatures shows that it is essentially independent of temperature except for the appearance of conductance oscillations below 40 K. This result suggests that electron backscattering by acoustic phonons is negligible and that in the low-bias regime transport within this tube length is ballistic even at room temperature.

Special attention has been devoted to understanding and controlling the properties of semiconducting CNTs. These nanotubes are an attractive option for various electronic devices operating at room temperature, such as high speed transistors and Schottky diodes [109]. Therefore it is important to describe the physics of nanotube/metal contacts and the implications for electron transport [110, 111]. Theoretically, it is expected that the contact will either be Ohmic or form a Schottky barrier, depending on the work function difference between the metal and the NT and also on the CNT bandgap. One may expect that an Ohmic contact is formed for metals with work functions greater than 4.8 eV, like Au (5.5 eV) and Pd (5.1 eV). While the contacts are essentially planar in current devices, in the case of CNT–metal systems different contact geometries can be found. The simplest contact geometry studied is that obtained on SWCNT crosses or individual tubes directly grown on  $\text{SiO}_2/\text{Si}$  substrate. An atomic force microscopy tip is used both to image the tubes and as a local gate [112]. During repeated scans, the current is measured as a function of time while applying a constant bias voltage across the tube. As reported in figure 19, it is possible to identify the metallic or semiconducting nature of the crossing nanotubes from the  $I$ – $V$  curves obtained.

Experiments using an atomic force microscope tip as the electrical scanning probe along a p-type CNT bridged between two Cr–Au contacts [113] register the current between the tip and the contact electrode before and after annealing the contact. As reported in figure 20, the  $I$ – $V$  behaviour is rectifying before annealing, indicating the presence of a Schottky barrier, while it becomes linear when the contact is Ohmic, probably because of the Au diffusion due to the annealing in the Cr film contacting the tube. This result was also confirmed by cooling the device, which showed an increase in conductance.



**Figure 19.** (a)  $I$ – $V$  characteristics of a metal–metal SWCNT cross. Left inset: scanning probe gating results on one of the M-SWCNTs. Right inset: AFM image of the cross. (b)  $I$ – $V$  characteristics of a metal–semiconductor SWCNT cross. Top right and bottom left insets: scanning probe gating results on the M-SWCNT and S-SWCNT, respectively. Reproduced with permission from [112]. Copyright 2000 American Institute of Physics.

Similar results have been obtained for field effect transistors built with an individual semiconducting CNT and Pd contacts, for tubes of different length [114]. The measured conductance for a 300 nm tube approximately reaches the maximum value ( $4e^2/h$ ), thus indicating that no barrier exists at the contact. This behaviour is further confirmed from the temperature dependence of the conductance reported in figure 21. The conductance increases with a reduction in the temperature, opposite to what happens in Schottky barrier contacts, where the current increases with the temperature as reported elsewhere [115].

Studies on films of CNTs have also been reported. A factor that makes CNT films complex is that they contain both metallic and semiconducting tubes. In addition, since the semiconducting tubes are frequently doped, both kinds of tubes can carry current. Films of CNTs contacted with Ti/Au source and drain electrodes are scanned with a metal-coated

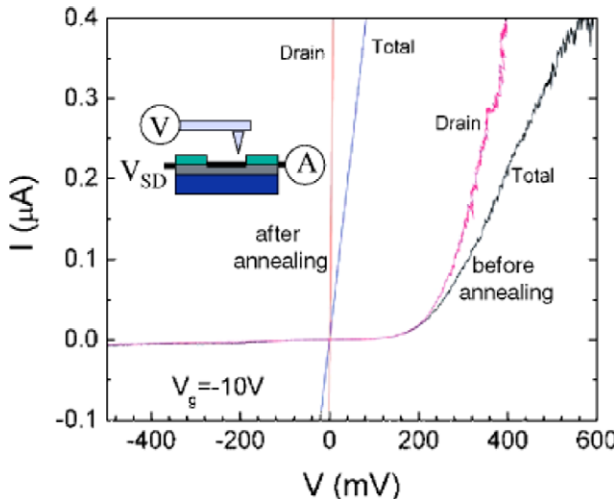


**Figure 20.** Current–voltage curves for a device with Cr–Au contacts before and after annealing. The voltage  $V$  refers to either the total voltage  $V_{SD}$  across the device or the voltage measured by the AFM tip 50 nm from the drain lead. Inset: measurement configuration. Reproduced with permission from [113]. Copyright 2004 American Physical Society.

AFM tip, and the surface potential that results from current flow in the device is imaged, see figure 22 [116].

Large variations in electrical performance from two devices fabricated one immediately next to the other are found, see figures 22(b), (c). The colour scale of the image corresponds to the measured voltage of the film and shows in case (b) a potential gradient starting near the bottom electrode with a relatively high resistance, while in (c) there is a smooth voltage drop between drain and source and a much lower resistance is found. There are substantial statistical fluctuations in the conductivities of the networks. Films with identical tube density and length but different in relative tube position show dramatic changes in the electrical characteristics as well as in the spatial patterns of flow and voltage drop. Theoretical simulations of the device determined that these drops arise from current being narrowed down to single percolative paths [117] at certain points in the film. In particular, changing the relative percentage between metallic and semiconducting tubes shows

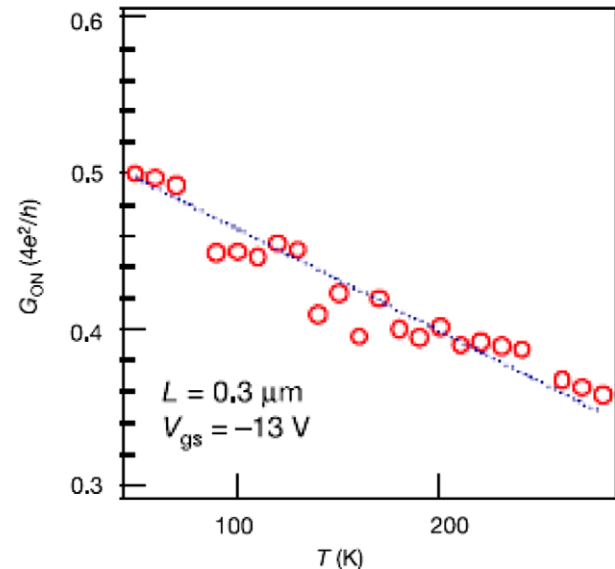


**Figure 21.**  $G_{ON}$  versus  $T$  for an  $L = 300$  nm semiconducting tube down to  $\sim 50$  K. Reproduced with permission from [114]. Copyright 2003 Nature Publishing group.

that two main electronic phases are identified: one where transport through the CNT film is modulated by the Schottky barrier formation and another where pure semiconducting paths connect source to drain, thus allowing transport in the device figure 22(d). These results underline the difficulty in realizing devices based on films of CNTs since a film contains both metallic and semiconducting tubes, although there are two semiconducting tubes for every metallic tube in a typical ensemble with uncontrolled chirality. Since the semiconducting tubes are frequently doped, both kinds of tubes can carry current, although percolative paths through the semiconducting tubes are preferable to those in the metallic tubes. Several approaches have been applied to improve the control of film composition and the overall reproducibility of the device. All approaches aim at: (1) increasing the presence and contribution from the semiconducting tubes and (2) reducing the metallic shorts to open more flowing paths and (3) favouring the overall electron mobility [118–122]. The conductivity of a nanotube can be altered by directly doping

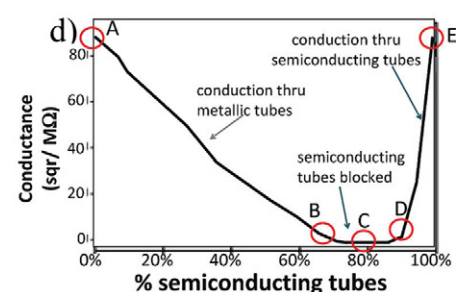
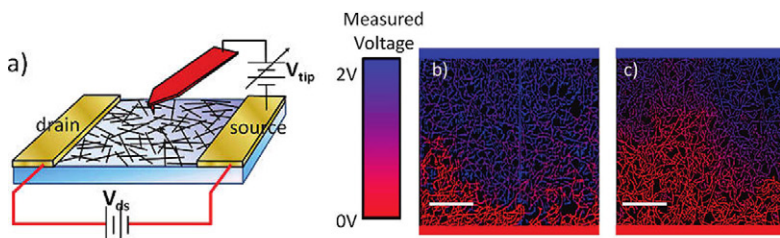


**Figure 22.** (a) Schematic showing the measurement technique used to image voltage drops in CNT films. (b), (c) Experimental images of nominally identical devices ( $40 \mu\text{m} \times 40 \mu\text{m}$ , same average tube length, density, diameter, and type). Panel (b) shows a large potential ‘cliff’ near the bottom electrode and exhibits a relatively high resistance of  $630 \text{ k}\Omega$ , while panel (c) displays a smooth voltage drop between drain and source and a much lower resistance of  $65 \text{ k}\Omega$ . (d) Expected conductance as a function of proportion of semiconducting tubes (adapted with permission from [116]). Copyright 2009 American Chemical Society.

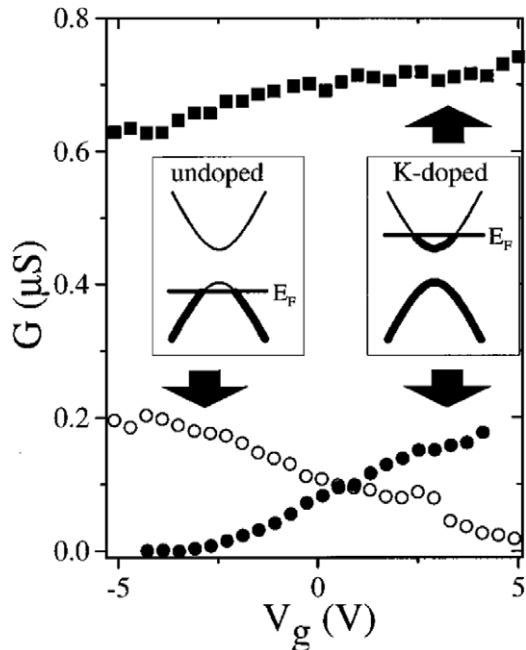


**Figure 23.** Open circles: conductance versus gate voltage for an undoped nanotube rope. The conductance increases with decreasing gate voltage, indicating p-type behaviour. The left inset shows a schematic band-structure diagram corresponding to this situation. Filled squares: conductance of a different sample after doping with potassium. Filled circles: the same sample after a cycle of deintercalation and re-intercalation at a lower doping level. The conductance increases with increasing gate voltage, indicating n-type behaviour. The right inset shows a schematic band-structure diagram corresponding to this situation. Reproduced with permission from [125]. Copyright 2000 American Physical Society.

the tube. It has been found that the addition of boron [123] and nitrogen to MWCNTs creates metallic features in the electronic density of states [124]. SWCNT ropes have been doped with alkali and halogen dopants which enter the interstices between the tubes in ropes [125–128]. A sizeable charge transfer process between the tubes and the dopants is set up, this increasing significantly the electrical conductivity. The doping effects produced on metallic or semiconducting SWCNTs can be different. Studies on the effects of potassium doping on the conductance of individual semiconducting single-walled carbon nanotube ropes demonstrate that it is possible to control the level of doping by reversibly intercalating and deintercalating potassium. The doping changes the carriers in the ropes from holes to electrons, see figure 23 [125].

One of the first devices built with doped CNTs was developed using an SWCNT deposited between two metal contacts patterned on a  $\text{SiO}_2$  substrate. The starting CNT was approximately  $3.5\ \mu\text{m}$  long and had a diameter of  $2\ \text{nm}$  [126]. Preliminary conductance measurements showed that it behaved like p-type semiconductor. One half of the tube was then covered with a thick polymethylmethacrylate (PMMA) coating, while the uncovered half was exposed to potassium, which is an electron donor. As shown in figure 24, the associated current–voltage response from such a device shows a negative differential resistance.

It must be emphasized that chemical doping introduces additional states or changes in the band gap, thus influencing the near intrinsic properties of nanotubes. A local p–n junction on an SWCNT can be formed by applying an external electrostatic potential [129] (see also figure 31, next section). This result is obtained using standard optical lithography and metal deposition techniques to form an additional pair of split gates buried in the  $\text{SiO}_2$  substrate, leaving the rest of the device similar to others.

The presence of defects can influence the electronic properties of the CNTs [73, 74, 130–135]. As an example Yao studied the electronic response from an individual SWCNT where a sharp kink was observed with AFM [130]. Figure 25 reports the AFM image of a CNT that contains a single kink.

The presence of this kink can be associated with the existence of pentagon and heptagon defects which join two nanotube pieces with different diameters and chiralities. The corresponding current versus applied bias curve, obtained at 100 K, is reported in figure 25(c), and shows a rectifying behaviour, while the curve in the inset obtained on the tube's upper straight segment measures a low resistance value and the absence of a gate effect, thus indicating that this segment is metallic. Therefore the system is made up of a metallic tube joining a semiconducting tube with a Schottky junction formed at the kink. The electronic transport in the presence of a Schottky barrier implies that the current injection across the contact, at room temperature, is dominated by thermionic emission while tunnelling does not play an important role.

Defects also influence the charge transport properties especially at room temperature [132]. Collins *et al* [133], using STM and STS, demonstrated that the transport on bundles of SWCNTs is similar to that observed in graphite; in other words, SWCNTs are semi-metallic. Nevertheless, as the STM tip moves along the nanotube, rapid changes in the  $I$ – $V$  curve are observed. This behaviour is ascribed to the presence of structural defects in the graphene lattice.

Castrucci *et al* [134] characterized by STM straight and coiled SWCNTs synthesized by laser vaporization dispersed on highly oriented pyrolytic graphite (HOPG). The straight tubes exhibit a uniform conductance along their axis, while a significant conductance modulation along the axis of two tightly bound and coiled nanotubes in correspondence to hills and valley-like regions is observed, see figure 26. The results suggest that changes at the nanometre scale in the electronic properties of the tubes are possible, meaning that in an individual nanotube a sequence of nanojunctions can coexist as theoretically predicted [135].

A metallized AFM tip has been used as a local gate to probe the conducting properties of a metallic SWCNT [136]. Applying a voltage to the AFM tip while scanning the sample at a fixed height allows the direct evaluation of the CNT resistance along the tube. The resistance response found shows some peaks that can be attributed to a resonant electron scattering that originates from localized defects in the nanotube [135].

CNTs are an attractive option for various electronic devices such as high speed transistors and Schottky diodes [137]. Field effect transistor (FET) devices based on

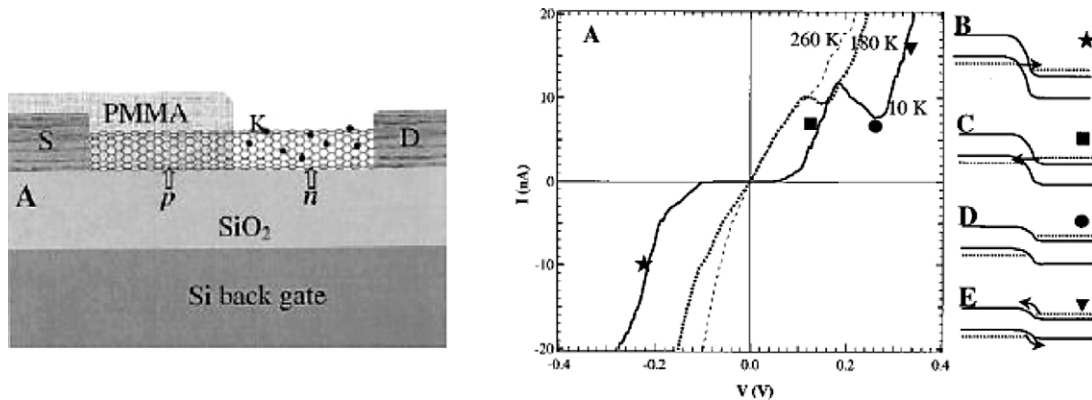


**Figure 24.** Schematic of the chemically doped CNT p–n junction and the associated  $I$ – $V$  curve response. Reproduced with permission from [126]. Copyright 2000 The American Association for the Advancement of Science.

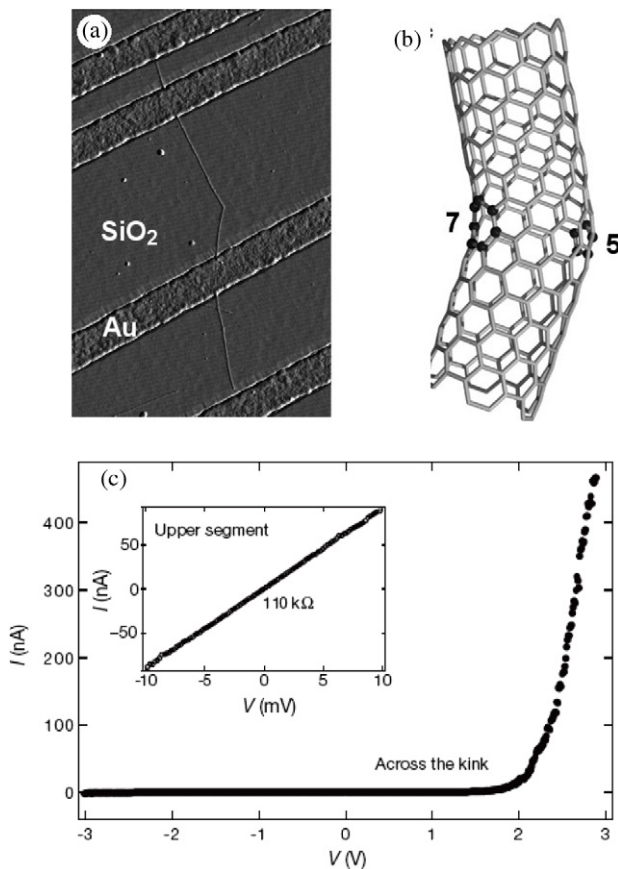


**Figure 25.** (a) AFM image of a CNT on top of three electrodes. (b) Illustration of the carbon-bond network of a kink junction constructed between an ‘armchair’ tube and a ‘zig-zag’ tube, where 5 denotes a pentagon, 7 denotes a heptagon, and the atoms in the pentagon and heptagon are highlighted by dark balls. (c)  $I$ – $V$  characteristics across the metal–semiconductor junction of (a), showing rectifying behaviour. The data are taken at 100 K. The results at room temperature are similar, but the data are noisier. Inset: the  $I$ – $V$  curve for the upper straight segment measured at room temperature. The low resistance value and the absence of a gate effect indicate that this segment is metallic. Reproduced with permission from [130]. Copyright 1999 Nature Publishing Group.

SWCNTs were first fabricated in 1998 [138–143]. One or more semiconducting CNTs play the role of the ‘channel’, while the two metal electrodes act as the ‘source’ and ‘drain’

electrodes [138]. The device consists of an SWCNT bridging two metallic electrodes deposited on a thick gate oxide film on a highly doped Si wafer, used as a back gate. The source–drain (SD) current  $I$  through the NT was measured at room temperature as a function of the bias voltage  $V_{SD}$  and the gate voltage  $V_G$ . Figure 27(a) shows the  $I$ – $V_G$  response for different source–drain voltages. The observed behaviour is similar to that of a p-channel metal–oxide–semiconductor field effect transistor (FET). The source–drain current decreases strongly with increasing gate voltage: this not only demonstrates that the CNT device operates as a field effect transistor but also that transport through the semiconducting SWCNT is dominated by positive charged carriers (holes). The conductance of the SWCNT-FET can be modulated by more than five orders of magnitude (see the inset of figure 27(a)).

Besides, a similar MCWNT-FET device has been tested [138]. Since the band gap of CNTs has been predicted to decrease with increasing tube diameter [26], MCWNTs with diameter greater than 10 nm are expected to show metallic rather than semiconducting behaviour at room temperature. Different MCWNT devices showed no gate action as shown in the  $I$ – $V_G$  curve plotted in figure 27(b) (curve (A)). For CNTs collapsing radially into a flattened tube with bulbs on either edge, in a geometry that balances the curvature energy with the interlayer interaction (‘collapsed’ tubes), as verified by AFM observation, a change in their electronic properties is observed, leading to a significant gate effect (curve (B) in figure 27(b)) similar to the SWCNT-FET. The  $I_{SD}$  current of this MCWNT-FET decreases with increasing gate voltage, i.e., the dominant conduction process is hole transport. It is possible to tune the  $I$ – $V$  response from an MCWNT/Si heterojunction by simply changing the doping of the Si substrate. In particular, a rectifying  $I$ – $V$  behaviour for lightly doped p-type Si (p-Si) was found [140] and linear characteristics (Ohmic) for highly doped p-Si [141].

It is well known that the feature sizes in Si integrated circuits are continually diminishing. The greatest demand is for horizontal interconnected devices. This application is much more difficult to satisfy, as horizontally directed nanotube growth can be achieved, but not with high reliability and yield. The key advantage of CNT-FETs over Si-FETs is

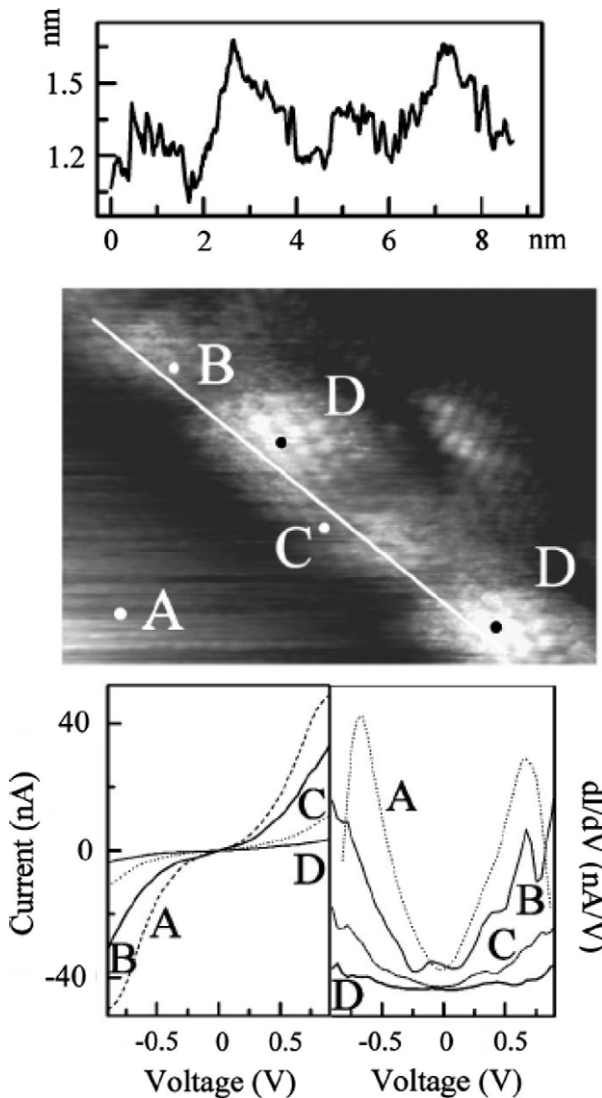


**Figure 26.** STM image ( $5 \times 5 \text{ nm}^2$ ) of two nanotubes twisted together. The upper panel shows the line profile along the white line drawn on the STM image. The lower panels show the  $I$ - $V$  curves recorded around points A, B, C, and D, respectively, and the corresponding  $dI/dV$  curves obtained by differentiation ( $I_{\text{tunnel}} = 1 \text{ nA}$ ,  $V_{\text{tip}} = 0.1 \text{ V}$ ). Reproduced with permission from [134]. Copyright 2004 Applied Physics Letters.

the lower operating voltage and size that allows the fabrication of dense aligned arrays at a reduced dimension. The FET performance can be improved using purely semiconducting CNTs in a film or highly oriented CNTs, thus limiting the high resistance tube–tube junctions prevalent in randomly oriented CNTs. In an FET metallic tubes can be removed, leaving the semiconducting tubes in the device; this can be achieved by gate biasing all the semiconducting tubes off, and then making a large current flow through the remaining metallic CNTs, thus burning them out. However, the overall process leads to a reduction in the total yield. This is not so useful for large scale manufacturing. Devices made with SWCNTs might not, however, form a realistic basis for technology, due in part to their low current outputs and small active areas.

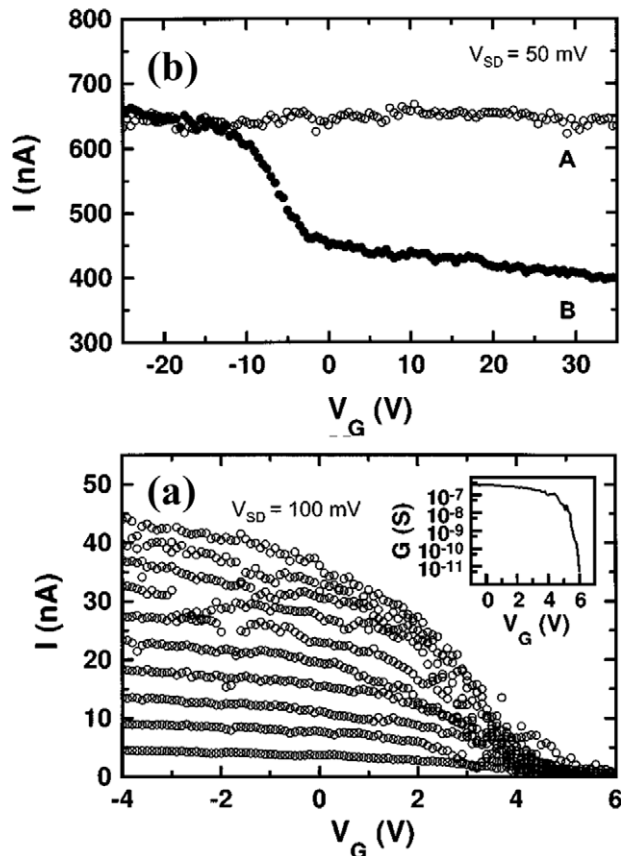


**Figure 27.** (a)  $I$ - $V_G$  curves for  $V_{\text{SD}} = 10$ – $100 \text{ mV}$  in steps of  $10 \text{ mV}$ . The inset shows that the gate modulates the conductance by five orders of magnitude ( $V_{\text{SD}} = 10 \text{ mV}$ ). (b)  $I$ - $V_G$  curve of a typical MWCNT device (curve (A)) in comparison to that of a collapsed tube of similar cross section (curve (B)). Reproduced with permission from [138]. Copyright 1998 American Institute of Physics.

Random deposition methods have been very effective for making first-generation devices since they are easily produced either by direct growth on a catalysed substrate or by deposition onto an arbitrary substrate from a solution of suspended CNTs. In this case the CNT density on the substrate must be high enough for the NTs to interconnect and form electrical paths [143]. CNT assembly is not easily reproducible, meaning that duplicating identical devices would be difficult and more complicated devices cannot be developed. For these reasons random deposition methods are clearly not immediately practical for large scale production devices.

A number of different techniques have been developed for controlling the position and orientation on the substrate and the number of nanotubes deposited [144, 145]. For example, application of an oriented electric field during the CVD process allows bridging of straight CNTs directly on metal electrodes, see figure 28 [144].  $I$ - $V$  curves obtained from these devices are also reported for metallic and semiconducting CNTs. This result clearly underlines the importance of applying a growth strategy highly compatible with standard semiconductor lithography processing techniques, in view of future large scale practical

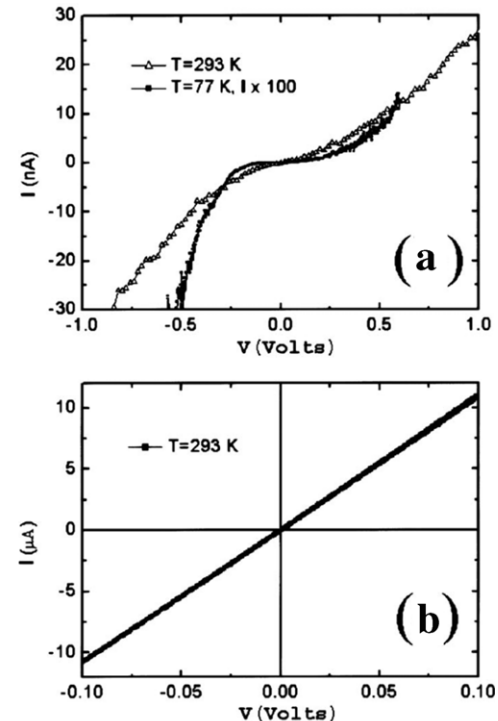
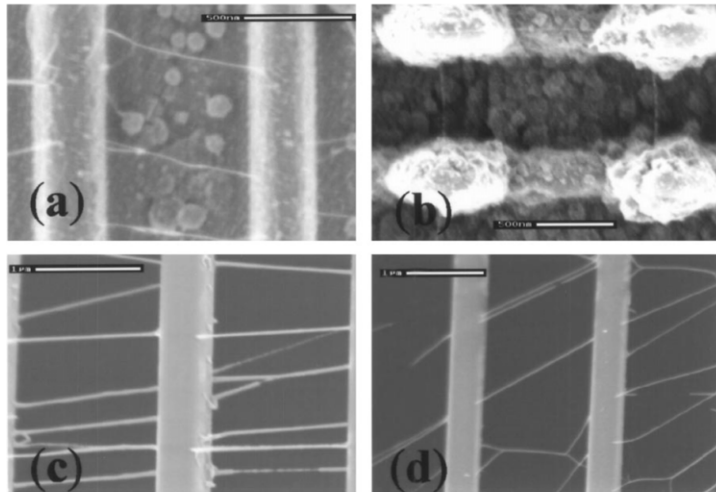


**Figure 28.** Left: (a)–(d) SEM images of SWCNTs connecting stripes or posts patterned on different substrates grown under applied electric field (scale bar:  $1 \mu\text{m}$ ). Right: (a)  $I$ – $V$  curves for a sample with suspended semiconducting SWCNTs at temperatures of  $T = 293 \text{ K}$  (triangles) and  $T = 77 \text{ K}$  (squares). The current ( $I$ ) values for  $T = 77 \text{ K}$  are multiplied by a factor of 100. (b)  $I$ – $V$  curve for a sample with metallic SWCNTs at room temperature (adapted with permission from [144]). Copyright 2003 American Institute of Physics.

applications which will most likely require integration of CNTs with silicon-based technology.

Recently, densely packed, perfectly aligned horizontal arrays of non-overlapping linear SWCNTs have been fabricated on a quartz substrate [145]. Large current outputs together with small variations in properties from device to device, even with tubes that individually have widely different transport characteristics, have been found. The highest value for the mobility in a p-type device developed on a plastic substrate is also reported as  $480 \text{ cm}^2 \text{ V}^{-1} \text{ s}^{-1}$ . This kind of device opens the way to future applications of CNT-FET flexible devices as also reported recently [146, 147].

## 7. Solar cells

In the last twenty years energy demand has increased remarkably and the scientific community has been asked to look for new energy resources. The progressive reduction of fossil fuel and the need for clean alternative energy resources to reduce the impact on the environment coming from fuel burning require a search for new alternative energy sources. In this scenario solar energy stands out as the most viable choice to meet the global energy demand. A solar cell is a device in which incident light is directly converted into electricity owing to the photovoltaic effect [148]. In the solar cell industry, semiconductor heterostructures containing p–n junctions are widely utilized to harvest light energy. In the photovoltaic device the semiconductor material has to be able to absorb most of the solar spectrum in a region

reasonably close to the surface and the photovoltage is developed across it. When photons are absorbed by the active material, their energy is used to excite electron–hole (e–h) pairs. The excited e–h pairs are collected at the junction in the presence of electric field (applied or already present at the interface). Subsequently, the high-energy electrons are selectively extracted at one terminal while the holes are replenished from the other terminal. Ideally, there should be a one-to-one relationship between light and electric current. The basic principles of a solar cell have been described in many publications [149, 150] and need not be detailed in this review. The main parameters that characterize the solar cell characteristics evaluated from the response of the cell under light irradiation are the open circuit voltage ( $V_{\text{oc}}$ ) and the short circuit current ( $I_{\text{sc}}$ ) as shown in figure 29(a). These are the maximum voltage and current the cell can develop respectively while the best power output response of the cell obtainable,  $P_{\text{m}}$  ( $P_{\text{m}} = I_{\text{m}}V_{\text{m}}$ ), can be estimated from the  $I$ – $V$  curves, see figure 29(a). The fill factor (FF) is the ratio of the maximum power ( $P_{\text{m}}$ ) divided by the  $V_{\text{oc}}$  and  $I_{\text{sc}}$ ,  $\text{FF} = P_{\text{m}} / (V_{\text{oc}}I_{\text{sc}})$ . In this framework the FF is a parameter often used to define the cell response. The energy conversion efficiency  $\eta$  is the percentage of incident light energy that actually ends up as electric power. This is calculated at the maximum power point,  $P_{\text{m}}$ , divided by the input light irradiance ( $E$ , in  $\text{W m}^{-2}$ ) under standard test conditions (STC) and the surface area of the solar cell ( $A_s$  in  $\text{m}^2$ ),  $\eta (\%) = P_{\text{m}} / (EA_s)$ . The STC specifies a temperature of  $25^\circ \text{C}$  and an irradiance of  $1000 \text{ W m}^{-2}$  with an air mass

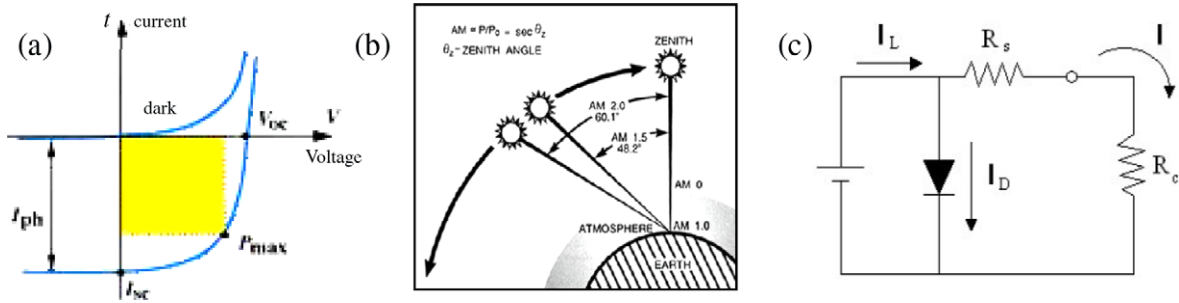


**Figure 29.** (a)  $I$ - $V$  curve for a photovoltaic device, (b) air mass (AM) definition, (c) equivalent circuit.

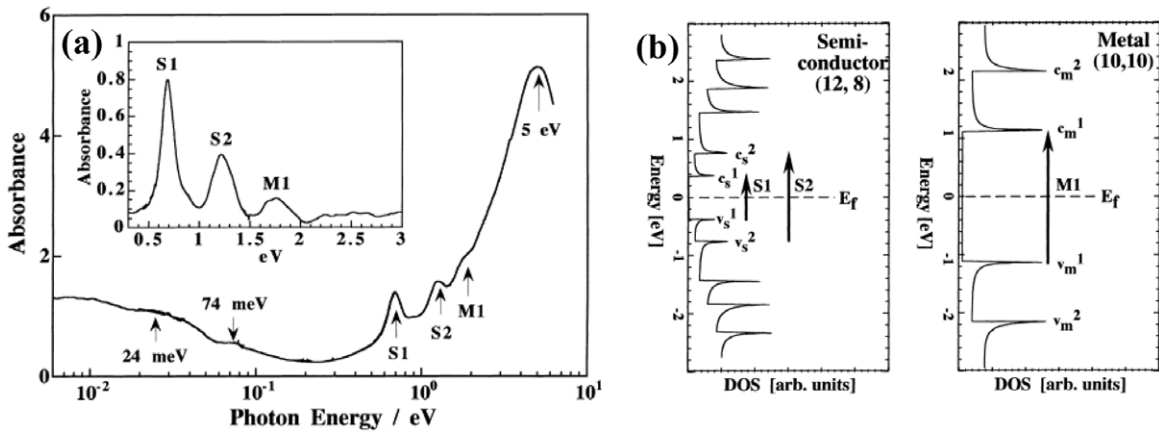


**Figure 30.** (a) Optical absorption spectrum of an SWCNT film in air at atmospheric pressure from UV to far IR. Inset: for convenience, by subtracting the large absorption background due to the p-plasmon, the absorption features labelled S1, S2, and M1 are clearly displayed. (b) Density of states (DOS) calculated from a tight-binding model for semiconducting (12, 8) and metallic (10, 10) SWCNTs. The absorption peaks (S1, S2, and M1) corresponding to the optical transitions between the van Hove singularities are indicated. Reproduced with permission from [30]. Copyright 2001 Elsevier.

1.5 (AM 1.5) spectrum and corresponds to the irradiance and spectrum of sunlight incident on a clear day upon a sun-facing  $37^\circ$ -tilted surface with the sun at an angle of  $41.81^\circ$  above the horizon, see figure 29(b). In the laboratory it is possible to have a solar spectrum simulator ( $1000\text{ W m}^{-2}$ ) or commercial lamps with different power outputs. The electric equivalent circuit of the photovoltaic cell is also reported in figure 29(c). Two resistances appear, one in series ( $R_s$ ) and one in parallel ( $R_p$ ). The series resistance is caused by the fact that a solar cell is not a perfect conductor. The parallel resistance originates from the leakage current from one terminal to the other due to poor insulation, for example at the cell edges. In an ideal solar cell, one would have  $R_s = 0$  and  $R_p = \infty$ .

Commercially available photovoltaic devices deliver power with 15% efficiency. Wafer-based silicon (single crystal and polycrystalline) solar cells and thin film solar cells based on amorphous silicon and III-V semiconductors dominate photovoltaic manufacture [149, 150], and they offer the best conversion efficiency attainable but are still expensive.

### 7.1. Carbon nanotube solar cells

In this research field, nanostructured materials have been recently identified as potential building blocks in new

generation solar cells. In principle, there are many advantages in using nanostructure-based devices such as reduced manufacturing cost, unlimited material availability, unlike silicon, and good quantum efficiency achievable by exploiting their low-dimensional optoelectronic properties that permit multiple electron-hole pair generation.

Carbon-based nanostructures have been extensively used in the assembly of solar cells [151]. Their potential applications in optoelectronics have been described in detail [152, 153] and it has been predicted that conversion rates of up to 10% can be reached with a marked dependence on the tube diameter. CNTs have a direct band gap which can vary from near zero in metallic tubes up to 0.5–0.6 eV in semiconducting CNTs; this value is inversely proportional to the tube diameter [26]. The typical absorbance spectrum obtained from an SWCNT is reported in figure 30 [30], where multiple bands can in principle participate in optical processes covering a wide energy range. Therefore, carbon nanostructure assemblies have been extensively studied for optoelectronic and energy conversion applications in the last decade.

A photovoltaic effect in a pristine nanotube diode device consisting of two CNTs with different electrical properties was first observed by Lee [154, 155]. The device consisted of an individual single semiconducting carbon tube

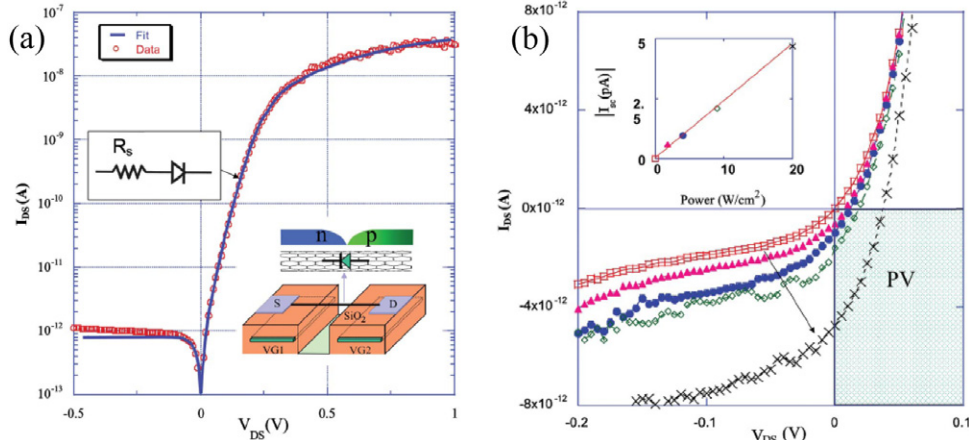


**Figure 31.** (a) Typical dark current–voltage  $I$ – $V$  curve at room temperature with a fit. The inset shows the split gate device where  $V_{G1}$  and  $V_{G2}$  are biased with opposite polarities ( $\pm 10$  V) to form an ideal p–n junction diode along an SWCNT. (b)  $I$ – $V$  characteristics under increased light intensity showing a progressive shift into the fourth quadrant (PV) where the diode generates power. The inset shows the expected linear increase in the current measured at  $V_{DS} = 0$  with illuminated power. Reproduced with permission from [154]. Copyright 2005 American Institute of Physics.

suspended between the source and drain gates, see the inset of figure 31(a). The electrostatic doping of the tube forms a p–n junction at room temperature. The  $I$ – $V$  curve in figure 31(a) shows that the CNT behaves like an ideal p–n junction diode and under light irradiation a photovoltaic effect is observed, see figure 31(b). This is also confirmed by the expected linear increase in the photocurrent measured at null applied voltage, see the inset of figure 31(b). Increasing the incident light power on the tube causes a progressive shift in the response towards the fourth (PV) quadrant [154].

Freitag *et al* [156] measured the infrared laser excited photoconductivity from an individual semiconducting carbon nanotube constituting the channel of a field effect transistor.

Figure 32(a) shows the drain current versus gate voltage characteristics of a typical ambipolar device (empty circles) and the characteristics for the same device irradiated with  $1 \text{ kW cm}^{-2}$  infrared light (full squares). Incident infrared light tuned between 1.59 and 1.27 eV was used to excite the  $E_{2-2}$  transition of the semiconducting nanotube, since the SWCNTs used in the experiments had diameters centred around 1.3 nm and  $E_{2-2}$  energy of about 1.35 eV. A drain voltage of 1 V was applied to reduce e–h recombination and facilitate charge collection. Whereas Schottky barriers limit carrier injection from the contacts into the channel, they allow the photogenerated charged carriers to leave the channel and be collected. The starting current value ('dark' with no light irradiation) increased by an order of magnitude upon irradiation and the gate voltage characteristics shifted by about 600 mV, effectively increasing the hole current and decreasing the electron current. Figures 32(b) and (c) show time-resolved traces of the photocurrent at  $-2$  V and  $+1.5$  V gate voltages. The mechanism of photocurrent generation involves resonant excitation of the second exciton state of the semiconducting nanotube ( $E_{2-2}$ ). This state decays to produce electron–hole pairs. The nanotube FET structure acts as a single-molecule photodetector.

Efficient multiple electron–hole pair generation in p–n junctions consisting of individual SWCNTs has been also

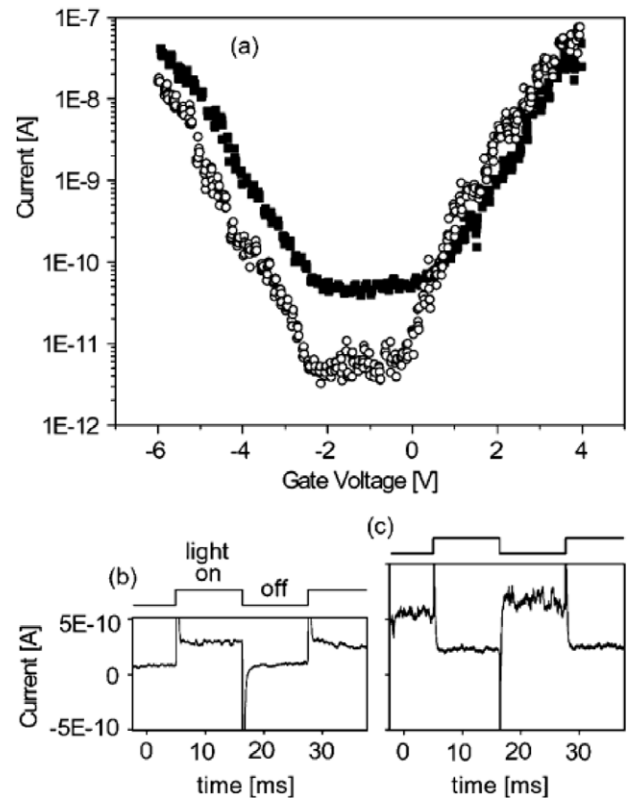


**Figure 32.** (a) Gating characteristics of an ambipolar NT-FET with (■) and without (○) infrared illumination ( $V_{\text{drain}} = -0.5$  V). (b), (c) Time traces of the current with the light chopped, taken at gate voltages of (b)  $-3$  V (hole conduction) and (c)  $+1.5$  V (electron conduction). The sign of the current spikes is independent of the gate voltage. The plateaus correspond to the data in (a). Reproduced with permission from [156]. Copyright 2003 American Chemical Society.

reported. In particular, an optical scanning microscope setup that combines electronic transport measurements at low temperature with spatially scanned laser illumination was used to measure the photocurrent response from an individual

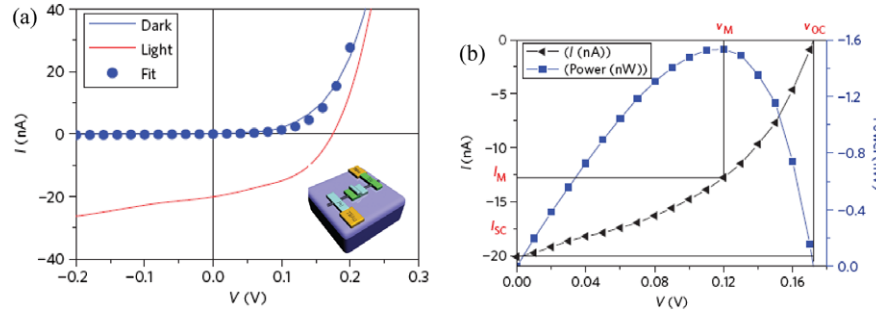


**Figure 33.** (a) Experimental and fitted  $I$ - $V$  characteristics in the dark (blue) and under illumination (red) measured for a device with light intensity of  $90 \text{ kW cm}^{-2}$ . Inset: schematic illustrating a CNT photovoltaic module with two cells connected in series. (b)  $I$ - $V$  (black) and output power (blue) characteristics for the same device. Reproduced with permission from [159]. Copyright 2011 Nature Publishing Group.

CNT [157]. Although the measurements were performed at low temperature the p-n junction CNT device still showed a significant power conversion efficiency at room temperature, considering that only a small fraction of the incident power is absorbed. Scanning photovoltage microscopy proves to be a useful probe technique for measuring the potential gradients in one-dimensional devices.

The standard limit of photovoltaic efficiency, first established by Shockley and Queisser [158], is set by the conversion of a single photon into a single e-h pair. In principle, it is now possible to employ an SWCNT to generate multiple e-h pairs from a single photon. In the absence of applied bias, only the internal fields can separate the photogenerated carriers and produce a photovoltage. These fields can be associated with the presence of Schottky barriers or at defects [152, 153].

Devices that use single SWCNTs as functional elements might not, however, form a realistic basis for technology, due to their low current outputs and small active areas. Nevertheless, it has been recently demonstrated that a single CNT diode can be realized in such a way that it can be replicated onto the supporting substrate and form a cascade solar cell [159]. Each device consisted of a semiconducting CNT deposited onto a  $\text{SiO}_2$  surface and connected to two scandium and palladium metal contacts. The remarkable difference in the metal work functions with respect to the tube band gap produced a local Schottky barrier that was not symmetric at the contacts. This contact is defined as virtual since its task is to produce a potential valley and hill to favour first the separation and then the collection of electron–hole pairs produced upon light irradiation and it is not connected to the external circuit. A metal contact made of Ti–Au helps the collection of the generated photocurrent. A single cell produces a  $V_{OC} = 0.23 \text{ V}$ ; the  $I_{SC}$  reaches  $20 \text{ nA}$ , indicating a high number of photogenerated charges, see figure 33. A double-cell module produces a  $V_{OC} = 0.41 \text{ V}$ , increasing up to  $0.84 \text{ V}$  in a quadrupole cell. Therefore the device seems to be merely a general tandem cell and may in principle be manufactured in the same way on a semiconducting CNT with varying diameter or energy bandgap, starting with smaller diameters and moving towards larger cells. The working principle for doubling the cell photovoltage in CNTs may readily be generalized to CNT photovoltaic modules with more cells to generate higher photovoltage.

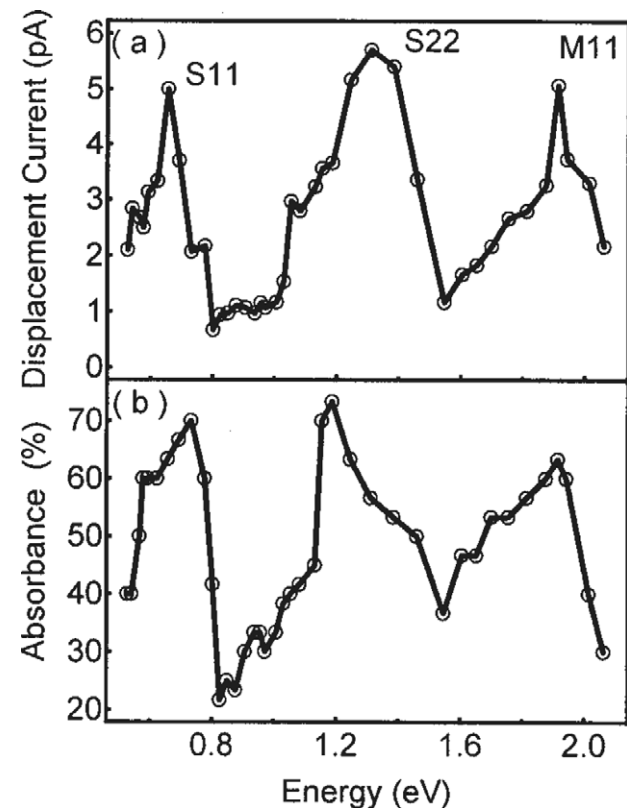


**Figure 34.** (a) The displacement photocurrent of an SWCNT film measured at  $300 \text{ K}$  as a function of incident photon energy. Peaks in the photocurrent are observed at the two lowest energy semiconductor transitions ( $S_{11}$  and  $S_{22}$ ) and at the lowest energy metallic transition ( $M_{11}$ ); (b) the absorbance spectrum measured for the same SWCNT film under the same conditions. Reproduced with permission from [160]. Copyright 2005 Applied Physics Letters.

In the case of SW and DWCNT films [42, 160–162] the photocurrent response was measured using a displacement photocurrent measurement technique. Briefly, the CNT film was deposited on a glass slide that was anchored to a grounded copper block within an optical access flow cryostat. The nanotubes were coupled to ground capacitively, through the glass dielectric, and coupled to the high side of the circuit by a wire silver-painted to a corner of the film. Pulsed laser light incident on the nanotube film excited charge carriers, which redistributed to create an ac voltage across the nanotube/insulator/metal capacitor. This was measurable as a

displacement current from the nanotube film to ground [42, 160]. The displacement current for the SWCNT film shows three peaks at 0.62, 1.39, and 1.85 eV, see figure 34. A comparison with the absorbance spectrum obtained on the same sample allows a close correspondence to be established between the peaks in the absorbance and those in the displacement current observed. In the case of DWCNT films the peaks found were assigned to the outer shell transitions that turned out to be the same as those found for the SWCNT film and to the inner shell transitions. There was a small shift in the outer shell transitions in the DW compared with the SW peaks that can be attributed to shell–shell interaction. The reported results are very interesting since they demonstrate that the metallic CNT can contribute to the photocurrent signal generation. In fact, for a bulk metal the e–h couple formed upon light irradiation would immediately recombine giving no photocurrent signal. The experimental results for CNTs demonstrate that an e–h pair is formed and it has a long enough lifetime to be separated and collected at the electrode. This effect has been also observed in MWCNT films that in principle should have a metallic behaviour [44, 161]. In particular, from the calculated density of states at the Fermi level for MWCNTs [44] the Thomas–Fermi static screening length ( $\lambda_{TF}$ ) has been evaluated. The  $\lambda_{TF}$  found ranges between 15 and 50 Å corresponding to a carrier density at the Fermi level of the order of  $9 \times 10^{20}$  electrons cm<sup>-3</sup>, significantly smaller than the usual carrier densities in bulk metals (about  $10^{22}$ – $10^{23}$  electrons cm<sup>-3</sup>). These findings imply that each e–h pair created within the nanotube is far less screened than in a typical metal, thus explaining why metallic nanotubes give a sizeable photocurrent signal.

CNT macro-bundles [162–164] consisting of many aligned nanotubes suspended between two electrodes have been irradiated with visible and infrared incident light and the photocurrent flow has been measured. The CNT bundles are connected to two annealed nickel foils to form metal–CNT heterojunctions. Several types of nanotube, SWCNTs, DWCNTs, and MWCNTs, with diameters of about 1.1, 2, and 50 nm, have been tested [162]. The results obtained show that each type of CNT has a distinct response upon light illumination, also in terms of the light spot position with respect to the metal contacts. The energy conversion efficiency observed in the nanotube bundles is remarkably low (<1%), thus suggesting that a better control of the bundles needs to be found.

An MWCNT–nSi diode prepared by a spray deposition technique gave a sizeable photoconductive response in the mid-IR energy range (8–12  $\mu\text{m}$ ) in nonbiased mode [165]. The current–voltage response obtained under low intensity IR light (15 mW cm<sup>-2</sup>) irradiation shows a photovoltaic response. To ascertain that the observed effect is due to the MWCNT film only a long pass germanium filter (LF) to cut photon energy higher than 0.6 eV (the cut-off wavelength is 2000 nm) in order to avoid any response from the Si band edge was used. It was possible to verify that the mid-IR band feature remained unchanged and that it was associated with the MWCNT–nSi interface only. In addition, the mid-IR band was not observed in the photocurrent spectrum

obtained from a control sample made of an SWCNT–nSi diode. The origin of the mid-IR photocurrent band can be associated with electron transition through the band gap of semiconducting MWCNTs with diameter in the range of 15–30 nm. The primary mechanism of photocurrent is photon absorption of the semiconducting MWCNT followed by charge separation at the interface, their transport and collection at the external electrodes. The tunable spectral response where the band gap depends on the nanotube diameter, high carrier mobility, simple wet deposition, and scalability makes such nanostructures very attractive for room temperature IR detection.

Solar cells based on CNTs/doped Si heterojunctions have been developed recently by taking advantage of the high mobility, conductive and transparent features of CNT film and the Si crystallinity that guarantees good length diffusion. The first solar cell studied consisted of an n-type crystalline silicon substrate on which a semitransparent thin film of DWCNT was deposited from solution [166]. The DW film made up of semiconducting and metallic tubes forms a high-density p–n heterojunction with the Si. The current–voltage characteristics show that the device behaves like a diode, with a power conversion efficiency of 7%. The observed energy conversion response is described as the result of multiple processes involving the DWCNTs. In fact, each CNT in the film forms a junction at the Si interface. This promotes charge separation where the electrons are moved to the n-type Si wafer and the holes are rapidly transported along the CNT percolation path to be collected at the contact electrode. A negligible degradation of current density after hundreds of hours of exposure to air is found. The role of a Si substrate that is not oxidized in the formation of more efficient heterojunctions with DWCNTs is also clearly evident, and is identified as the main factor influencing the relatively low efficiency found (<1%) in a similar experiment [167]. The above results suggest that CNT-on-Si is a potentially realizable configuration for photovoltaic devices, showing the possibility of producing solar cells with adequate conversion efficiencies while reducing the use of silicon.

Solar cells made of semiconducting SWCNTs with a narrow chirality distribution (7, 6 major chirality) [168] have been deposited on Si and on glass substrates (as reference) via spray coating from a suspension (0.5 mg ml<sup>-1</sup>) in dichlorobenzene solution. The photovoltaic properties of the solar cells were tested under dark and illuminated conditions under incident irradiation intensity of 100 mW cm<sup>-2</sup> (AM 1.5). Comparison of the photocurrent response obtained with the near infrared (NIR) absorption spectra (from the reference sample) clearly indicated an excellent matching of the S<sub>11</sub> band (corresponding to the first interband transition for SWCNTs with 7, 6 and 8, 6 chirality) with the photocurrent band located around 1150 nm. The result demonstrates that the SWCNT film contributes to the photoconversion process not only as a charge separator/transporter/collector but also as a light absorber. This is an important fact, distinguishing between a heterojunction solar cell with two active light absorbing components and a Schottky cell, where the metal component is not capable of absorbing photons. The best

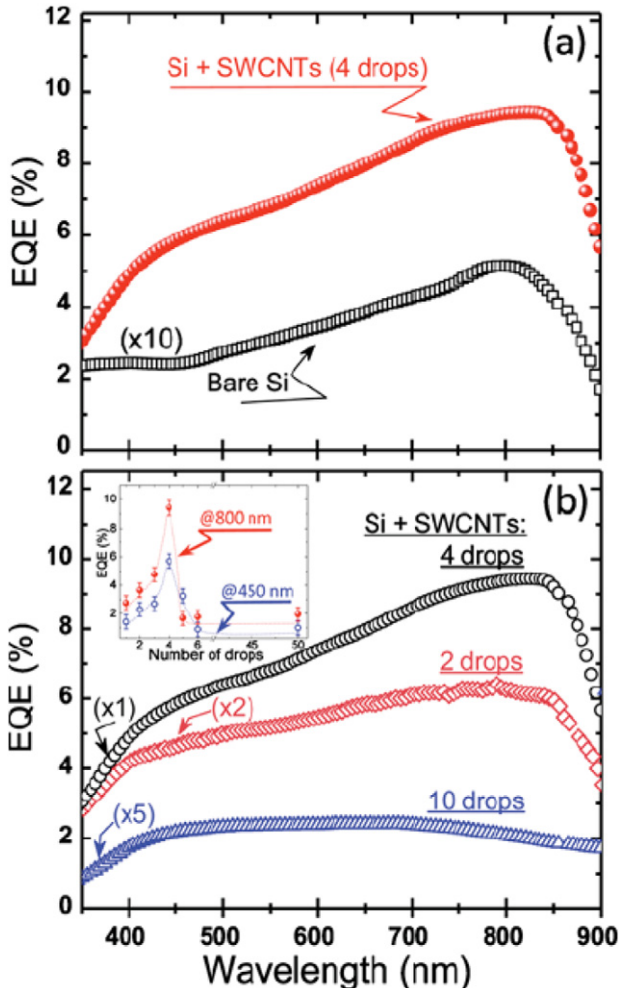


**Figure 35.** (a) Typical EQE spectra of our SWCNT/n-Si hybrid devices for four drops of SWCNTs and bare-Si. (b) Effect of the number of drops of SWCNTs on the EQE. The inset shows the EQE variation with the number of drops at  $\lambda = 450$  and  $800$  nm. Reproduced with permission from [169]. Copyright 2010 American Institute of Physics.

conversion efficiency cell found for the different cells studied was 1.7% [168].

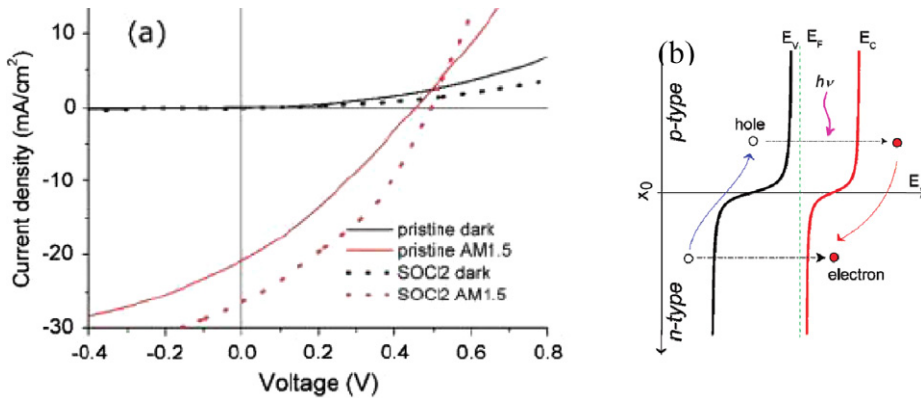
Laser synthesized SWCNTs drop cast onto n-Si have been used to realize relatively simple PV devices [169]. The SWCNTs were dispersed in methanol and drop cast on the substrate in controlled quantity (drops of solution). The photocurrent response was measured from metal contacts directly deposited onto the CNT film following a planar architecture, see figure 35.

Figure 35(a) shows that over all the spectral range studied, the external quantum efficiency (EQE) of the SWCNT/n-Si hybrid devices is enhanced compared to the bare-Si reference device. A maximum around 820 nm is found similar to that observed in [170] that is due to the Si substrate contribution. Samples that differ in the quantity of deposited SWCNTs have been investigated, see figure 35(b). A linear increase in the EQE with the quantity of SWCNTs deposited up to 10% (four drops of solution) was first found and then a reduction to 0.5% for 10 drops of solution deposited.

The result highlights the importance of the SWCNT-Si junctions for the generation of the photocurrent. Indeed, as the SWCNT film thickens, most of the impinging light is absorbed by the SWCNTs, and a large number of the charges generated in the SWCNT film recombine before reaching the depletion layer at the SWCNT/Si interface and ultimately the metal electrodes for collection. Thus, the optimal amount of SWCNTs found (4 drops) corresponds to a better ratio between the SWCNTs for light absorption and best harvesting of the photogenerated charges. The SWCNTs add an important sizeable contribution in the UV spectral range, where the Si has poor absorbance. This finding opens the prospect of photoconverting wavelengths shorter than the photoactive spectrum of traditional Si-solar cells [149, 150].

Improvement of solar cell photoconversion efficiency for SWCNT films has been reported recently [171]. Networks of SWCNTs deposited on n-Si substrates following an airbrush technique have been used for photovoltaic solar cells. The airbrushed SWCNT film is virtually free of catalyst residue or amorphous carbon particles. The semitransparent SWCNT network coating the n-Si substrate forms p-n and/or Schottky heterojunctions and exhibits a rectifying behaviour. Since the airbrush technique allows the deposition of CNT films of variable thickness an evaluation of the transmittance is performed. Several samples that differ in the transmittance are measured. The CNTs/n-Si form heterojunctions that upon illumination show a strong rectifying behaviour and photovoltaic effect. The generated electron–hole pairs are then separated and transported through SWCNTs (holes) and n-Si (electrons), respectively (figure 36). In the process the CNTs serve as both photogeneration sites and a charge carrier collecting and transport layer. In addition, after treating the SWCNT coating film with thionyl chloride ( $\text{SOCl}_2$ ) a significant increase in the conversion efficiency is found from 2.7% to 4%, see figure 36(a). The effect is interpreted as due to change in the energy levels involved in the heterojunction that increases the carrier concentration and mobility.

Studies on the possibility of modulating the Schottky junction formed between the SWCNT and the Si in a solar cell have been recently reported [172]. The photovoltaic cell used is shown in figure 37. The contact between the tubes and the Si forms a Schottky diode PV cell. Upon light irradiation the photons are transmitted through the transparent SWCNT film and interact with the Si and generate electron–hole pairs, that are driven in opposite directions by the field associated with the built-in potential in the depletion layer; in particular, holes are extracted on the SWCNT film side and electrons on the n-Si side. A power conversion efficiency (PCE) of 8.5% can be determined from the illuminated curve. This performance is better than that obtained from similar devices made with thin films of DWCNTs (7.4%) [166]. The natural porosity of the SWCNT film was exploited and an electrolyte gate was inserted to apply a gate field at the junction. The electrolyte substantially alters the  $J$ – $V$  characteristics as shown in figure 37. The solar cell characteristics extracted from the curves reported in figure 37 indicate that at the highest negative gate potential applied ( $-0.75$  V) the cell achieves a power conversion



**Figure 36.** (a) Photovoltaic performance (dark–light) of the pristine SWCNT/n-Si solar cell (black) and after the thionyl chloride (SOCl<sub>2</sub>) treatment (red). (b) Schematic energy band diagram of a heterojunction diode showing the photogenerated carrier transfer process. Reproduced with permission from [171]. Copyright 2009 American Chemical Society.

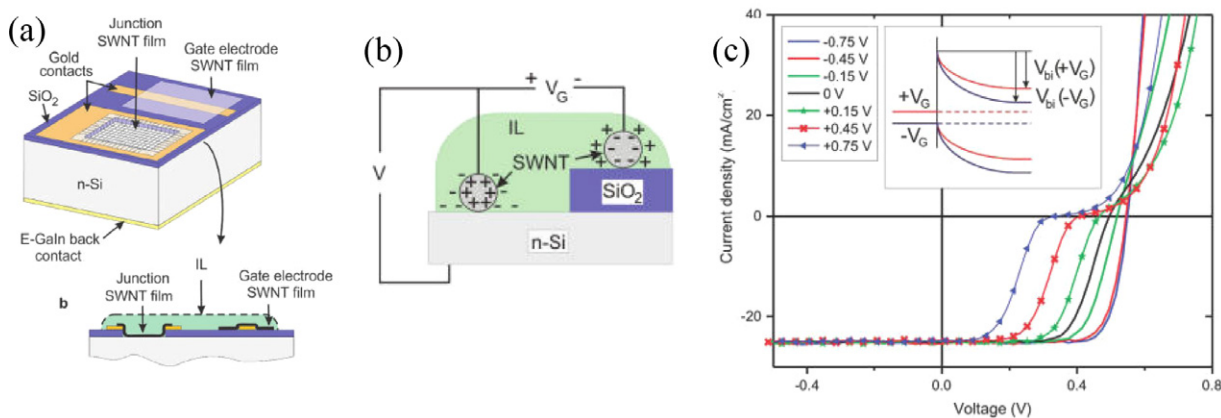


**Figure 37.** Device design. (a) Three-dimensional (3D) view (ionic liquid not shown). An SWCNT film contacts both the gold electrode and the n-Si within the window forming the SWCNT/n-Si junction (hash lines are merely aids for 3D visualization); a cross-sectional view with ionic liquid (IL) is shown. (b) Charge state of the junction SWCNTs with negative voltage applied to the gate electrode. (c) J–V plots of the illuminated SWCNT/n-Si cell under the indicated gate voltage applied to the gate electrode. Reproduced with permission from [172]. Copyright 2010 American Chemical Society.

efficiency of 11%, a value remarkably higher than its original value of 8.5%. Although a detailed modelling is needed to quantify the relative contributions of the identified effects involved in the process, the results obtained demonstrate that the ‘conventional’ CNT/n-Si junction coupled with an electrolyte gate allowed an active modulation of the power conversion efficiency to be obtained.

The integration of CNTs into Si-based photovoltaic devices is still evolving to improve the efficiency of solar cells. Very recently, it has been shown that the efficiency of a solar cell fabricated by coating an n-Si substrate with a porous CNT film increases from the initial value of 6.2% up to 11–13% [173] by acid-doping the nanotube network. The acid (dilute HNO<sub>3</sub>) significantly reduces the internal series resistance and favours the formation of photoelectrochemical units that enhance charge separation and transport. Given the high porosity of CNT films (>70%), the acid infiltration would simultaneously promote charge separation at the interface and provide additional charge transport paths through the CNT network. Time stability tests show that the performance degradation is within

10%. Compared to conventional Si cells, the fabrication process is greatly simplified, involving the transfer of a porous semiconductor-rich nanotube film onto an n-type crystalline Si wafer followed by acid infiltration. For practical applications, stability issues related to Si photocorrosion can be reduced by introducing an oxide layer on the surface. In addition, acid storage requires better device encapsulation and mild acid electrolytes.

Crystalline Si is very costly and needs to be doped in common photovoltaic devices; moreover, the wafer is usually very thick. Amorphous silicon (a-Si:H) can be used as an alternative material since it is much cheaper and can be employed in very thin layers. Nevertheless it needs to be covered with semitransparent electrodes (usually indium tin oxide, ITO, or ZnO) which are expensive and brittle. Networks of SWCNTs can replace these materials, acting mainly as a semitransparent electrode and to a lesser extent as a photoactive layer. Del Gobbo *et al* [174] realized an SWCNT/a-Si:H photovoltaic device, where the SWCNTs were deposited following an airbrush technique on the amorphous Si substrate, see figure 38. A thick film of Cr

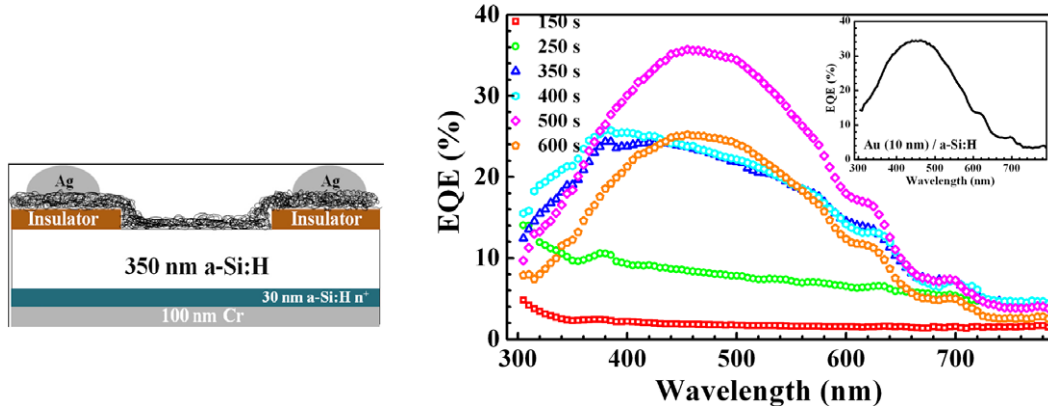


**Figure 38.** Left: a cross-sectional view of the device design. Right: external quantum efficiency (EQE) spectra of the device recorded as a function of the incident light wavelength for several SWCNT spraying times. Inset: EQE spectrum of a 10 nm Au film covering the same a-Si:H device. Reproduced with permission from [174]. Copyright 2011 American Institute of Physics.

was the back electrode contact. Samples that differed in the deposition time were prepared. The EQE for very small amount of SWCNTs, up to 250 s deposition time, corresponds to a very low CNT film thickness such that the number of SWCNT/a-Si:H heterojunctions formed is so small that the e–h pair generation, separation and transport is dominated by the CNTs alone. In fact, the EQE line shape closely resembles the SWCNTs' absorbance and no hint of the a-Si:H energy gap decrease can be detected. When the amount of SWCNT/a-Si:H heterojunctions increases, and more e–h pairs are generated in the a-Si:H substrate can be separated at the heterojunctions, the a-Si:H becomes more important. Indeed, the EQE spectral shape decreases at wavelength less than 350 nm due a-Si:H surface recombination, and increases at wavelengths greater than 720 nm. The corresponding value of the EQE strongly increases from 10% to 20%–25% at 400 nm. This suggests that current photogeneration is much more efficient in silicon than in SWCNTs. The EQE value increases to 35% at 460 nm, when the number of SWCNT/a-Si:H heterojunctions reaches its optimum value (500 s deposition time), and the spectral shape is very similar to that of the same a-Si:H cell covered by a 10 nm Au film (inset of figure 38). These results indicate that for such a high SWCNT/a-Si:H heterojunction density the SWCNT film acts mainly as a semitransparent conductive electrode rather than an e–h generator, thus confirming the Schottky barrier nature of the heterojunctions. This could be due to the wide spatial extension of the depletion region inside the a-Si:H substrate allowing a great number of e–h pairs coming from the silicon to be separated. Finally, the EQE behaviour for the spraying time of 600 s can be interpreted in terms of SWCNT partial optical absorption that prevents light from reaching the a-Si:H substrate underneath. Numerical simulations of the solar cell's response indicate that the poor quality of SWCNT contacts might be responsible for the reduced collection of the photogenerated holes and suggest that the contacts need to be improved for better efficiency. Nevertheless, SWCNT/a-Si:H-based devices are promising and deserve more research to increase their performance to a level that is competitive, in terms of cost, efficiency and flexibility.

Photovoltaic effects have been also measured for a network of MWCNTs [175], thus producing an optoelectronic solid state device sensitive to infrared, visible and near ultraviolet wavelength. Although the efficiency found was lower than that of a silicon solar cell, this result shows surprising potential given that the device used was built following a relatively easy method avoiding the use of the fundamental selective doping needed to obtain p–n junctions.

## 7.2. Photoelectrochemical devices

Several solar cells based on the new generation of materials have been developed, the most interesting being dye-sensitized solar cells (DSSCs) and organic solar cells. The DSSC is a special type of photoelectrochemical solar cell that was first developed by Grätzel in 1991 [176, 177]. It constitutes a valid alternative to the present p–n junction photovoltaic devices. In a common p–n junction the Si acts both as light absorber and separator of charges, while in the DSSC this task is shared between two basic elements. A dye sensitizer anchored to the surface of a wide band semiconductor absorbs the incident light; the charge separation occurs at the interface where the photogenerated electrons are injected from the dye to the conduction band of the solid semiconductor to the charge collector. An appropriate choice of the dye coupled with oxide films of nano-crystalline morphology makes it possible to expand the photon conversion process from the ultraviolet (UV) to the near infrared (IR) region. High conversion efficiencies have been obtained that enable the DSSC to compete with other new generation solar cells. In addition, DSSCs can be engineered into flexible sheets and are made of low cost material; solar modules have been on the market since 2009. DSSCs have some limitations, in that dyes suffer from degradation under heat and UV light, and the cell casing is difficult to seal due to the solvents used in assembly.

Following the basic idea of the Grätzel cell [176, 177], CNTs have been successfully incorporated into photoelectrochemical cells for application in solar cell devices but without the use of a dye-sensitized element. This is because CNT films are expected to form percolation paths,

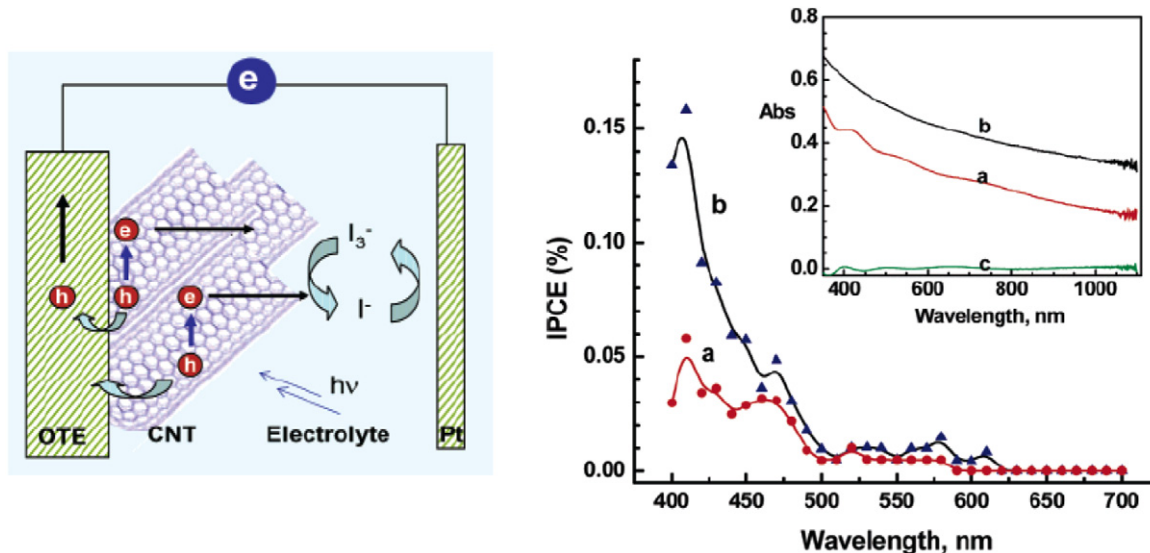


**Figure 39.** Left: photoelectrochemical cell scheme. Right: IPCE spectra of (a) OTE/SWCNT and (b) OTE/SnO<sub>2</sub>/SWCNT electrodes at different excitation wavelengths. The counter electrode is platinum gauze, and the electrolyte is 0.5 M LiI and 0.01 M I<sub>2</sub> in acetonitrile. Inset: absorption spectra of an SWCNT film cast by electrodeposition (50 Vdc) on an OTE electrode (curve (a)), OTE/SnO<sub>2</sub> electrodes (curve (b)), and the OTE reference electrode (curve (c)). Reproduced with permission from [178]. Copyright 2004 American Chemical Society.

exhibiting efficient charge separation and transport in the cells. Films of SWCNTs [178] were deposited onto two optically transparent electrodes made of indium tin oxide (ITO) and measured the optical response with a standard three-electrode system containing a redox couple I<sub>3</sub><sup>-</sup>/I<sup>-</sup> in acetonitrile, see figure 39. Two devices were measured: one was covered by the CNT film and the other was modified with SnO<sub>2</sub> nanoparticle colloids (ITO/SnO<sub>2</sub>) before CNT deposition. The overall system photoresponse is expressed in terms of incident photon to charge carrier conversion efficiency (IPCE) and is calculated by normalizing the photocurrent values for incident light energy and intensity as follows:

$$\text{IPCE} (\%) = 100 \times 1240 \text{ (nm)} I_{\text{sc}} \text{ (A cm}^{-2}\text{)} / (I_{\text{inc}} \text{ (W cm}^{-2}\text{)} \times \lambda \text{ (nm)})$$

where  $I_{\text{sc}}$  is the short circuit photocurrent (A cm<sup>-2</sup>),  $I_{\text{inc}}$  is the incident light intensity (W cm<sup>-2</sup>), and  $\lambda$  is the incident light wavelength (nm).

The measured IPCE value from the CNT only is around 0.05% at 400 nm. This value increases up to 0.15% for the modified ITO/SnO<sub>2</sub>. The photoirradiation induces the cathodic flow of electrons, indicating that the photogenerated holes are captured at the collecting electrode surface and transported to the counter electrode via an external circuit. The regenerative I<sub>3</sub><sup>-</sup>/I<sup>-</sup> redox couple facilitates the scavenging of electrons at the electrode surfaces and thus enables the delivery of a steady photocurrent. The cathodic character of the photocurrent further supports the notion that CNTs possess p-type semiconducting properties. The photocurrent response found has been interpreted in terms of electronic transitions involving van Hove singularities. The low value found was mainly explained in terms of a fast recombination of photogenerated charged species. These

features have been measured with optical and energy loss spectra between 1 and 3 eV [43, 179]. Although the IPCE values found are small compared to many nanostructured semiconductor films [180], the results reported prove that CNTs can be used to efficiently generate electron–hole pairs and have an optical response in the visible light energy range. The observed increase of the photocurrent signal for the ITO/SnO<sub>2</sub> electrode can be ascribed to different effects. One is that the SnO<sub>2</sub> nanoparticles increase the electrode surface area; another is that there is a direct interaction between the SnO<sub>2</sub> and the SWCNT that produces additional photogenerated charges at the electrode surface.

It is known that the SWCNTs tend to interact with each other by strong  $\pi$ – $\pi$  interaction; therefore they exist as ropes or bundles 10–25 nm in diameter and a few micrometres long. These ropes are entangled together in the solid state to form a highly dense, complex network structure. These factors make them very difficult to disperse in organic media. Since modern synthetic chemistry takes place in the solution phase a dissolution process for SWCNTs has been developed [181]. Since CNTs have a wide electrochemical stability, and high surface area accessible for selective functionalization different entities ranging from inorganic [182], to polymers [183] and biomolecules [184] have been interfaced with CNTs. These hybrid systems have emerged as a new class of nanomaterials with even more attractive properties and have been used for chemical [185] and bio-sensing [186], hydrogen storage [187], optical and electronic applications [188, 189], electrocatalysis, and others [190]. Only after SWCNTs have been solubilized can they be employed in photoelectrochemical devices and cells. This task can be carried out by covalently or non-covalently functionalizing them. Covalent functionalization can alter the pristine structural and electronic properties of the

tubes, while non-covalent functionalization cannot. Therefore non-covalent functionalization has been extensively applied for SWCNT-based devices [181]. Considerable effort has been made to modify the SWCNT surface to link molecules such as porphyrins [191, 192] to improve the photocurrent response. Supramolecular assemblies of protonated porphyrins and SWCNTs have reached a maximum IPCE value of 13% around 420 nm. Transient absorption measurements performed on the system indicate that the photocurrent generation can be ascribed to the photoinduced charge injection from the excited state of the porphyrin into the SWCNTs. The electrons are transported across the CNT film to the electrode, while the redox couple ( $I_3^-/I^-$ ) in the solution regenerates the molecules donating the missing electrons. The photocurrent generation is mainly attributed to the injection of charges coming from the porphyrin excited state into the SWCNTs, and the increase in the response is mainly due to the optical response of the molecule. The SWCNTs in this system play a double role: they promote charge transfer by interacting with excited porphyrin and act as conduits to transport the injected electrons to the collecting electrode. A similar role for the nanotube is also observed in architectures made up of SWCNTs decorated with semiconducting nanoparticles [193–196]. The basic idea consists of combining the quantum confinement effects of the semiconductor nanoparticles, such as  $TiO_2$ ,  $SnO_2$ ,  $CdSe$ , and  $CdS$ , with the ability of CNTs to act as conduits for the collection of photogenerated charges to the electrode surface. A remarkable increase in the IPCE up to 15% was found at around 350 nm photon wavelength in the case of SWCNT– $TiO_2$  hybrids [195], but only up to 0.5% for SWCNT– $CdS$  [196]. It turns out that similar SWCNT architectures provide a very limited gain in the IPCE response.

Although MWCNTs are expected to exhibit electronic properties similar to those of graphite, they have a photocurrent response while graphite does not. Photocurrent measurements from MWCNT film have been reported for the first time by Castrucci *et al* [197], see figure 40. The photoelectrochemical response is measured with a standard three-electrode cell, where the MWCNT film grown on  $SiO_2$  substrate is one electrode. The photoresponse obtained ranges from the visible to the near ultraviolet photon energy with a maximum in the IPCE of 7% at around 350 nm photon wavelength, a value 50 times higher than that reported for SWCNTs [178]. This result is absolutely outstanding and demonstrates that charge transfer and transport are more effective in MWCNTs. This is due to the presence of many cylindrical graphitic tubes that contribute to the current generation. Nevertheless, in the case of MWCNTs the assignment of the observed structures in the IPCE spectra is less clear.

In fact, no calculations of electronic DOSs for MWCNTs have been reported, to allow a direct correlation between the low dimensionality and the experimental photocurrent behaviour. Transmission electron energy loss spectra measurements performed on individual MWCNTs (inset of figure 40) show a well-defined feature at energies between 2.8 and 3.2 eV, in addition to the typical  $\pi$

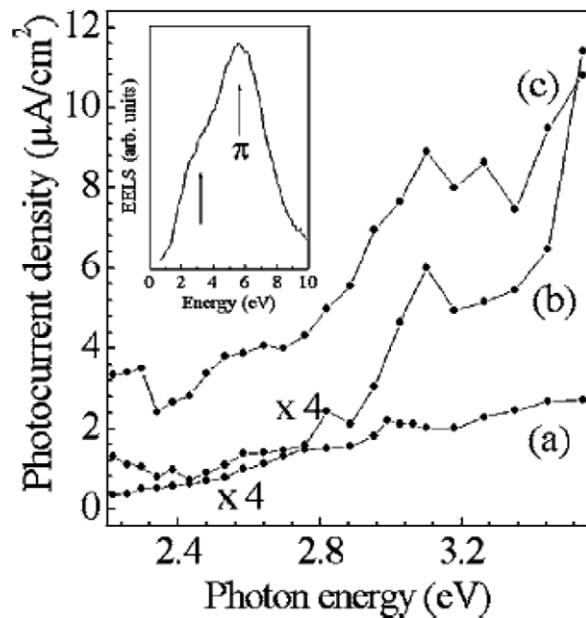


**Figure 40.** Photocurrent density spectra obtained for different MWCNT films. Inset: transmission electron energy loss spectrum recorded on an individual MWCNT of the sample of curve (c).  $NaI$  0.5 M and  $I_2$  0.01 M in acetonitrile is used as the electrolyte. Reproduce with permission from [197]. Copyright 2006 American Institute of Physics.

plasmon excitation peak located at around 6 eV [179]. These results have been confirmed by detailed electron energy loss calculations predicting the existence of the interband excitation channels in MWCNTs [31]. The experimental results indicate that the electronic density of states of MWCNTs is different from that of highly oriented pyrolytic graphite; this suggests the presence of singularities, due to reduced dimensionality. Theoretical [198] and experimental efforts [42, 160–162] have been mainly dedicated to double-walled carbon nanotubes (DWCNTs), these being the simplest MWCNTs. The MWCNT electronic density of states is difficult to model, due to the large number of shells and their mutual interactions; therefore, only a few theoretical predictions of MWCNT electronic properties are available [31]. Recently, additional theoretical results have been reported in the case of MWCNTs made up of four graphitic walls [44], as discussed previously and reported in figure 8. The calculated densities of states (DOSs) show that there is a rather small interaction among nanotubes. The van Hove singularities on both sides of the Fermi level ( $E_F$ ) together with the very small density of states at  $E_F$  might explain the origin of the photogenerated e–h pair in MWCNTs. In addition, the calculation shows that the density of states increases with the number of walls by up to a factor of five. This means that each multiwall contributes, in principle, to the photocurrent much more than a single wall does.

Recently, similarly to SWCNTs, MWCNTs have been used as building architectures for anchoring nanoparticles to improve the photocurrent response. Our group performed a detailed study of the effect on the photoelectrochemical response from MWCNT films decorated with Cu nanoparticles anchored on the CNTs simply by thermal deposition,

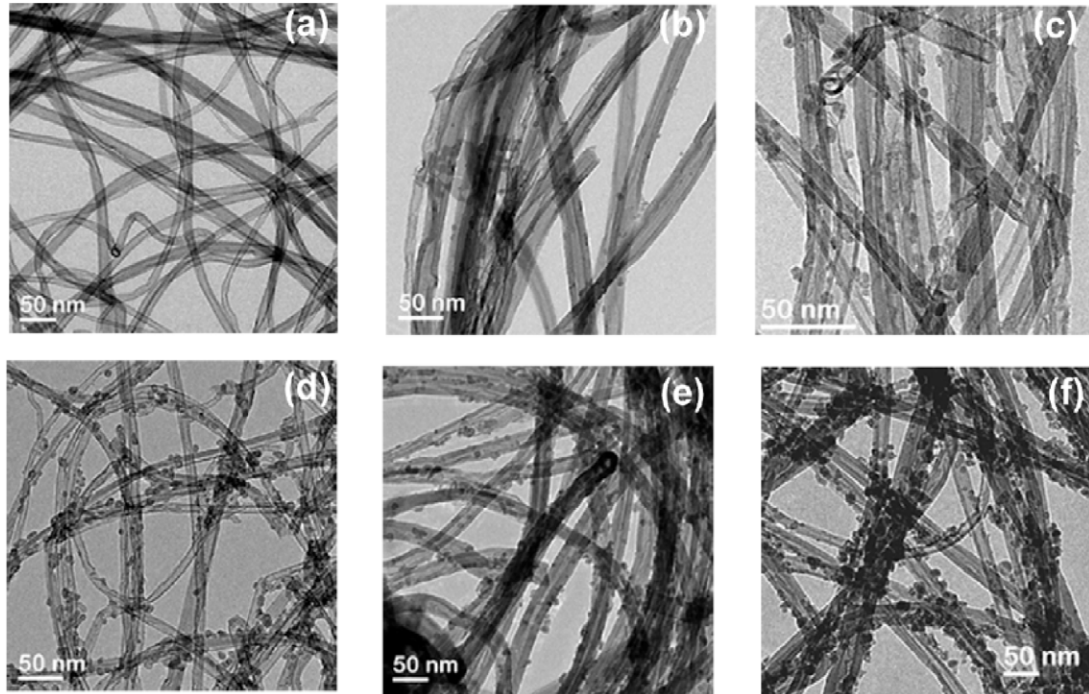


**Figure 41.** TEM images of a clean MWCNT sample (a) and Cu–MWCNT samples of (b) 0.1 nm, (c) 0.2 nm, (d) 0.5 nm, (e) 1 nm, and (f) 3 nm nominal Cu thickness [189].

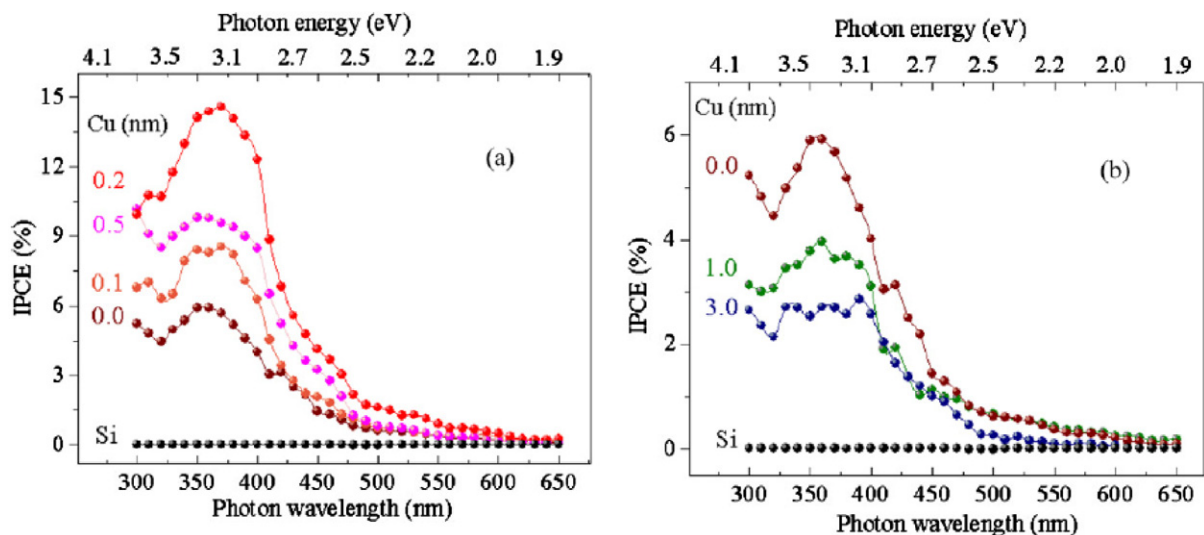


**Figure 42.** IPCE spectra collected as a function of the incident photon wavelength on Cu decorated MWCNT samples differing in the Cu nominal thickness (NT) deposited compared to the bare CNT (brown curve). In (a) the Cu NT varies from 0.1 to 0.5 nm and in (b) the Cu NT is 1 and 3 nm; the grey curve is the Si substrate signal and the brown curve is that from the bare CNT. The CE (counter electrode) is Pt; the electrolyte is KI 0.5 M and I<sub>2</sub> 0.01 M in acetonitrile; the applied cell potential is 12 mV [189].

see figure 41 [189, 199, 200]. A marked increase in the photoresponse in the visible and near ultraviolet photoenergy range was found with respect to the bare CNTs, see figure 42. The IPCE of about 5.9% obtained from bare CNTs, increased up to 14.6% around 360 nm photon wavelength for CNTs decorated with 0.2 nm of Cu (nominal thickness), see figure 42(a) [189]. Theoretical calculations performed on an SWCNT in close contact with a linear chain of Cu atoms [201] clearly indicate that there is an efficient charge transfer

between the Cu atoms in close contact with the C atom of the tube. The DOS of the hybrid architecture increases below and above the Fermi level. This means that more charges will be available in the contact region. The numerous concentric cylindrical walls of CNTs offer additional pathways for the flow and transport of photogenerated charges, finally collected at the electrode surface. In addition, inside the MWCNTs both semiconducting and metallic walls coexist, whereby localized Schottky barriers can form, thus favouring

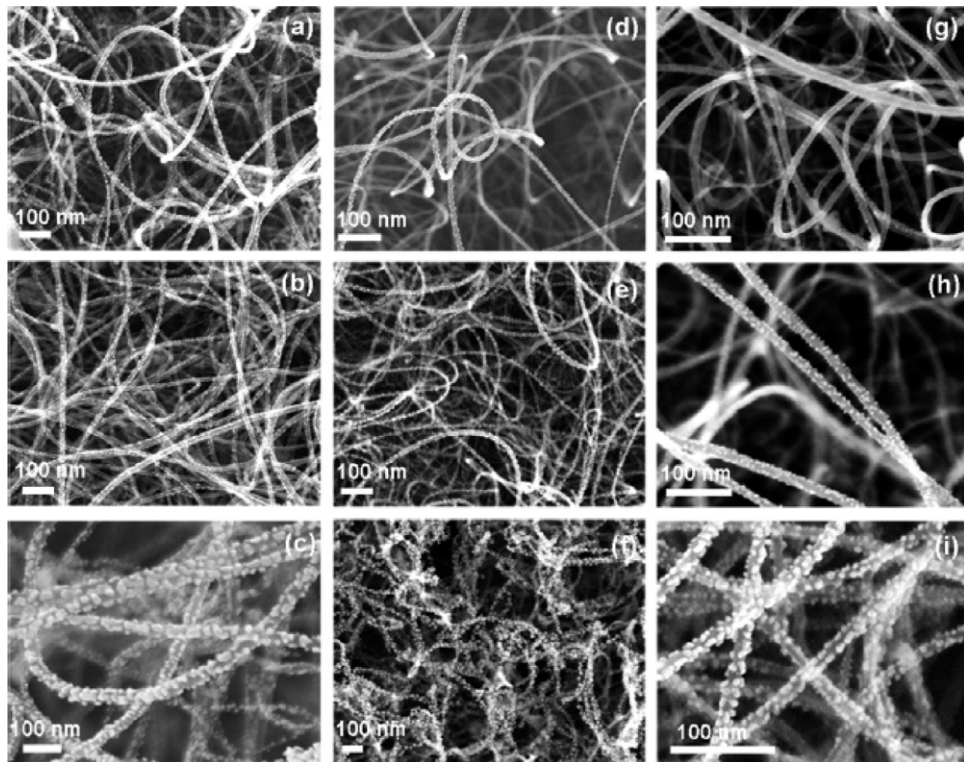


**Figure 43.** SEM images of Au–MWCNTs ((a)–(c)), Ag–MWCNTs ((d)–(f)), and Cu–MWCNTs ((g)–(i)), for 0.2 nm in (a), (d) and (g); 0.5 nm in (b), (e) and (h); and 3 nm in (c), (f) and (i), (nominal thicknesses) respectively. Reproduced with permission from [202]. Copyright 2012 Elsevier.

the diffusion of the optically excited charges and reducing their recombination. However, to maximize the effect of the metal particle–nanotube interface, the Cu clusters should be relatively small and dispersed. In fact, at higher coverage, the Cu nanoparticles increased in size and density and formed large clusters, a reduction in the photoresponse being observed, see figure 43(b). The increase in the mean dimension of Cu clusters has two main effects on the photocurrent generation: one is loss of contact with the tube outer wall and the second is a change in the electronic properties from semiconductive towards metallic. Both effects quench the photocurrent response. Similar results have been recently found also in the case of MWCNTs decorated with Au and Ag nanoparticles, see figure 43 [202, 203].

### 7.3. Polymer solar cells

Organic solar cells and polymer solar cells are built from thin films (typically 100 nm) of organic semiconductors including polymers and small-molecule compounds and carbon fullerenes and fullerene derivatives [204]. Although the energy conversion efficiencies achieved to date using conductive polymers are low (6%) compared to inorganic materials, these cells can be beneficial for applications where mechanical flexibility and disposability are important. Recently, photovoltaic devices based on CNTs and conjugated polymers, like P3OT poly(3-octylthiophene), have been extensively studied [205–207]. In this architecture the carbon nanotubes operate as a heterojunction component for charge

separation at high speed of the photogenerated excitons in the polymer, and offer a highly conductive percolated network for efficient charge transport to the collecting electrode. The dispersion of CNTs in a solution of an electron donating conjugated polymer is perhaps the most common strategy for inserting CNT-based materials for use in organic photovoltaic devices and thus raising the efficiency. Structural studies on regioregular poly(3-hexyl-thiophene) (rrP3HT) onto SW, DW and MWCNTs have been performed with STM, AFM and TEM [208–215]. Figure 44 [214] reports a collection of STM images obtained on a polymer–MWCNT coiled structure. The polymer presents a high degree of order as the periodic wrapping can be observed as a replicating assembly over the whole structure. The period of the polymer structure evaluated is  $3.0 \pm 0.1$  nm. The P3HT self-organization is helical but in this case, remarkably, the coiling shows a variable coiling angle. As can be seen in the inset of figure 44(b) where the structure has been mathematically reconstructed, the periodic variation of the coiling angle eliminates the rotational symmetry of the covering structure. Nevertheless, the inter-coil distance along the nanotube main axis does not vary as can be observed in the other examples of figure 44. From the images collected different patterns of the polymer coverage have been found, since the P3HT structure rotates around along the nanotube, as shown in figures 44(c) and (d).

Figure 44(e) shows the local density of states (LDOS) of a P3HT coil-wrapped (15, 0) SWCNT nanotube evaluated from the measured STS spectra reported in [211, 212]. The experimental curve, collected on a bare SWCNT, is compared with the DOS of a theoretical curve [216]. From the DOS

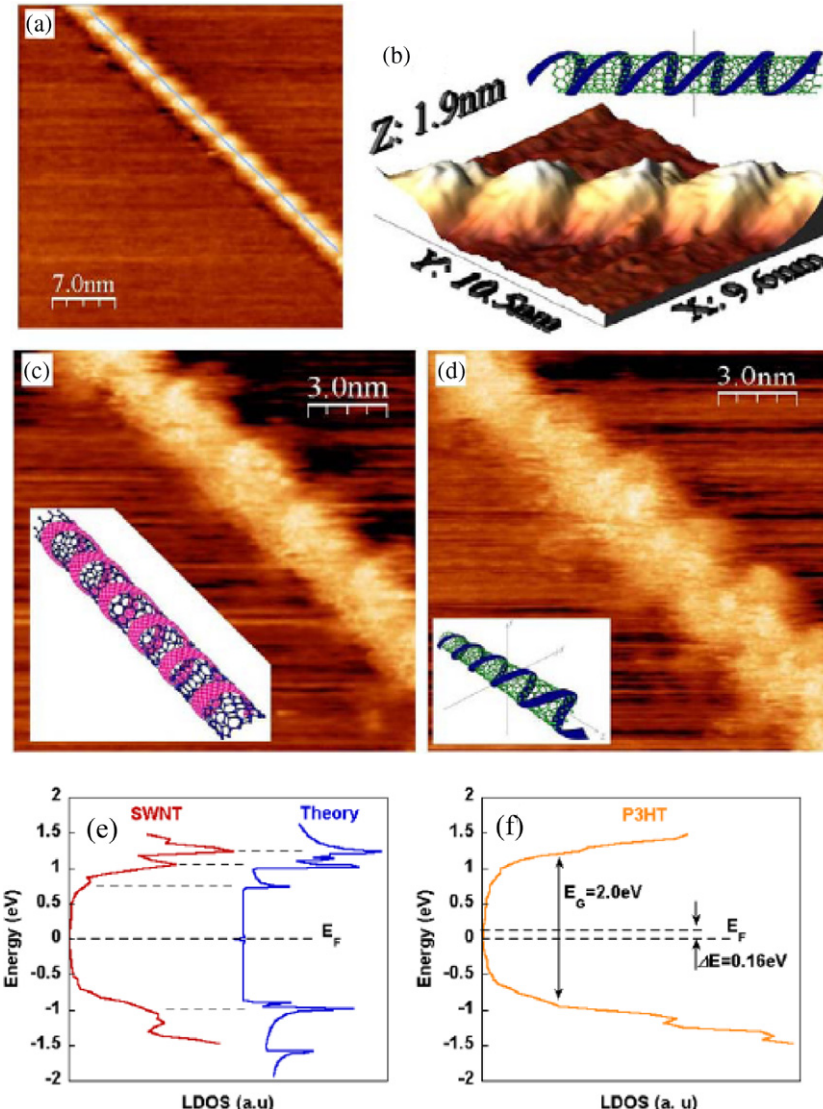


**Figure 44.** (a) A polymer covered CNT imaged by UHV-STM. The line of the structure is used for profile analysis. (b) 3D image and (c) corresponding 2D image. The image has been filtered with a Gaussian smooth on the  $Y$  axis. Inset: the polymer wrapping generated mathematically. (d) The same wrapped nanotube pictured in a different point of the structure ( $V_{\text{SAMPLE}} = -0.5\text{ V}$  and  $I = 0.3\text{ nA}$ ). (e) STS of the bare nanotube section. The agreement between the experimental result and the theoretical curve is evident and confirmed by the coincidence of the Van Hove singularities. (f) The differential conductance related to the local density of states (LDOS) of the P3HT covered part of the CNT. The shift of the energy gap towards the highest occupied molecular orbital (HOMO) is due to a charge transfer from the polymer to the nanotube. Reproduced with permission from [214].

measured on a P3HT wrapped section of the same nanotube, as reported in figure 44(f), it is possible to observe that an energy shift ( $\Delta E = 0.16\text{ eV}$ ) of the polymer band gap towards the highest occupied molecular orbital (HOMO) appears in the differential conductance curve. The shift can be related to negative charge transfer from the P3HT to the nanotube that can be therefore be referred to as a donor–acceptor system. Electron transfer to a nanotube can cause a further shift of the Fermi energy of the nanotube towards the vacuum level. It has also been identified as one of the factors reducing the possibility of charge separation in P3HT/CNT-based devices [217].

For devices made with SWCNT–poly(3-octylthiophene) (P3OT) an increase in the photoresponse ( $\sim 500$  times) as compared to the pristine P3OT is found and can be

attributed partly to the increase in effective hole mobility, due to the reduction of localized states of the pristine P3OT matrix, and partly to the enhanced exciton extraction at the polymer/nanotube junctions [205–220]. However, SWCNTs increase the efficiency of P3OT solar cells unlike the case of P3HT. Despite intensive efforts in involving carbon nanotubes as active components in polymer-based solar cells the current efficiencies for such hybrid cells are still modest. Besides, the cells have a limited environmental stability since they suffer from degradation in air even at room temperature, although nanotubes are stable at much higher temperatures. In the polymer/CNT films metallic and semiconducting nanotubes coexist, and tend to aggregate at higher concentrations, causing phase segregation between the nanotubes and the polymer. For the successful future development of this

research area, however, it is important to obtain uniformity of the samples. Comparative studies on individual nanotubes before and after functionalization are necessary, in order to determine the dependence of the reactivity on the electronic structure and the effect of chemical modification on the electrical properties [218–220]. Furthermore, the nanotubes are able to deliver dissociated charge carriers to the electrode at high speed and their concentration in the composite should be high enough to reach percolation. Polymers on the other hand, have poor mobility and could severely limit the charge transport to the opposite electrode. These are the major challenges to be overcome to substantially improve the cell efficiencies.

## 8. Conclusions and future prospects

The theoretical and experimental studies performed since CNTs were first synthesized have proved, among other things, their extraordinary electronic and optical properties. CNTs are a model system for the study of a variety of phenomena at the nanometre scale and for the development of basic concepts applicable in many different devices. Certainly, in the future more information on the physics of nanoscale systems will come from the study of CNTs. Independently of the outcome of the ongoing race to exploit nanotubes in applications, carbon nanotubes have provided previously unconceivable possibilities in nanotechnology. The research into CNTs and more recently into graphene is providing new insights into how to handle and process nanomaterials and develop nanotechnology.

The results reported in this review describe the more relevant electronic and optical CNT applications in photon energy conversion devices. Some CNT applications are produced on an industrial scale, such as x-ray tubes [221], scanning x-ray sources [222], flat panel displays [223] and lamps [224]. Others still require a more sophisticated CNT preparation, like field effect transistors or logic circuits made with single CNTs, as illustrated in this review. Nevertheless, CNTs are one of the most perfect one-dimensional physical objects and provide an interesting and ideal system for understanding fundamental physical properties of objects down the nanometre scale. In this regard, Luttinger liquid behaviour and ballistic transport at room temperature have been studied in many experiments. In terms of the properties reported in these pages, CNTs are capable of absorbing sunlight and generating electrons efficiently. This important capability has been exploited so as to produce different light conversion devices where CNTs have been inserted as active electrodes or simply to help charge carrier separation and transport. Various methods have been employed in solar cell realization; these include individual CNTs, metallic and semiconducting SWCNTs and MWCNT films deposited on different substrates, CNT–polymer assemblies, and, more recently, Si–CNT heterojunctions. The CNT-based solar cells tested to date are still far lower in efficiency than silicon-based ones. The limited cell performance results from the coexistence of different types of CNT that causes a facile deactivation in the excited states, SWCNTs'

tendency to aggregate that promotes self-quenching, and the contamination from impurities including metal catalyst particles and amorphous carbon. The major bottleneck in the development of nanotube-based devices is the inability to produce large amounts of identical and pure tubes of the same size and structure. Although there is no reliable way to produce a single type of CNT as required, it is now possible to separate a single type of nanotube from a mixture. Recent advances in depositing ultra-thin and homogeneous CNT films on arbitrary substrates can reduce the process cost and improve the films' mechanical flexibility. The studies performed hitherto indicate that CNTs are insensitive to temperature change. This means, in practice, that raising the temperature has no effect on the power conversion efficiency (in the range from 20 to 60 °C), in contrast to conventional Si cells that undergo a 20% reduction over the same temperature range. Pure, highly chemically and environmentally stable CNT cells are expected to eventually appear on the market. When this happens they should turn out to be more economical than silicon-based solar cells. Other applications with real potential include optical devices such as electrically pumped solid state nanoscale light sources and lasers, CNT light guides and nonlinear devices.

## References

- [1] Kroto H W, Heath J R, O'Brien S C, Curl R F and Smalley R E 1985 *Nature* **318** 162
- [2] Oberlin A, Endo M and Koyama T 1976 *J. Cryst. Growth* **32** 335
- [3] Iijima S 1991 *Nature* **354** 56
- [4] Iijima S, Ichihashi T and Ando Y 1992 *Nature* **356** 776
- [5] Iijima S and Ichihashi T 1993 *Nature* **363** 603
- [6] Nobel prize lectures of Geim A K and Novoselov K S 2010 [www.nobelprize.org](http://www.nobelprize.org)
- [7] Novoselov K S, Geim A K, Morozov S V, Jiang D, Zhang Y, Dubonos S V, Grigorieva I V and Firsov A A 2004 *Science* **306** 666
- [8] Castro Neto A H, Guinea F, Peres N M R, Novoselov K S and Geim A K 2009 *Rev. Mod. Phys.* **81** 110
- [9] Dresselhaus M S, Dresselhaus G, Sugihara K, Spain I L and Goldberg H A 1988 *Graphite Fibers and Filaments* (*Springer Ser. Mater. Sci.*) vol 5 (Berlin: Springer)
- [10] Saito R, Fujita M, Dresselhaus G and Dresselhaus M S 1992 *Appl. Phys. Lett.* **60** 2204
- [11] Hamada N, Sawada S and Oshiyama A 1992 *Phys. Rev. Lett.* **68** 1579
- [12] Odom T W, Huang J L, Kim P and Lieber C M 1998 *Nature* **391** 62
- [13] Kim P, Odom T W, Huang J-L and Lieber C M 1999 *Phys. Rev. Lett.* **82** 1225
- [14] Venema L C, Janssen J W, Buitelaar M R, Wildöer J W G, Lemay S G, Kouwenhoven L P and Dekker C 2000 *Phys. Rev. B* **62** 5238
- [15] Ebbesen T W and Ajayan P M 1992 *Nature* **358** 220
- [16] Salvetat J P, Bonard J M, Thomson N H, Kulik A J, Forrò L, Benoit W and Zuppiroli L 1999 *Appl. Phys. A* **69** 255
- [17] Tombler T, Zhou C, Alexeyev L, Kong J, Dai H, Liu L, Jayanthi C, Tang M and Wu S 2000 *Nature* **405** 769
- [18] Liu L, Jayanthi C S, Tang M, Wu S Y, Tombler T W, Zhou C, Alexeyev L, Kong J and Dai H 2000 *Phys. Rev. Lett.* **84** 4950

- [19] Jorio A, Dresselhaus M S and Dresselhaus G 2008 *Carbon Nanotubes: Advanced Topics in the Synthesis, Structure, Properties, and Applications* (New York: Springer)
- [20] Saito R, Fujita M, Dresselhaus G and Dresselhaus M S 1992 *Appl. Phys. Lett.* **60** 2204
- [21] Charlier J-C, Blase X and Roche S 2007 *Rev. Mod. Phys.* **79** 677
- [22] Kim P, Odom T W, Huang J-L and Lieber C M 1999 *Phys. Rev. Lett.* **82** 1225
- [23] Widoer J W G, Venema L C, Rinzler A G, Smalley R E and Dekker C 1998 *Nature* **391** 59
- [24] Venema L C, Wildöer J W G, Temminck Tunistra H L J, Kouwenhoven L P and Dekker C 1999 *Science* **283** 52
- [25] Lemay S G, Janssen J W, van den Hout M, Mooij M, Bronikowski M J, Willis P A, Smalley R E, Kouwenhoven L P and Dekker C 2001 *Nature* **412** 617
- [26] Kataura H, Kumazawa Y, Maniwa Y, Umezawa I, Suzuki S, Ohtsuka Y and Achiba Y 1999 *Synth. Met.* **103** 2555
- [27] Rubio A, Sánchez-Portal D, Artacho E, Ordejón P and Soler J M 1999 *Phys. Rev. Lett.* **82** 3520
- [28] Odom T W, Hafner J H and Lieber C M 2001 *Top. Appl. Phys.* **80** 173
- [29] Chen J, Hamon M A, Hu H, Chen Y, Rao A M, Eklund P C and Haddon R C 1998 *Science* **282** 95
- [30] Minami N, Kazaoui S, Jacquemin R, Yamawaki H, Aoki K, Kataura H and Achiba Y 2001 *Synth. Met.* **116** 405
- [31] Liu X, Pichler T, Knupfer M, Golden M S, Fink J, Kataura H and Achiba Y 2002 *Phys. Rev. B* **66** 045411
- [32] Rao A M et al 1997 *Science* **275** 187
- [33] Kuzmany H, Plank W, Hulman M, Kramberger Ch, Grüneis A, Pichler Th, Peterlik H, Kataura H and Achiba Y 2001 *Eur. Phys. J. B* **22** 307
- [34] Dresselhaus M S, Dresselhaus G, Jorio A, Souza Filho A G, Pimenta M A and Saito R 2002 *Acc. Chem. Res.* **35** 1070
- [35] O'Connell M et al 2002 *Science* **297** 593
- [36] Bachilo S M, Strano M S, Kittrell C, Hauge R H, Smalley R E and Weisman R B 2002 *Science* **298** 2361
- [37] Ho Y H, Chang C P, Shyu F L, Chen R B, Chen S C and Lin M F 2004 *Carbon* **42** 3159
- [38] Kwon Y and Tomanek D 1998 *Phys. Rev. B* **58** R16001
- [39] Okada S and Oshiyama A 2003 *Phys. Rev. Lett.* **91** 216801
- [40] Saito R, Dresselhaus G and Dresselhaus M S 1993 *J. Appl. Phys.* **73** 494
- [41] Ho Y H, Ho G W, Wu S J and Lin M F 2006 *J. Vac. Sci. Technol. B* **24** 1098
- [42] Mohite A, Sumanasekera G U, Hirahara K, Bandow S, Iijima S and Alphenaar B W 2005 *Chem. Phys. Lett.* **412** 190
- [43] Shyu F L and Lin M F 2000 *Phys. Rev. B* **62** 8508
- [44] Castrucci P, Scilletta C, Del Gobbo S, Scarselli M, Camilli L, Simeoni M, Delley B, Continenza A and De Crescenzi M 2011 *Nanotechnology* **22** 115701
- [45] Bethune D S, Kiang C H, de Vries M S, Gorman G, Savoy R, Vazquez J and Beyers R 1993 *Nature* **363** 605
- [46] Journet C, Maser W K, Bernier P, Loiseau A, Delachapelle M L, Lefrant S, Deniard P, Lee R and Fischer J E 1997 *Nature* **388** 756–8
- [47] Thess A et al 1996 *Science* **273** 483–7
- [48] Liu H, Nishide D, Tanaka T and Kataura H 2011 *Nature Commun.* **2** 309
- [49] Ghosh S, Bachilo S M and Weisman R B 2010 *Nature Nanotechnol.* **5** 443
- [50] Ando Y, Zhao X, Sugai T and Kumar M 2004 *Mater. Today* **7** 22
- [51] Hong G, Chen Y, Li P and Zhang J 2012 *Carbon* **50** 2067
- [52] Futaba D N, Goto J, Yasuda S, Yamada T, Yumura M and Hata K 2009 *Adv. Mater.* **21** 4811
- [53] Yuan D N, Ding L, Chu H B, Feng Y Y, McNicholas T P and Liu J 2008 *Nano Lett.* **8** 2576
- [54] Raty J Y, Gygi F and Galli G 2005 *Phys. Rev. Lett.* **95** 096103
- [55] Fan S, Michael G, Chaplin M G, Nathan R, Franklin N R, Tombler T W, Cassell A M and Dai H 1999 *Science* **283** 512
- [56] Dai H, Kong J, Zhou C, Franklin N, Tombler T, Cassell A, Fan S and Chapline M 1999 *J. Phys. Chem. B* **103** 11246
- [57] Wang X, Li Q, Xie J, Jin Z, Wang J, Li Y, Jiang K and Fan S 2009 *Nano Lett.* **9** 3137
- [58] Ren Z F, Huang Z P, Xu J W, Wang J H, Bush P, Siegal M P and Provencio P N 1998 *Science* **282** 1105
- [59] Zhang M, Fang S, Zakhidov A A, Lee S B, Aliev A E, Willimas C D, Atkison K R and Baughman R H 2005 *Science* **309** 1215
- [60] Cao Q, Kim H-S, Pimparkar N, Kulkarni J P, Wang C, Shim M, Roy K, Alam M A and Rogers J A 2008 *Nature* **454** 495
- [61] Camilli L, Scarselli M, Del Gobbo S, Castrucci P, Nanni F, Gautron E, Lefrant S and De Crescenzi M 2011 *Carbon* **49** 3307
- [62] Monthioux M, Smith B W, Burteaux B, Claye A, Fischer J E and Luzzi D E 2001 *Carbon* **39** 1251
- [63] El-Barbary A A, Telling R H, Ewels C P, Heggie M I and Briddon P R 2003 *Phys. Rev. B* **68** 144107
- [64] Stone A J and Wales D J 1986 *Chem. Phys. Lett.* **128** 501
- [65] Jensen P, Gale J and Blasé X 2002 *Phys. Rev. B* **66** 193403
- [66] Orlikowski D, Buongiorno Nardelli M, Bernholc J and Roland C 2000 *Phys. Rev. B* **61** 14194
- [67] Dunlap B I 1994 *Phys. Rev. B* **49** 5643
- [68] Hashimoto A, Suenaga K, Gloter A, Uruta K and Iijima S 2004 *Nature* **430** 870
- [69] Fan Y, Goldsmith B R and Collins P G 2005 *Nature Mater.* **4** 906
- [70] Yao Z, Postma H W Ch, Bents L and Dekker C 1999 *Nature* **402** 273
- [71] Ouyang M, Huang J-L, Cheung C I and Lieber C M 2001 *Science* **291** 97
- [72] Bittencourt C, Felten A, Douhard B, Colomer J-F, Van Tendeloo G, Drube W, Ghijsen J and Pireaux J-J 2007 *Surf. Sci.* **601** 2800
- [73] Charlier J-C et al 2009 *Nanotechnology* **20** 375501
- [74] Terrones M, Banhart F, Grobert N, Charlier J-C, Terrones H and Ajayan P M 2002 *Phys. Rev. Lett.* **89** 075505
- [75] Jorio A, Souza Filho A G, Saito R, Dresselhaus G and Dresselhaus M S 2003 *New J. Phys.* **5** 139.1
- [76] Scarselli M 2011 unpublished data
- [77] Qin C and Peng L-M 2002 *Phys. Rev. B* **65** 155431
- [78] Qin L C, Ichihashi T and Iijima S 1997 *Ultramicroscopy* **67** 181
- [79] Goldberg D, Bando Y, Burgeois L and Kurashima K 1999 *Carbon* **37** 1858
- [80] Hashimoto A, Suenaga K, Gloter A, Uruta K and Iijima S 2004 *Nature* **430** 870
- [81] Warner J H, Young N P, Kirkland A I and Briggs G A D 2011 *Nature Mater.* **10** 958
- [82] Helveg S, López-Cartes C, Sehested J, Hansen P L, Clausen B S, Rostrup-Nielsen J R, Abild-Pedersen F and Nørskov J K 2004 *Nature* **427** 426
- [83] Lin M, Tan J P Y, Boothroyd C, Loh K P, Tok E S and Foo Y-L 2007 *Nano Lett.* **7** 2234
- [84] Zhang X B, Zhang X F, Amelinckx S, Van Tendeloo G and Van Landuyt J 1994 *Ultramicroscopy* **54** 237
- [85] Cowley J M and Sundell F A 1997 *Ultramicroscopy* **68** 1
- [86] Humphreys C J 1989 *Ultramicroscopy* **28** 357
- [87] Banhart F 2006 *J. Mater. Sci.* **41** 4505

- [88] Castrucci P, Scarselli M, De Crescenzi M, El Khakani M A and Rosei F 2010 *Nanoscale* **2** 1611
- [89] Nygård J, Cobden D H, Bockrath M, McEuen P L and Lindelof P E 1999 *Appl. Phys. A* **69** 297
- [90] Bockrath M, Cobden D H, Lu J, Rinzler A G, Smalley R E, Balents L and McEuen P L 1999 *Nature* **397** 598
- [91] Avouris P, Chen Z and Perebeinos V 2007 *Nature Nanotechnol.* **2** 605
- [92] Landauer R 1970 *Phil. Mag.* **21** 863
- [93] Büttiker M 1986 *Phys. Rev. Lett.* **57** 1761
- [94] Büttiker M and Christen T 1996 *Quantum Transport in Semiconductor Submicron Structures* ed B Kramer (Dordrecht: Kluwer)
- [95] Tans S J, Devoret M H, Dai H, Thess A, Smalley R E, Geerlings L J and Dekker C 1997 *Nature* **386** 474
- [96] Bockrath M, Cobden D H, McEuen P L, Chopra N G, Zettl A, Thess A and Smalley R E 1997 *Science* **275** 1922
- [97] Langer L, Stockman L, Heremans J P, Bayot V, Olk C H, Van Haesendonck C, Bruynseraeede Y and Issi J-P 1994 *J. Mater. Res.* **9** 927
- [98] Terrones M et al 1998 *Appl. Phys. A* **66** 307
- [99] Dai H, Wong E W and Lieber C M 1996 *Science* **272** 523
- [100] Langer L, Bayot V, Grivei E, Issi J-P, Heremans J P, Olk C H, Stockman L, Van Haesendonck C and Bruynseraeede Y 1996 *Phys. Rev. Lett.* **76** 479
- [101] Ebbesen T W, Lezec H, Hiura H, Bennett J W, Ghaemi H F and Thio T 1996 *Nature* **382** 54
- [102] Kasumov A Yu, Khodos I I, Ajayan P M and Colliex C 1996 *Europhys. Lett.* **34** 429
- [103] Bachtold A, Fuhrer M S, Plyasunov S, Forero M, Anderson E H, Zettl A and McEuen P L 2000 *Phys. Rev. Lett.* **84** 6082
- [104] Frank S, Poncharal P, Wang Z L and de Heer W A 1998 *Science* **280** 1744
- [105] Urbina A, Echeverría T, Pérez-Garrido A, Díaz-Sánchez A and Abellán J 2003 *Phys. Rev. Lett.* **90** 106603
- [106] Park J-Y, Rosenblatt S, Yaish Y, Sazonova V, Uestuenel H, Braig S, Arias T A, Brouwer P W and McEuen P L 2004 *Nano Lett.* **4** 517
- [107] Gomez-Navarro C, De Pablo P J, Gomez-Herrero J, Biel B, Garcia-Vidal F J, Rubio A and Flores F 2005 *Nature Mater.* **4** 534
- [108] Javey A, Guo J, Paulsson M, Wang Q, Mann D, Lundstrom M and Dai H 2004 *Phys. Rev. Lett.* **92** 106804
- [109] Sze M 1981 *Physics of Semiconductor Devices* (New York: Wiley)
- [110] Duerkop T, Getty S A, Cobas E and Fuhrer M S 2004 *Nano Lett.* **4** 35
- [111] Svensson J and Campbell E B 2011 *J. Appl. Phys.* **110** 111101
- [112] Tombler T W, Zhou C, Kong J and Dai H 2000 *Appl. Phys. Lett.* **76** 2412
- [113] Yaish Y, Park J-Y, Rosenblatt S, Sazonova V, Brink M and McEuen P L 2004 *Phys. Rev. Lett.* **92** 046401
- [114] Javey A, Guo J, Wang Q, Lundstrom M and Dai H 2003 *Nature* **424** 654
- [115] Appenzeller J, Radosavljević M, Knoch J and Avouris P 2004 *Phys. Rev. Lett.* **92** 048301
- [116] Topinka M A, Rowell M W, Goldhaber-Gordon D, McGehee M D, Hecht D S and Gruner G 2009 *Nano Lett.* **9** 1866
- [117] Hu L, Hecht D S and Grüner G 2004 *Nano Lett.* **4** 2513
- [118] Cao Q, Kim H S, Pimparkar N, Kulkarni J P, Wang C J, Shim M, Roy K, Alam M A and Rogers J A 2008 *Nature* **454** 495
- [119] Zhou Y, Gaur A, Hur S H, Kocabas C, Meitl M A, Shim M and Rogers J A 2004 *Nano Lett.* **4** 2031
- [120] Collins P C, Arnold M S and Avouris P 2001 *Science* **292** 706
- [121] Arnold M S, Green A A, Hulvat J F, Stupp S I and Hersam M C 2006 *Nature Nanotechnol.* **1** 60
- [122] Zhang G, Qi P, Wang X, Lu Y, Li X, Tu R, Bangsaruntip S, Mann D, Zhang L and Dai H 2006 *Science* **314** 974
- [123] Liu K, Avouris P, Martel R and Hsu W K 2001 *Phys. Rev. B* **63** 161404
- [124] Carroll D L, Blase X, Charlier J-C, Curran S, Redlich P, Ajayan P M, Roth S and Rühle M 1998 *Phys. Rev. Lett.* **81** 2332
- [125] Bockrath M, Hone J, Zettl A, McEuen P L, Rinzler A and Smalley R 2000 *Phys. Rev. B* **61** R10606
- [126] Zhou C, Kong J, Yenilmez E and Dai H 2000 *Science* **290** 1552
- [127] Kong J, Zhou C, Yenilmez E and Dai H 2000 *Appl. Phys. Lett.* **77** 3977
- [128] Miyata Y, Maniwa Y and Kataura H 2006 *J. Phys. Chem. B* **110** 25
- [129] Lee J U, Gipp P P and Heller C M 2004 *Appl. Phys. Lett.* **85** 145
- [130] Yao Z, Postma H W C, Balents L and Dekker C 1999 *Nature* **402** 273
- [131] Giusca C E, Tison Y and Silva S R P 2007 *Phys. Rev. B* **76** 035429
- [132] Freitag M, Tsang J C, Bol A, Avouris P, Yuan D and Liu J 2007 *Appl. Phys. Lett.* **91** 031101
- [133] Collins P G, Bando H and Zettl A 1998 *Nanotechnology* **9** 153
- [134] Castrucci P, Scarselli M, De Crescenzi M, El Khakani M A, Rosei F, Braidy N and Yi J-H 2004 *Appl. Phys. Lett.* **85** 3857
- [135] Chico L, Crespi V H, Benedict L X, Louie S G and Cohen M L 1996 *Phys. Rev. Lett.* **76** 971
- [136] Bockrath M, Liang W, Bozovic D, Hafner J H, Lieber C M, Tinkham M and Park H 2001 *Science* **291** 283
- [137] Avouris P, Freitag M and Perebeinos V 2008 *Nature Photon.* **2** 341 and references therein
- [138] Martel R, Schmidt T, Shea H R, Hertel T and Avouris P 1998 *Appl. Phys. Lett.* **73** 2447
- [139] Giusca C E, Tison Y and Silva S R P 2007 *Phys. Rev. B* **76** 035429
- [140] Hu J, Ouyang M, Yang P and Lieber C M 1999 *Nature* **399** 48
- [141] Kawano T, Christensen D, Chen S, Cho C Y and Lin L 2006 *Appl. Phys. Lett.* **89** 163510
- [142] Tans S, Verschueren A and Dekker C 1998 *Nature* **393** 49
- [143] Snow E S, Novak J P, Campbell P M and Park D 2003 *Appl. Phys. Lett.* **82** 2145
- [144] Peng H B, Ristropf T G, Schurmann G M, King G M, Yoon J, Narayananurmi V and Golovchenko J A 2003 *Appl. Phys. Lett.* **83** 4238
- [145] Kang S J, Kocabas C, Ozel T, Shim M and Pimparkar N 2007 *Nature Nanotechnol.* **2** 230
- [146] Cao Q, Kim H-S, Pimparkar N, Kulkarni J P, Wang C, Shim M, Roy K, Alam M A and Rogers J A 2008 *Nature* **454** 495
- [147] Fanchini G, Unalan H E and Chhowalla M 2006 *Appl. Phys. Lett.* **88** 191919
- [148] Becquerel A E 1839 *C. R. Acad. Sci.* **9** 561
- [149] Goetzberger A, Knobloch J and Voss B 1998 *Crystalline Silicon Solar Cells* (New York: Wiley)
- [150] Green M A 1995 *Silicon Solar Cells: Advanced Principles and Practice* (Sidney: Bridge Printery)
- [151] Zhu H 2009 *Sol. Energy Mater. Sol. Cells* **93** 1461
- [152] Stewart D A and Leonard F 2005 *Nano Lett.* **5** 219
- [153] Stewart D A and Leonard F 2004 *Phys. Rev. Lett.* **93** 107401
- [154] Lee J U 2005 *Appl. Phys. Lett.* **87** 073101
- [155] Lee J U, Codella P J and Pietrzykowski M 2007 *Appl. Phys. Lett.* **90** 053103
- [156] Freitag M, Martin Y, Misewich J A, Martel R and Avouris P 2003 *Nano Lett.* **3** 1067

- [157] Gabor N M, Zhong Z, Bosnick K, Park J and McEuen P L 2009 *Science* **325** 1367
- [158] Shockley W and Queisser H J 1961 *J. Appl. Phys.* **32** 510
- [159] Yang L, Wang S, Zeng Q, Zhanog Z, Pei T, Li Y and Peng L-M 2011 *Nature Photon.* **5** 672
- [160] Mohite A, Chakraborty S, Gopinath P, Sumanasekera G U and Alphenaar B W 2005 *Appl. Phys. Lett.* **86** 061114
- [161] Sarker B K, Arif M, Stokes P and Khondakera S I 2009 *J. Appl. Phys.* **106** 074307
- [162] Wei J Q, Sun J L, Zhu J L, Wang K L, Wang Z C, Luo J B, Wu D H and Cao A Y 2006 *Small* **2** 988
- [163] Sun J L, Wei J Q, Zhu J L and Wu D H 2006 *Appl. Phys. Lett.* **88** 131107
- [164] Itkis M E, Borodnits F, Yu A and Haddon R C 2006 *Science* **312** 413
- [165] Ong P-L, Euler W B and Levitsky I A 2010 *Appl. Phys. Lett.* **96** 033106
- [166] Jia Y *et al* 2008 *Adv. Mater.* **20** 4594
- [167] Wei J *et al* 2007 *Nano Lett.* **7** 2317
- [168] Ong P-L, Euler W B and Levitsky I A 2010 *Nanotechnology* **21** 105203
- [169] Le Borgne V, Castrucci P, Del Gobbo S, Scarselli M, De Crescenzi M, Mohamedi M and El Khakani M A 2010 *Appl. Phys. Lett.* **97** 193105
- [170] Jia Y *et al* 2008 *Adv. Mater.* **20** 4594
- [171] Li Z, Kunets V P, Saini V, Xu Y, Dervishi E, Salamo G J, Biris A R and Biris A S 2009 *ACS Nano* **3** 1407
- [172] Wadhwa P, Liu B, McCarthy M A, Wu Z and Rinzler A G 2010 *Nano Lett.* **10** 5001
- [173] Jia Y *et al* 2011 *Nano Lett.* **11** 1901
- [174] Del Gobbo S, Castrucci P, Scarselli M, Camilli L, De Crescenzi M, Mariucci L, Valletta A, Minotti A and Fortunato G 2011 *Appl. Phys. Lett.* **98** 183113
- [175] Passacantando M *et al* 2008 *Appl. Phys. Lett.* **93** 051911
- [176] Grätzel M 2001 *Nature* **414** 338
- [177] O'Regan B and Graetzel M 1991 *Nature* **353** 737
- [178] Barazzouk S, Hotchandani S, Vinodgopal K and Kamat P V 2004 *J. Phys. Chem. B* **108** 17015
- [179] Stéphan D, Taverna M, Kociak K, Suenaga L, Henrard C and Colliex 2002 *Phys. Rev. B* **66** 155422
- [180] Scarselli M, Masala S, Castrucci P, De Crescenzi M, Gatto E, Venanzi M, Karmous A, Szkutnik P D, Ronda A and Berbezier I 2007 *Appl. Phys. Lett.* **91** 141117
- [181] Umeyama T and Imahori H 2008 *Energy Environ. Sci.* **1** 120
- [182] Georgakilas V, Gournis D, Tzitzios V, Pasquato L, Guldi D M and Prato M 2007 *J. Mater. Chem.* **17** 2679
- [183] Liu P 2005 *Eur. Polym. J.* **41** 2693
- [184] Sanchez-Pomales G, Santiago-Rodríguez L and Cabrera C R 2009 *J. Nanosci. Nanotechnol.* **9** 2175
- [185] Kong J, Franklin N R, Zhou C, Chapline M G, Peng S, Cho K and Dai H 2000 *Science* **287** 622
- [186] Oh J, Yoo S, Chang Y W, Lim K and Yoo K H 2009 *Curr. Appl. Phys.* **9** 229
- [187] Shiraiishi M, Takenobu T, Yamada A, Ata M and Kataura H 2002 *Chem. Phys. Lett.* **358** 213
- [188] Du J, Fu L, Liu Z, Han B, Li Z, Liu Y, Sun Z and Zhu D 2005 *J. Phys. Chem. B* **109** 12772
- [189] Scarselli M, Castrucci P, Camilli L, Del Gobbo S, Casciardi S, Tombolini F, Gatto E, Venanzi M and De Crescenzi M 2011 *Nanotechnology* **22** 035701
- [190] Wildgoose G G, Banks C E and Compton R G 2006 *Small* **2** 182
- [191] Hasobe T, Fukuzumi S and Kamat P V 2005 *J. Am. Chem. Soc.* **127** 11884
- [192] Hasobe T, Fukuzumi S and Kamat P V 2006 *J. Phys. Chem. B* **110** 25477
- [193] Kamat P V 2006 *Nanotoday* **1** 20
- [194] Vietmeyer F, Seger B and Kamat P 2007 *Adv. Mater.* **19** 2935
- [195] Kongkanand A, Martínez Domínguez R and Kamat P V 2007 *Nano Lett.* **7** 676
- [196] Robel I, Bunker B A and Kamat P V 2005 *Adv. Mater.* **17** 2458–63
- [197] Castrucci P, Tombolini F, Scarselli M, Speiser E, Del Gobbo S, Richter W, De Crescenzi M, Diociaiuti M, Gatto E and Venanzi M 2006 *Appl. Phys. Lett.* **89** 253107
- [198] Kwon Y K and Tomanek D 1998 *Phys. Rev. B* **58** R16001
- [199] Scarselli M *et al* 2009 *J. Phys. Chem. C* **113** 5860
- [200] Scarselli M, Scilletta C, Tombolini F, Castrucci P, De Crescenzi M, Diociaiuti M, Casciardi S, Gatto E and Venanzi M 2009 *Superlattices Microstruct.* **46** 340
- [201] Kong K, Han S and Ihm J 1999 *Phys. Rev. B* **60** 6074
- [202] Scarselli M, Camilli L, Castrucci P, Nanni F, Del Gobbo S, Gautron E, Lefrant S and De Crescenzi M 2012 *Carbon* **50** 875
- [203] Scarselli M, Camilli L, Persichetti L, Castrucci P, Lefrant S, Gautron E and De Crescenzi M 2012 *Carbon* **50** 3616
- [204] Forrest S R and Thompson M E 2007 *Chem. Rev.* **107** 923
- [205] Kymakis E and Amaralunga G A J 2002 *Appl. Phys. Lett.* **80** 112
- [206] Kymakis E, Servati' P, Tzanetakis P, Koudoumas E, Korniliou N, Rompogiannakis I, Frangiadakis Y and Amaralunga G A J 2007 *Nanotechnology* **18** 435702
- [207] Kymakis E, Koudoumas E, Frangiadakis I and Amaralunga G A J 2006 *J. Phys. D: Appl. Phys.* **39** 1058
- [208] Geng J and Zeng T 2006 *J. Am. Chem. Soc.* **128** 16827
- [209] Liu P 2005 *Eur. Polym. J.* **41** 2693
- [210] Stranks S D, Weissfennig C, Parkinson P, Johnston M B, Herz L M and Nicholas R J 2011 *Nano Lett.* **11** 66
- [211] Giulianini M, Waclawik E R, Bell J M, Scarselli M, Castrucci P, De Crescenzi M and Motta N 2009 *Appl. Phys. Lett.* **95** 143116
- [212] Giulianini M, Waclawik E R, Bell J M, De Crescenzi M, Castrucci P, Scarselli M and Motta N 2009 *Appl. Phys. Lett.* **95** 013304
- [213] Giulianini M, Waclawik E R, Bell J M, Scarselli M, Castrucci P, De Crescenzi M and Motta N 2009 *Appl. Phys. Lett.* **95** 143116
- [214] Giulianini M, Waclawik E R, Bell J M, Scarselli M, Castrucci P, De Crescenzi M and Motta N 2011 *Polymers* **3** 1433
- [215] Giulianini M, Waclawik E R, Bell J M, De Crescenzi M, Castrucci P, Scarselli M, Diociaiuti M, Casciardi S and Motta N 2011 *J. Phys. Chem. C* **115** 6324
- [216] Akai Y and Saito S 2005 *Physica E* **29** 555
- [217] Kanai Y and Grossman J C 2008 *Nano Lett.* **8** 908
- [218] Mallajosyula A T, Iyer S S K and Mazhari B 2010 *J. Appl. Phys.* **108** 094902
- [219] Pradhan B, Batabyal S K and Pal A J 2006 *Appl. Phys. Lett.* **88** 093106
- [220] Landi B J, Raffaelle R P, Castro S L and Bailey S G 2005 *Prog. Photovolt. Res. Appl.* **13** 165
- [221] Sugie H, Tanemura M, Filip V, Iwat K, Takahashi K and Okuyama F 2001 *Appl. Phys. Lett.* **78** 2578
- [222] Zhang J, Yang G, Cheng Y, Gao B, Qiu Q, Lee Y Z, Lu J P and Zhou O 2005 *Appl. Phys. Lett.* **86** 184104
- [223] Choi W B *et al* 1999 *Appl. Phys. Lett.* **75** 3129
- [224] Croci M, Arfaoui I, Stöckli T, Chatelain A and Bonard J-M 2004 *Microelectron. J.* **35** 329